Artificial Textile Reinforced Tubular Aortic Heart Valves – Multi-scale Modelling and Experimental Validation

Von der Fakultät für Bauingenieurwesen der
Rheinisch-Westfälischen Technischen Hochschule
Aachen zur Erlangung des akademischen Grades eines Doktors der Ingenieurwissenschaften
genehmigte Dissertation

vorgelegt von
Deepanshu Sodhani

Berichter: Univ.-Prof. Dr.-Ing. habil. Stefanie Reese
Univ.-Prof. Dr. med. Dipl.-Ing., Thomas Schmitz-Rode

Tag der mündlichen Prüfung: 10.12.2018

Dedicated to . . .
my loving wife & parents
"in the vastness of space,
immensity of time,
intricacies of nature &
complexities of life,
it is my joy to spend an epoch with you"
- Carl Sagan

Acknowledgements

First and foremost, I would like to express my gratitude to Prof. Stefanie Reese, Asst. Prof. Scott E. Stapleton and Dr., Privatdozentin Petra Mela for setting up a fruitful collaboration between the Institute of Applied Mechanics and Applied Medical Engineering, paving way for me to work on the presented topic. They have been a constant source of support, encouragement and inspiration. I would further like to thank Prof. Reese for giving me an opportunity to work at the institute on various projects, culminating into this dissertation.

Furthermore, I would like to express my appreciation for all my colleagues at IFAM for maintaining a synergistic, transparent and supportive research atmosphere within the institute. A special thanks to Jaan Simon, Bertram Stier, Johannes Neumann & Daniel Höwer for their friendship, encouragement and intensive discussions on not just the matters of research, but on all walks of life. I would also like to thank my student assistants for their intangible assistance over the course of this work. I would also like to thank materialise NV and FlowVision for their assistance and for providing me with free CT to geometry generation and fluid solvers tools, respectively.

Last but not the least, I express my heartfelt appreciation to my parents and friends for their endless support. Particularly, to my best friend & wife Aparna for umpteen patience and encouragement.

Deepanshu Sodhani

Summary

Valvular heart disease is characterized by damage to or a defect in one of the four heart valves: the mitral, aortic, tricuspid or pulmonary. Patients with a malfunctioning valve often must undergo a valve replacement surgery. Prosthetic heart valves deployed in the left heart (aortic and mitral) are subjected to harsh hemodynamical conditions causing durability concerns in existing prostheses. Therefore, self-healing tissue-engineered valvular prostheses that can replace damaged native valves are in development as an alternative to available prostheses. Most of the tissue engineered heart valves have been developed for the low-pressure pulmonary position because of the difficulties in fabricating a mechanically strong valve which is able to withstand the higher loads of the systemic circulation of left heart. Ergo, engineered soft tissues can greatly benefit from reinforcements to attain mechanical properties comparable with that of the native organs. Complex interactions at various levels between the reinforcements and engineered tissue make the selection of the most optimized reinforcing scaffold difficult and subject to an enormous amount of experimental evaluation. Also, to better design these implants, material behaviour of the composite, valve kinematics and its hemodynamical response need to be evaluated.

Experimental assessment can be immensely time consuming and expensive, paving way for numerical studies. Hence, to reduce the extent of prototyping, it is prudent to develop a simulation-based development approach. In the presented example of valvular prostheses (aortic valve) which are textile-tissue composites, we test a simulation approach based on multi-scale modelling, often used for evaluating/predicting the behaviour of composites. The current study seeks to predict the behaviour of textile reinforced artificial heart valves along with its hemodynamical behaviour. The complex textile structure was divided into simplified models at different scales. Virtual experiments were

conducted on each of these models and their response was fitted by appropriate isotropic and anisotropic hyperelastic material models. The textile response was then used in a macro scale heart valve model, which was subjected to dynamic cardiac loading in a pure mechanical (finite element method - FEM) and multi-physics fluid structure interaction (FSI) simulation. An in-silico immersed boundary (IB) fluid structure interaction (FSI) simulation emulating the in-vitro experiment was set-up to evaluate and compare the geometric orifice area and flow rate for one beat cycle.

Results from the in-silico FEM & FSI simulation were found to be in good coherence with the in-vitro test during the systolic phase, while deviating slightly in the FSI study during the diastolic phase of a beat cycle. Overall the modelling technique provided a good correlation with experimental results, laying the pathway to further study the complex interaction between the engineered tissue and their reinforcing scaffolds. This method can further form the basis for evaluating the mechanical bio-compatibility of scaffolds and their interaction with engineered tissues at various scales and levels.

Zusammenfassung

Ein Therapieverfahren bei degenerativen Herzklappenerkrankungen ist der chirurgische Ersatz der betroffenen Klappe durch eine Prothese. Da bei den bestehenden Prothesen Probleme bezüglich der Haltbarkeit auftreten können, werden als Alternative selbstheilende, gewebegefertigte Herzklappenprothesen entwickelt, die beschädigte native Herzklappen ersetzen können. Zurzeit konzentriert sich die Entwicklung dieser Klappen auf die rechte Herzseite (Pulmonal- und Trikuspidalklappe), da hier geringere hämodynamischen Belastungen herrschen. Der Vorteil dieser Art von Klappengewebe ist, dass durch Gewebeverstärkungen mechanische Eigenschaften erreichbar sind, die mit denen der natürlichen Klappe vergleichbar sind. Allerdings machen komplexe Wechselwirkungen auf verschiedenen Ebenen zwischen den Verstärkungen und dem konstruierten Gewebe die Auswahl des am besten optimierten Bewehrungsgerüsts schwierig. Um diese Implantate besser zu gestalten, müssen auch das Materialverhalten des Verbundes, die Ventilkinematik und die hämodynamische Reaktion bewertet werden. Da die experimentelle Testung sehr aufwändig ist, werden bei der Entwicklung dieser gewebegefertigten Herzklappen Computersimulationen genutzt um den Entwicklungsprozess zu unterstützen.

Inhalt der vorliegenden Arbeit ist die Simulation einer Aortenklappenprothese bestehend aus einem Textil-Gewebe-Verbundwerkstoff mithilfe eines neuen Simulationsansatzes. Dieser basiert auf der Grundlage einer mehrskaligen Modellierung, die häufig zur Bewertung und Vorhersage des Verhaltens von Verbundwerkstoffen verwendet wird. Ziel der Arbeit war es das Verhalten von textilverstärkten künstlichen Herzklappen zusammen mit ihrem hämodynamischen Verhalten vorherzusagen. Die komplexe textile Struktur wurde in vereinfachte Modelle mit verschiedenen Maßstäben unterteilt (Faser, Gewebe, Klappensegel). An jedem dieser Modelle wurden virtuelle Experimente durchgeführt und ihre Reaktion wurde durch geeignete isotrope und anisotrope

phänomenologische Materialmodelle angepasst. Das angepasste numerische Modell wurde dann in einer Herzklappensimulation verwendet, in der eine dynamische Herzbelastung mit einer mechanischen Finite-Elemente-Methode (FEM) und einer multiphysikalischen Fluid-Struktur-Interaktion-Ansatz (FSI) durchgeführt wurde. Die geometrische Öffnungsfläche und die Durchflussmenge wurden mit Hilfe dieses Modells für einen Herzschlagzyklus bestimmt.

Die Ergebnisse der FEM und FSI-Simulation zeigten eine gute Kohärenz mit dem in-vitro-Test während der systolischen Phase, und leichte Abweichungen während der diastolischen Phase für die FSI-Simulationen. Insgesamt zeigt der Modellierungsansatz eine gute Korrelation mit experimentellen Ergebnissen, so dass weitere Untersuchung der komplexen Wechselwirkung zwischen dem konstruierten Gewebe und seinen Verstärkungsgerüsten durchgeführt werden können. Diese Methode kann weiterhin die Grundlage für die Bewertung der mechanischen Biokompatibilität von Gerüsten und deren Interaktion mit technisiertem Gewebe auf verschiedenen Modellierungsebenen bilden.

Contents

1 Introduction

1.1 Motivation and research-relevant questions

Valvular heart disease remains common in industrialized countries, because the decrease in prevalence of rheumatic heart diseases has been accompanied by an increase in that of degenerative valve diseases. Valvular heart disease is characterized by damage to or a defect in one of the four heart valves: the mitral, aortic, tricuspid or pulmonary. The prevalence of valvular disease increases sharply with age, owing to the predominance of degenerative etiologies. Aortic stenosis and mitral regurgitation are the two most common types of valvular disease in Europe.

Normally, functioning valves ensure that blood flows with proper force in the proper direction at the proper time as shown in Fig. 1.2a. The mitral and tricuspid valves control the flow of blood between the atria and the ventricles (the upper and lower chambers of the heart). The pulmonary valve controls the flow of blood from the heart to the lungs, and the aortic valve governs blood flow between the heart and the aorta, and thereby the blood vessels to the rest of the body. The mitral and aortic valves are the ones most frequently affected by valvular heart disease. A stenotic valve forces blood to back up in the adjacent heart chamber, while an incompetent valve allows blood to leak back into the chamber it previously exited (Fig. 1.2b). To compensate for poor pumping action, the heart muscle enlarges and thickens, thereby losing elasticity and efficiency. In addition, in some cases, blood pooling in the chambers of the

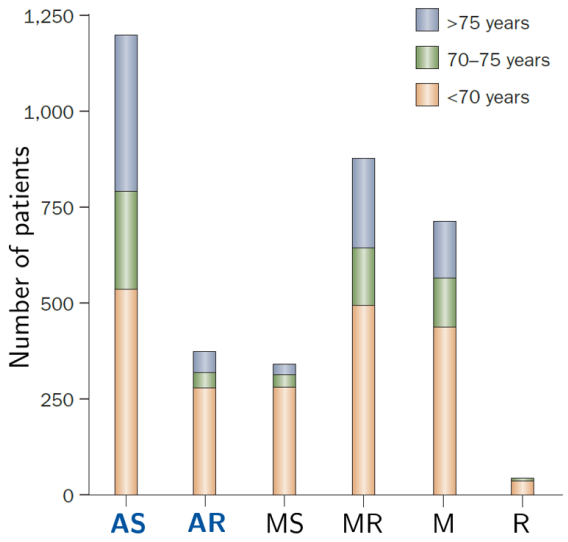

Figure 1.1: Distribution of the various types of native valvular heart disease in 3,547 patients in the Euro Heart Survey. Abbreviation: AR, aortic regurgitation; AS, aortic stenosis; M, multiple valve disease; MR, mitral regurgitation; MS, mitral stenosis; R, right-sided heart disease. Reproduced from Iung and Vahanian [2011]

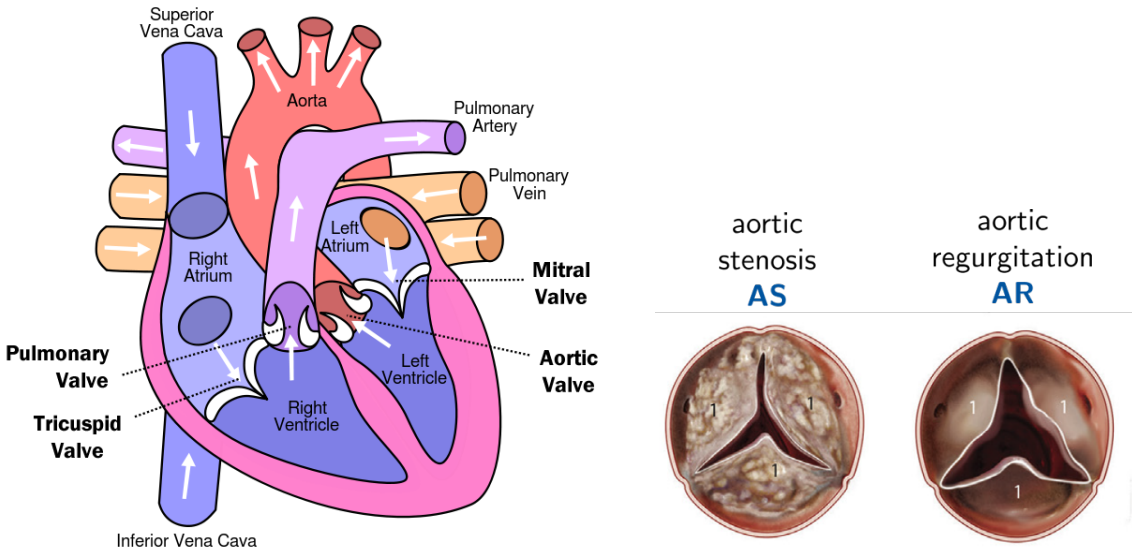

(a) (b)

Figure 1.2: (a) schematic representation of human heart and the its valves, showing the direction of blood flow; (c) aortic stenosis and regurgitation

heart has a greater tendency to clot, increasing the risk of stroke or pulmonary embolism. The severity of valvular heart disease varies. In mild cases there

may be no symptoms, while in advanced cases, valvular heart disease may lead to congestive heart failure and other complications. Treatment depends upon the extent of the disease.

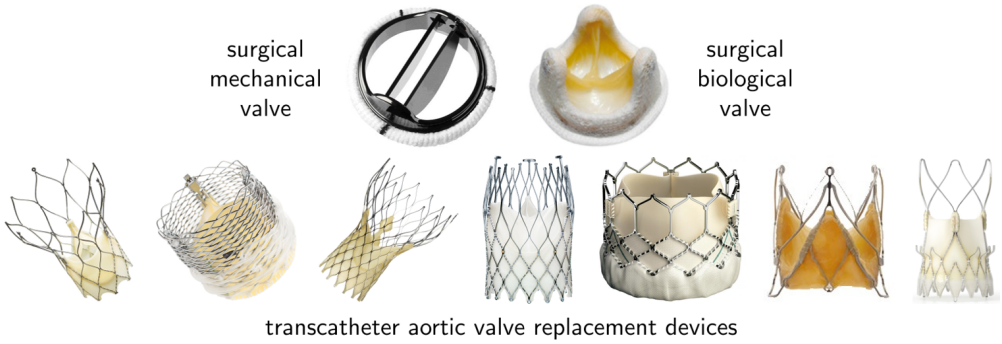

Figure 1.3: Different types of approved and in-development aortic valves (St.Jude Medical|Boston Scientific|Medtronic|NVT|Edwards|Jena Valve)

There are two primary surgical approaches, open heart surgical valve replacement for low risk patients where often a mechanical or biological valve is used, and a percutaneous transcatheter valve replacement procedure for high risk patients which delivers a decellularized tissue valve construct to the site of the diseased valve through a catheter (Fig. 1.3). Mechanical valves require a life-long anticoagulation therapy because of the associated risk of thrombosis and thromboembolism, while the biological/decellularized valves which are not as stiff as the native valve, suffer from structural degeneration and therefore have a limited life Padala et al. [2011]; Pibarot and Dumesnil [2009]. Tissue engineered heart valves have been proposed as alternatives to the clinically adopted heart valves to overcome their limitations. Different tissue engineering strategies have been proposed for the realization of valves which ultimately will consist of healthy tissues produced by the patient's own cells, putatively eliminating the above-mentioned limitations [Cheung et al. [2015]; Namiri et al. [2017]]. The goal is to provide the patient with an implant produced with and by the patient's own cells, able to remodel and self-repair, with physiological hemocompatibility, biologically and mechanically equivalent to the native

tissue.

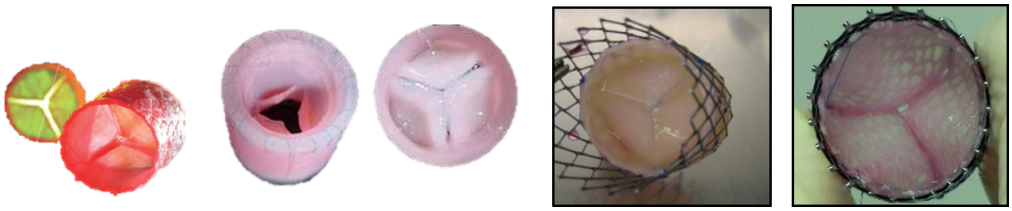

Figure 1.4: Tissue-engineered surgical and percutaneously implantable valve (DBE, TU/e | AME, RWTH)

One such example of tissue-engineered heart valves for surgical or transcatheter implantation is the research being conducted at the institute of Applied Medical Engineering, RWTH Aachen University [Weber et al. [2013]; Moreira et al. [2016]]. In most cases, pure engineered tissues do not possess the mechanical properties required by valvular implants to sustain the working pressures of the systemic circulation. This can be overcome with the use of a three-dimensional textile scaffolds as reinforcement on which cells can grow, proliferate and form into a functional tissue construct. Tissue engineered valves were reinforced with textile for both surgical implantation [Weber et al. [2013]; Moreira et al. [2016]] as well as percutaneous delivery [Moreira et al. [2014a]].

An optimum scaffold architecture for tissue-engineered heart valves is a structure with a high degree of interconnectivity (through continuous or interconnected short fibres) allowing for uninterrupted stress flow through the thin heart valve leaflets to the strong aortic wall, protecting the cusps from rupture yet being porous enough to allow cellular in-growth. A mismatch between highly deformable native tissue and engineered biomaterials can lead to short and long-term health impairments. The capability of implants to functionally deform with respect to the surrounding biological materials, is often associated with non-affine micro structural deformation mechanism. This non-affinity on smaller length scales might lead to micro injuries, cell damage, inflammation, fibrosis or necrosis (Mazza and Ehret [2015]). Hence, the mechanical biocom-

patibility of soft implants depends not only on the properties and composition of the implant material, but also on its organization, distribution and motion at one or several length scales.

In the current work, a textile mesh (knitted scaffolds) was used in the development of tissue-engineered tubular aortic heart valves [Weber et al. [2013]; Moreira et al. [2014a]]. The textile reinforcement must be carefully designed: too much reinforcement can cause the valve to be too stiff and lose functionality, while too little reinforcement can lead to early failure of the leaflets. To facilitate intentional, intelligent and mechanically biocompatible valve design, computational models of heart valves are required that form a link between reinforcement design and valve performance. The ability of a model to predict valve performance relies on the representation of three main aspects: topological delineation of the complex reinforcement, its material properties and the loading/boundary conditions on the valve.

1.2 State-of-the-art

A substantial amount of work has been done in the field of cardio-vascular engineering, from experiments to simulation. Cheung et al. [2015] reviewed the current progress in tissue engineering of heart valves, looking at different fabricating strategies of tissue engineered heart valves (TEHVs), concluding that a clinically viable product has not yet been realized. Singh et al. [2015] reviewed the design aspect of medical textiles (woven, knitted, braided, electrospun) intended for vascular implant applications, concluding that mechanical properties of biological material such as anisotropy, non-linearity, compliance and visco-elasticity remain widely unconsidered while designing synthetic vascular implants. Mazza and Ehret [2015] showed that the mechanical biocompatibility of scaffolds is not only linked to adequate macroscopic properties (non-linear stress-strain response, ductility, strength) but also to the realization

of micro structural deformation mechanisms, in particular, the deformation field at the cell length scale influences the mechano-transduction and mechano-biological response of the tissue surrounding the implant.

Some of the works in the direction of stress and strain analysis of heart valves under its diastolic and systolic phase are detailed in this paragraph. Stapleton et al. [2015] analysed the effect of fibre orientation and volume fraction on the macroscopic stress developed in a tubular three leaflet heart valve in its closed configuration, indicating that a non-uniform fibre distribution using tailored fibre placement could be used to optimize reinforcement design. Argento et al. [2012] presented an approach of mechanical characterization of the electro-spun scaffolds for TEHVs, by accounting for the effect of underlying scaffold structure. The derived material properties were then used to simulate the stress and strain in a heart valve when it was closed. De Hart et al. [2004] analysed the effects of collagen fibres (distributed short natural fibres) on the mechanics and hemodynamics of a trileaflet aortic valve using a numerical analysis of the systolic phase. It demonstrates that presence of distributed fibres substantially reduces stresses in the leaflets and provide smoother opening and closing while reducing the fluttering motion of the leaflets. Cacciola et al. [2000a,b] produced stent less artificial aortic valve prosthesis and analysed different fibre-reinforced structures with respect to the stresses that are likely to contribute to the failure of fibre-reinforced prostheses and compared them with the results obtained for a stented prosthesis. The comparison showed that stress developed in the stent less models were significantly lower than the stented models with the same type of reinforcement. De Hart et al. [1998] analysed three-dimensional finite element models for reinforced three-leaflet valve prosthesis for stress reduction. Different fibre reinforcements were investigated, and the model responses were analysed for stresses showing that, in peak stress areas of reinforced models, up to 60% of the maximum principle stresses were taken over by fibres and

that, in some cases of reinforcement, a more homogeneous stress distribution was obtained. Jana et al. [2014] compared the advantages and disadvantages of decellularized and fabricated scaffolds for use as TEHVs, concluding that synthetic scaffold-based TEHVs are more suited as an implant because they can be tailored to the requirement. Even though decellularized scaffolds retain the original valve structure and extra-cellular matrix, their low pore size, porosity and cell survivability limit their use for valve engineering. Van Lieshout et al. [2006a] tested various bio-compatible scaffold heart valves and fibrin under systemic circulation and compared the electro-spun valvular scaffold with knitted valvular scaffold in Van Lieshout et al. [2006b]. It was shown that the knitted textile scaffold lasted longer in the systemic circulation as the electro-spun scaffold tore after a while. Yeoman et al. [2010] developed a constitutive model to represent the non-linear warp-weft coupled mechanics by extending a strain energy function for soft tissue to include shear and by increasing the number and order of coefficients, which was validated for uniaxial tension tests. The model was successfully able to predict the macro behaviour of some textiles but fails to capture the micro mechanics and its effects. D'Amore et al. [2014] simulated the mesoscopic in-plane mechanical behaviour of elastomeric electro-spun polyurethane membrane where the simulations were developed from experimentally-derived fibre network geometries. Effects on macro-mechanics based on fibre intersections, connectivity, orientation, and diameter were evaluated demonstrating good agreement with the experimental data.

A significant amount of work has also been invested in modelling the macroscopic behaviour of biological materials (which have differently oriented short fibres as reinforcement). Much of the works on continuum modelling of isotropic and anisotropic material behaviour has been reviewed in Chagnon et al. [2015]. These materials are known to support large reversible deformations along with exhibiting hysteresis, stress softening or relaxation. A hyper-

elastic constitutive equation is typically the basis of the model that describes the behaviour of the material. The hyperelastic constitutive equation can be isotropic or anisotropic. Böl et al. [2009] used a micro mechanically motivated tetrahedral element developed in Böl and Reese [2006] to create a predictive model of thin muscular films accounting for the muscle fibres. Auricchio et al. [2014] tested the impact of using different material models in a patient-specific finite element analysis able to virtually reproduce stent-less valve implantation, on both the stress pattern and post-operative coaptation area, length and height. Also, physical and non-physical response from a few of these hyperelastic material models have been compared in Duong et al. [2015]. While several studies consider the valve to be a homogeneous elastic material [Koch et al. [2010]; Hsu et al. [2014]; Kamensky [2015]], others model the valve accounting for the collagen fibres in the native tissue valve using phenomenological material models. Such approaches do not facilitate design of the reinforcements. This further necessitates, a multi-scale modelling approach for an artificial textile reinforced tubular aortic heart valve.

In the field of traditional fibre reinforced composites, there has been tremendous development in multi-scale material modelling; investigating the effects of the micro structure on its macroscopic behaviour. Nguyen et al. [2011] reviewed the recent developments in multi-scale modelling of continuous and discontinuous modelling of multi-phase heterogeneous materials. Vassiliadis et al. [2011] discussed the challenges and solutions/modelling methodologies for woven fabrics at different scales accounting for micro to macro scale deformations. An extended literature review of the computational models for the deformation of woven fabrics was presented. A review on homogenization and topology optimization of periodic structure was presented by Hassani and Hinton [1998]. Some of the recent works in the direction of multi-scale modelling of composites accounting for the micro structural effects are presented

in Döbrich et al. [2016]; Li et al. [2016]; Bednarcyk et al. [2015] and Stier et al. [2015a,b]. There are also studies that deal with multi-scale modelling of heart valves, where the problem at hand is tackled at organ, tissue, cell and molecular scales Weinberg and Mofrad [2007]; Weinberg et al. [2010]. In these approaches, the material characteristics of the higher scale is obtained from the lower scale, whereas the response of the underlying structure is often not accounted for clearly. Argento et al. [2012] present an approach of mechanical characterization of the scaffolds for tissue engineered heart valves, by accounting for the effect of underlying scaffold structure, which is like the approach presented in this study.

Finally, the loading of the blood flow on the leaflets needs to be represented. Several studies have been carried out to evaluate the influence of topological design and material response by simply considering the hydrostatic pressures acting on the structural domain [Koch et al. [2010]; Li and Sun [2010]; Sun et al. [2010]; Loerakker et al. [2013]; Saleeb et al. [2013]; Gunning et al. [2014]; Morganti et al. [2014, 2015]; Wang et al. [2015]; Sodhani et al. [2016]]. While these methods give a general idea of the performance of the valve, decoupled FE simulations often neglect the interaction of the fluid with the valve surface and its resulting loads. Hence, FSI models are becoming increasingly important for biomedical engineering applications Luraghi et al. [2017]. A general review of FSI methods was presented in Hou et al. [2012], while reviews on FEA, CFD and FSI simulation approaches for cardiac valves are found in Votta et al. [2013]. Experimental validation of FSI simulations have been reported in Wu et al. [2016]; Joda et al. [2016]. The number of studies considering FSI to evaluate the valve kinematics are increasing [see e.g. Borazjani and Sotiropoulos [2010]; Marom et al. [2012]; Griffith [2012]; Sturla et al. [2013]; Borazjani [2013]; Bavo et al. [2016]; Wu et al. [2016]; Joda et al. [2016]; Mao et al. [2016]; Luraghi et al. [2017]].

1.3 Present work

Currently, the reinforcing scaffold is intuitively chosen without any prior mechanical biocompatibility evaluation in terms of meso- and micro-mechanisms for deformation. This is because it is complicated to formulate a quantitative criterion as not only are the values often missing, but the quantities to evaluated are not clearly defined. Therefore, in this work, we attempt to apply and validate the popular multi-scale modelling approach to evaluate the mechanical behaviour of the knitted textile scaffold used in the development of the tissue engineered heart valves by Weber et al. [2013]; Moreira et al. [2014a]. For the assessment of the approach a simplified textile reinforced valve was used, where silicone was used in place of the complex anisotropic tissue model (*si*licone embedded *tex*tile reinforced heart *valve* (siTexValve)). The following work is divided into three parts.

In the first part (Article 1), behaviour of a textile scaffold reinforced strip was predicted using the multi-scale modelling approach. Two competing methodologies were tested. In one, the underlying geometric structure was reconstructed from CT data and in the second, idealized underlying geometric structure was used. The latter more accurately predicted the macroscopic response of the test sample.

In the second part (Article 2), the validated multi-scale modelling approach was employed to predict the kinematics of the simplified valve. The valve was divided into four representative levels, where individual levels were subjected to virtual experiments and their response was fitted with an appropriate phenomenological model. Finally, the valve was simulated for its kinematics using hydrostatic pressures as loads. The predicted valve kinematics were in good agreement with the experimental data.

Finally, a multi-physics fluid structure interaction simulation method was setup to evaluate the hemodynamic behaviour of the valve. The predicted valve

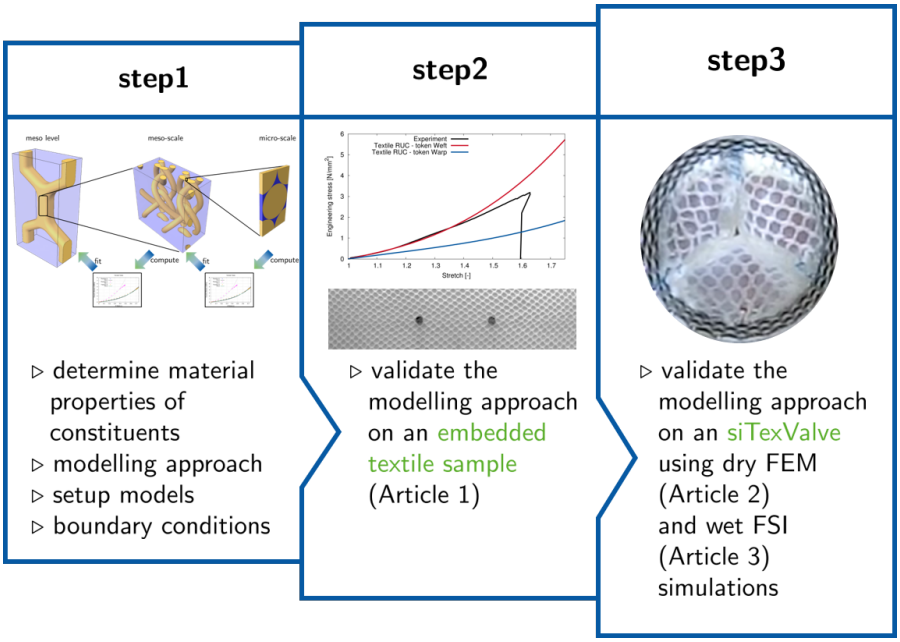

Figure 1.5: Steps involved in the presented work

kinematics and the systolic flow rates were in good agreement with experimental results, while some deviation was observed during the diastolic phase. Differences between the dry FEM and wet FSI simulations were compared and medically relevant risk parameters were evaluated.

The thesis concludes with a conclusion and a brief overview of the future work, where the developed multi-scale method can be employed to study the tissue growth.

2 Article 1: Multi-scale modelling and simulation of a highly deformable embedded biomedical textile mesh composite

This article was published as:

Sodhani D, Reese S, Jockenhövel S, Mela P, Stapleton SE. Multi-scale modelling and simulation of a highly deformable embedded biomedical textile mesh composite. Composites Part B: Engineering. 2018 Jun 15;143:113-31.

Disclosure of the individual authors' contributions to the article:

D. Sodhani conceptualized the multi-scale modelling technique, conducted the experiments, generated the required geometries and carried out the simulations; P. Mela provided the experimental samples along with intellectual content and gave conceptual advice; S.E. Stapleton provided the python script for fitting anisotropic material models along with intellectual content and gave conceptual advice; S. Reese & S. Jockenhövel provided intellectual content and gave conceptual advice; S. Reese, P. Mela and S.E. Stapleton were engaged in obtaining funds for the research; All authors drafted the work for intellectual content; All authors approved the publication of the final manuscript.

2.1 Abstract

Self-healing prostheses that can replace damaged native organs, like tissue-engineered valvular implants, are under development. Engineered soft tissues can greatly benefit from reinforcements to attain mechanical properties comparable with the native organs. Complex interactions at various levels between the reinforcements and engineered tissue make the selection of the most optimized reinforcing scaffold difficult and subject to an enormous amount of experimental evaluation. Hence, to reduce the extent of prototyping, it is prudent to develop a simulation based development approach. In the example of valvular prostheses which are textile-tissue composites, we test a simulation approach based on multi-scale modelling, often used for evaluating/predicting the behaviour of composites. A textile scaffold embedded in silicone is used as a replacement for the textile-tissue composite. The modelling technique provides a good correlation with the experimental results, laying the pathway to further study the complex interaction between the engineered tissue and the reinforcing scaffold. This method can further form the basis for evaluating the mechanical compatibility of scaffolds and their interaction with engineered tissues at various scales and levels.

2.2 Introduction

Engineered biomaterials are ubiquitous and have important function in numerous biomedical applications. One such application of biomaterial implants is tissue-engineered heart valves for surgical or transcatheter implantation Weber et al. [2013]; Moreira et al. [2016], where replacement of self-healing, load-bearing soft tissues is an impetus for their development. In most cases, pure engineered tissues do not possess the mechanical properties required by such implants to sustain the working pressures of the systemic circulation. This can

be overcome with the use of reinforcing scaffolds. An optimum scaffold architecture for tissue-engineered heart valves is a structure with a high degree of interconnectivity (through continuous or interconnected short fibres) allowing for uninterrupted stress flow through the thin heart valve leaflets to the strong aortic wall, protecting the cusps from rupture yet being porous enough to allow cellular in-growth. In the current work, a textile mesh (knitted scaffolds) used in the development of tissue-engineered tubular aortic heart valves Weber et al. [2013]; Moreira et al. [2014a] has been used as an example.

Currently, the reinforcing scaffold is intuitively chosen without any prior mechanical compatibility evaluation in terms of meso- and micro-mechanisms of deformation. This is because it is complicated to formulate a quantitative criterion as not only are the values often missing, but even the quantities to be evaluated are not clearly defined. Therefore, characterization should be performed at the macro- and microscopic length scales (multi-scale properties) because a mismatch between highly deformable engineered tissue and scaffolds can lead to short and long-term health impairments. Hence, the mechanical compatibility of reinforcing scaffolds depends not only on the properties and composition of the material, but also on its organization, distribution and motion at one or several length scales. Various biocompatible scaffold heart valves were tested by Van Lieshout et al. [2006a,b] under systemic circulation, concluding that the knitted scaffolds lasted longer compared to their electrospun counterpart.

In their review, Mazza and Ehret [2015] elaborated that mechanical compatibility of highly deformable reinforcing scaffolds depends more on their deformation behaviour rather than on their strength. In fact, integration of engineered tissues with textile mesh are not only associated with adequate macroscopic properties (non-linear stress strain response, ductility, strength) but also with their realization by micro-structural kinematics which should

match those of the adjacent tissue. Mechanical interaction is determined by the spatial arrangement i.e., the topology of the micro-structure, governing the local and global deformation behaviour. Length scales responsible for the mechanical response depend on the material system and are in the range of mm for such prosthetic meshes. Multiple measurements for different loading states are required to reliably characterize the deformation behaviour of such scaffolds. Therefore, to achieve design and mechanical compatibility, modelling strategies to rationalize experimental observations and predict implant performance need to be developed.

There are three major modelling approaches of textile fabrics, namely continuum, structural and multi-scale methods. Significant amount of work in representing the continuum macroscopic behaviour of differently oriented fibre reinforced material has been developed in the last few decades. Much of the works on continuum modelling of isotropic and anisotropic material behaviour has been reviewed in Chagnon et al. [2015]. The continuum macro-scale approach like the ones proposed in Hernández-Gascón et al. [2011] and Yeoman et al. [2010] can be easily implemented into FEM code to efficiently simulate inhomogeneous load cases which is not straight forward in other meso- or micro-scale methods. However, fabrics are not a continuum and a large experimental data set is needed to fit the corresponding model parameters.

The central idea behind the structural models is to use a physically motivated meso-scale structure to capture the relevant mechanical phenomena at the macro-scale. In this way suitable criteria for fabric design and optimization can be deduced.

Weaves are the simplest structure among fabrics and are the most examined in the literature, see King et al. [2005]; Nadler et al. [2006]; Assidi et al. [2011]; Ben Boubaker et al. [2007]; Grujicic et al. [2009]; Nayfeh and Kress [1997]; Mingxing Xiao et al. [2011]. These structural models focus primarily on yarn-

yarn interaction such as shear-locking or crimp interchange in tension. Macro-scale phenomena simulated by such models include geometric non-linearity, non-linear force-strain relationships, large Poisson's ratios or anisotropy. There are only a few structural models for knitted textiles, e.g. Antonietti et al. [2011] and Röhrnbauer et al. [2014]. A repeating unit cell (RUC) of knitted prosthetic mesh based on the theory of multi-body systems showing good correlation with effective macro-scale experimental results and local non-affine deformation state was proposed by Röhrnbauer et al. [2014]. However, as these models generally use truss or rigid force elements and the presence of matrix is usually either implemented as boundary conditions or enforced in model equations, it is not possible to extract the local stress and strain fields in the matrix. These values are important to determine the growth and remodelling of tissues. Also, since the method is physically motivated, large number of parameters are needed to account for stitches, nodes or cross-links.

An equally popular method is the use of detailed micro-scale approach, see Duhovic and Bhattacharyya [2006]; Hart et al. [1985]; De Jong and Postle [1978]. Due to their complex inter-looping patterns, knitted dry fabrics are more frequently modelled at the micro-scale with an explicit representation of each filament/yarn Duhovic and Bhattacharyya [2006]; Hart et al. [1985]; De Jong and Postle [1978]. A review of such modelling approaches can be found in Hasani et al. [2017]; Huang and Ramakrishna [2000]; Tan et al. [1997] and Hallal et al. [2013]. The geometries and assigned material properties for the filaments/yarns are based on real measured data. Therefore, such detailed models are associated with lesser model assumptions. Virtual experiments with perfectly controlled boundary conditions can be performed on such models. Three-dimensional micro-structural effects, which cannot be evaluated with other models and are generally difficult to be seen from experiments, can be examined through finite element analysis. However, such models are often

computationally expensive and require the solution of multi-contact problems, which often lack numerical convergence or require non-physical assumptions on the friction behaviour and the inter-penetration of filaments Duhovic and Bhattacharyya [2006]. Another challenge is the definition of a representative initial configuration, which might be found by an elaborate simulation of the manufacturing process and the corresponding solution of the unloaded equilibrium state, see Glaessgen et al. [1996]; De Jong and Postle [1978].

Multi-scale modelling of knitted fabrics with basic looping structures are presented in Wan et al. [2016]. Multi-scale approaches are also aimed at determining parameters for corresponding constitutive model formulations to be implemented in finite element codes. There has been tremendous development in the field of multi-scale material modelling of traditional fibre reinforced composites, investigating the effects of micro structure on its macroscopic behaviour. Nguyen et al. [2011] reviewed the recent developments in multi-scale modelling of continuous and discontinuous multi-phase heterogeneous materials. Vassiliadis et al. [2011] discussed the challenges and solutions for modelling methodologies of woven fabrics at different scales accounting for micro to macro-scale deformations. An extended literature review of the computational models for the deformation of woven fabrics was presented. A review on homogenization and topology optimization of periodic structure was presented by Hassani and Hinton [1998] and Saeb et al. [2016].

Geometric modelling approaches for different fabrics and its composites have been presented in literature Adanur and Liao [1998]; Kyosev et al. [2005]; Verpoest and Lomov [2005]; Sherburn [2007]; Lin et al. [2012]; Li et al. [2014]. A representative volume element (RVE) based approach to determine the effective stiffness of a multi-layered biaxial weft-knitted fabric reinforced composite was presented in Qi et al. [2015]. Ugbolue [2015] examined the geometrical model of auxetic warp knit structures and validated their characteristics with

data obtained from experimental analysis.

Even though there is a considerable body of work in various disciplines like modelling of biomaterials, analysis of dry scaffolds and multi-scale modelling of fibre reinforced composites, there is a scarcity in the synergistic approach in determining the mechanical compatibility of scaffolds used in implants. The present work is devoted to a multi-scale method for modelling, simulation and analysis of textile composites used in the development of a tissue-engineered tubular aortic heart valve. In-silico experiments are conducted at various structural levels to predict the macro-scale mechanical behaviour of the textile composite and quantify the local deformation kinematics. A hierarchical multi-scale modelling approach popular in the field of material mechanics is employed. The benefit of this approach is that individual constituents of the composite can be modelled by means of a simple material model, and characterized using standard experiments.

2.3 Experiments

In the present work, a textile-silicone composite was used for validation of the proposed numerical methods. This is because, once the textile is embedded in a tissue matrix, it's mechanical behaviour changes as the deformation mechanics are modified by the ingrowth of tissues. And, in Röhrnbauer and Mazza [2013] and Röhrnbauer et al. [2014], it was shown that when a textile scaffold is embedded into elastomer matrix, its results have the same qualitative conclusion when compared to the corresponding experiment on ex-plants (i.e. dry textile mesh surrounded/embedded into tissue). Also, in contrast to textile-tissue, textile-elastomer composites are easy to handle and inexpensive with test results showing moderate scatter, establishing themselves as an effective tool for mechanical characterization/optimization and validation of numerical methods & models for prosthetic meshes preceding in-animal study. Another advantage

Table 2.1: Dimensions of the specimens

Dimensions	Textile-silicone composite	Silicone samples
length (l)	120.00 mm	120.00 mm
measuring length (l_m)	$\approx$ 29 mm	$\approx$ 31.28 mm
width (w)	25.67$\pm$0.28 mm	6.35 mm
breadth (b)	1.245$\pm$0.05 mm	1.15 mm

of using a textile-elastomer composite as a model for tissue in-growth is the quantification of non-affine deformation mechanisms and local delaminations Maurer et al. [2014].

Textile-silicone composite The textile mesh was produced using medical grade polyethylene terephthalate (PET) fibres. For the production, a tüll-fillet pattern, a needle gauge of E30 (i.e. 30 needles per inch) and a course density of 15 loops/cm were chosen. 52 PET yarns were processed into a tubular structure which was thermo-stabilized at 200°C for 8 minutes before use. The textile mesh was then embedded into a medical grade silicone matrix and cured for two hours. A specimen is shown as an insert in Fig. 2.1 and dimensions of the produced specimens are provided in Table 2.1.

The tensile test set-up, which included a Zwick Z005 testing machine along with a specimen is shown in Fig. 2.1a. The specimens were preloaded with 1 N, and stretched at 3 mm/min until failure at a global strain of about 60%. Time, force, cross head displacement and nominal strains were measured. The kinematic quantities were captured for the specimen in real time, providing global strain values. Nominal strains were measured using an optical extensometer and two points. The mean value and the deviation of engineering stress obtained by testing five samples are plotted against the stretch in Fig. 2.1b. The results from these experiments were used to validate the corresponding simulation outcome.

The amount of fibre in a fibre reinforced composite directly corresponds to

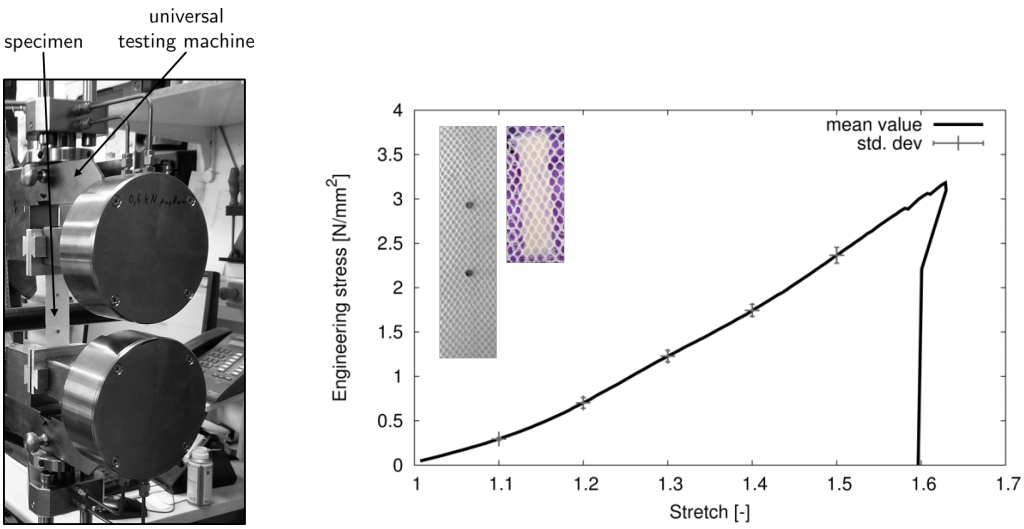

(a) (b)

Figure 2.1: (a) Experimental set-up; (b) mean value and standard deviation for engineering stress vs. stretch values for experiments conducted on five samples of textile-silicone composite (inserts: textile-silicone vs. textile-tissue composite sample)

the mechanical properties of the composite. Adding too little or too much fibre reinforcement in the composite will deviate the properties of the material from its required properties. Therefore, for a given set of constitutes there is an optimal range of fibre volume fraction to achieve the desired end results. The volume fractions of the PET fibres in the samples were derived by considering the density of the PET fibres and its mass over a given area. The density of the PET fibres is 1.38 g/cm^3. The mass m of the textile mesh over an area of $A =$ 551.25 mm^2 (l =17.5 mm, b =31.5 mm) was found to be 0.025 g. Hence, using $\phi = V_{textile}/V_{total} = (m/A)/(t\rho)$ the volume fraction of the composite for the same area A was determined to be $\approx$ 2.564%.

2.4 Materials and Methods

In this section, we start with a brief description of the material models used, followed by an illustration of multi-scale modelling, computational homogenization and boundary conditions. Geometries used at various scales/levels is

described thereafter.

2.4.1 Material models

The two material constituents, PET fibres and silicone matrix, are modelled with isotropic linear elasticity and hyperelasticity. The bundle of fibres (yarns) together were assumed to behave transversely linearly isotropic. Fung's orthotropic hyperelasticity law (see Fung et al. [1979]) was used to represent the large deformation anisotropic response of the textile structure embedded in the matrix. Various other orthotropic/anisotropic hyperelastic material models such as those developed by Holzapfel and Gasser [2001]; Reese [2003]; Holzapfel [2004]; Gasser et al. [2006] and Ehret and Itskov [2007] could also be used to represent orthotropic/anisotropic large deformation material response. But, since the focus of this paper was more on the methodology rather than material modelling, implementing any one of these models was outside the scope of this work.

Transversely isotropic material model Yarns are modelled using a transversely isotropic material law. Transverse isotropy is a special case of orthotropy, where a material is isotropic with respect to one plane and has different properties in the direction normal to this plane. Such materials can be described by a minimum of five independent elastic constants for the linear case, but might require more parameters to account for non-linear situations. By convention, the five elastic constants in transversely isotropic constitutive equations are the Young's modulus and Poisson's ratio in the symmetry plane, E_p and ν_p, the Young's modulus and Poisson's ratio in the normal direction, E_n and ν_{np}, and the shear modulus μ_{np}. Considering the out of plane direction to be the

z-direction, the compliance matrix in Voigt notation can be written as follows:

$$\begin{bmatrix} \epsilon_{\mathrm{xx}} \\ \epsilon_{\mathrm{yy}} \\ \epsilon_{\mathrm{zz}} \\ 2\epsilon_{\mathrm{yz}} \\ 2\epsilon_{\mathrm{zx}} \\ 2\epsilon_{\mathrm{xy}} \end{bmatrix} = \begin{bmatrix} \frac{1}{E_{\mathrm{p}}} & -\frac{\nu_{\mathrm{p}}}{E_{\mathrm{p}}} & -\frac{\nu_{\mathrm{np}}}{E_{\mathrm{n}}} & 0 & 0 & 0 \\ -\frac{\nu_{\mathrm{p}}}{E_{\mathrm{p}}} & \frac{1}{E_{\mathrm{p}}} & -\frac{\nu_{\mathrm{np}}}{E_{\mathrm{n}}} & 0 & 0 & 0 \\ -\frac{\nu_{\mathrm{pn}}}{E_{\mathrm{p}}} & -\frac{\nu_{\mathrm{pn}}}{E_{\mathrm{p}}} & \frac{1}{E_{\mathrm{n}}} & 0 & 0 & 0 \\ 0 & 0 & 0 & \frac{1}{\mu_{\mathrm{np}}} & 0 & 0 \\ 0 & 0 & 0 & 0 & \frac{1}{\mu_{\mathrm{np}}} & 0 \\ 0 & 0 & 0 & 0 & 0 & \frac{2(1+\nu_p)}{E_{\mathrm{p}}} \end{bmatrix} \begin{bmatrix} \sigma_{\mathrm{xx}} \\ \sigma_{\mathrm{yy}} \\ \sigma_{\mathrm{zz}} \\ \sigma_{\mathrm{yz}} \\ \sigma_{\mathrm{zx}} \\ \sigma_{\mathrm{xy}} \end{bmatrix} \tag{2.1}$$

Hyperelastic material models Hyperelastic materials are known to support large reversible deformations along with exhibiting hysteresis, stress softening or relaxation. A hyperelastic constitutive equation is typically the basis of the model that describes the behaviour of these materials. The hyperelastic constitutive equation can be isotropic or anisotropic. Also, physical and non-physical responses from a few of these hyperelastic material models have been compared in Duong et al. [2015].

Arruda Boyce material model Arruda and Boyce [1993] model is an isotropic hyperelastic constitutive model used to describe the mechanical behaviour of rubber-like and other polymeric substances, is used to model the silicone matrix. This model is based on the statistical mechanics polymeric chains within an elastomer with a cubic representative volume element containing eight chains along the diagonal directions. The material is assumed to be incompressible and the strain energy density function is given by

$$W = Nk_B\theta\sqrt{n}\left[\beta\lambda_{\mathrm{chain}} - \sqrt{n}\ln\left(\frac{\sinh\beta}{\beta}\right)\right] \tag{2.2}$$

where n is the number of chain segments, k_B is the Boltzmann's constant, θ is the temperature given in Kelvin and N is the number of chains (density of

chains) in the network of cross-linked polymers.

$$\lambda_{\text{chain}} = \sqrt{\frac{I_1}{3}} \; ; \;\; \beta = \mathcal{L}^{-1}\left(\frac{\lambda_{\text{chain}}}{\sqrt{n}}\right) \;\; ; \;\; \mu_{ab} = N k_B \theta \tag{2.3}$$

where λ_{chain} represents the stretch of a chain, I_1 is the first invariant of the right Cauchy-Green deformation tensor, and $\mathcal{L}^{-1}$ is the inverse Langevin function. μ_{ab} is the shear modulus obtained by fitting the experimental results.

Fung's orthotropic material model The generalized Fung strain energy potential in Abaqus is based on the two-dimensional exponential form proposed by Fung et al. [1979], which was suitably generalized to arbitrary three-dimensional states using Humphrey [1994]. It has the form

$$W = \frac{c}{2}(e^Q - 1) + \frac{K}{2}\left(\frac{(J^2) - 1}{2} - \ln J\right) \tag{2.4}$$

where c is the shear modulus, K is the bulk modulus, J is the change in volume and Q is defined by

$$Q = \mathbf{E} : \mathbb{B} : \mathbf{E} \tag{2.5}$$

$\mathbb{B}$ is a dimensionless symmetric fourth-order tensor of anisotropic material constants, $\mathbf{E}$ represents the Green-Lagrange strain tensor and : is the scalar multiplication operator. The orthotropic form of the generalized Fung model with eleven independent variables is used in this work. The Voigt notation of

the $\mathbb{B}$ matrix is given by

$$\hat{\mathbf{B}} = \begin{bmatrix} b_1 & b_7 & b_8 & 0 & 0 & 0 \\ b_7 & b_2 & b_9 & 0 & 0 & 0 \\ b_8 & b_9 & b_3 & 0 & 0 & 0 \\ 0 & 0 & 0 & b_4 & 0 & 0 \\ 0 & 0 & 0 & 0 & b_5 & 0 \\ 0 & 0 & 0 & 0 & 0 & b_6 \end{bmatrix} \tag{2.6}$$

It is well known in the literature that parameter fitting of the Fung model largely depends on the choice of initial values. Hence, care has been taken to choose the initial values reasonably while fitting this model to the virtual experiments at different levels.

2.4.2 Multi-scale modelling, homogenization and boundary conditions

Mechanical tests are often designed to create a macroscopically homogeneous field of strain over a certain measurement region of the specimen. For composite materials, however, this seemingly homogeneous strain is an average of the strains on smaller length scales that are experienced by its constituents and are difficult to measure experimentally. Fibres or yarns (bundle of fibres) may be subjected to small or large strains depending on their material properties or orientations. Heterogeneity of the deformations on smaller length scales which might increase with a decreasing scale of observation, define the macroscopic behaviour of the composite. This is where multi-scale modelling and computational homogenization can be used to characterize the smaller length scales, understand the deformation behaviour and optimize the scaffold structure.

A methodology referred to as "hierarchical multi-scaling" in the literature (see Bednarcyk et al. [2015]) was used in the current work. This means that an incremental deformation gradient was applied on a structural unit cell model as

kinematic boundary conditions. The model was solved according to minimum energy principles and the stresses homogenized over the volume (or reaction forces obtained averaged over the respective boundaries) led to the incremental stress tensor, producing a virtual experimental stress vs. stretch (or strain) curve. This was then used to fit an appropriate material model to determine the parameters for an upper level model. The same procedure was repeated until all the scales under investigation were accounted for.

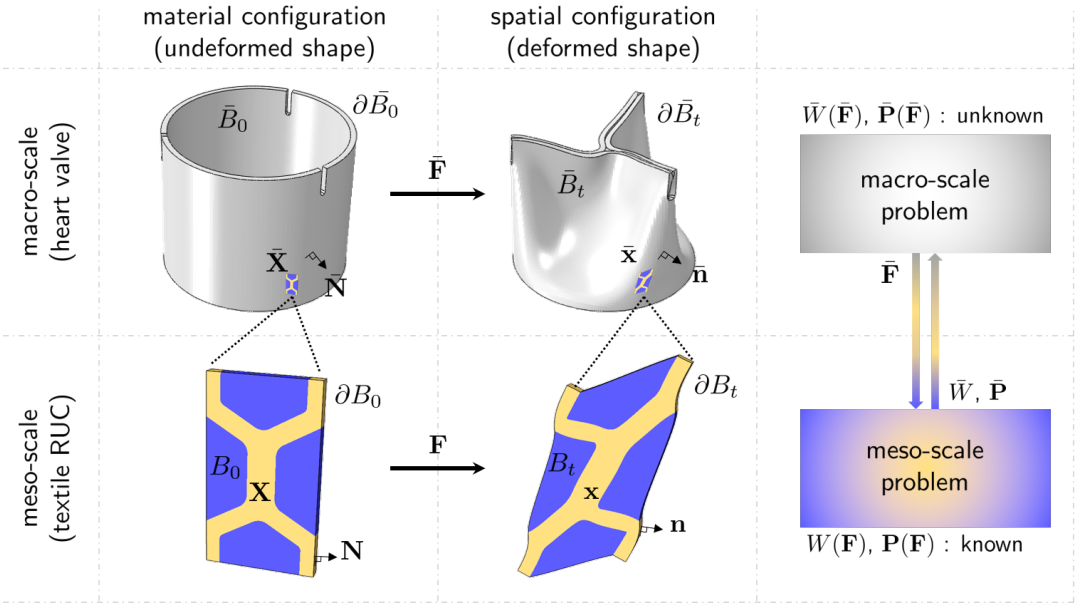

Figure 2.2: Schematic representation of multi-scaling

The approach followed in the present study is restricted to strain-driven computational homogenization. The central idea of this technique is to prescribe the deformation gradient $\bar{\mathbf{F}}$, of the macro-scale (upper-level) onto the structure of the micro-scale (lower-level) and to compute the effective response of the micro-scale, in particular the macro-scale Piola stress $\bar{\mathbf{P}}$ (engineering stress). The micro-scale (lower-level) quantities are related to their macro-scale (upper-level) counterparts through volume averaging over the representative volume element (RVE) or repeating unit cell (RUC). The volume averaging over a domain B_0 with a volume V_0 bounded by the external boundary ∂B_0 is defined

as

$$[(\bullet)] = \frac{1}{V_0}\int_{B_0} (\bullet)\, dV \quad \text{with} \quad V_0 = \int_{B_0} dV \tag{2.7}$$

In the context of material and geometrical non-linearity, the equivalence of strain energy on the micro- and meso-scale is given by the Hill-Mandel condition Saeb et al. [2016], where $\bar{\mathbf{P}} : \delta\bar{\mathbf{F}} - \langle \mathbf{P} : \delta\mathbf{F} \rangle \overset{!}{=} 0$

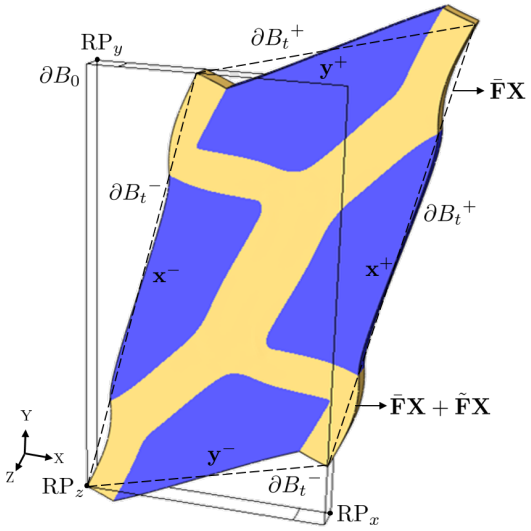

Figure 2.3: Graphical illustration of PBC and LDBC implementation setting. The boundary of the RUC (or RVE) is decomposed into minus and plus parts. Positions of the boundary nodes are determined through the uniform and fluctuation part of the deformation gradient for PBC and only the uniform part for LDBC

The use of periodic displacement-based boundary conditions (PBCs) is a well established technique to fulfil the Hill-Mandel condition and obtain the effective properties/response of a material from its micro-structure, particularly in the context of first-order strain driven homogenization presently used (for example see Bednarcyk et al. [2015]; Sodhani et al. [2015]). The macroscopic kinematic boundary conditions are applied on the nodes which are on the outer surface of the RUC (or RVE). The microscopic deformation gradient is decomposed into a uniform part ($\bar{\mathbf{F}}$) and a fluctuation part ($\tilde{\mathbf{F}}$), i.e., $\mathbf{F} = \bar{\mathbf{F}} + \tilde{\mathbf{F}}$ leading to two

fields contributing to the new position of the boundary nodes, i.e. $\bar{\mathbf{F}}\mathbf{X}$ and $\tilde{\mathbf{F}}\mathbf{X}$ on the surfaces as shown in Fig. 2.3. This results in $\mathbf{x}^+ = \bar{\mathbf{F}}\mathbf{X}^+ + \tilde{\mathbf{F}}\mathbf{X}^+$, $\mathbf{x}^- = \bar{\mathbf{F}}\mathbf{X}^- + \tilde{\mathbf{F}}\mathbf{X}^-$. Periodic boundary condition implementation assumes that the deformation fluctuation on the opposite boundaries are equal in order to maintain C^0 continuity of displacements, resulting in $\mathbf{x}^+ - \mathbf{x}^- = \bar{\mathbf{F}}\,[\mathbf{X}^+ - \mathbf{X}^-]$.

As mentioned earlier, to obtain the effective property at the macro-scale (upper-level), only the micro-stress over B_0 needs to be integrated. To circumvent the computationally expensive volume integral of the micro-stresses, the surface integral in the reference configuration was evaluated as follows:

$$\bar{\mathbf{P}} = \frac{1}{V_0} \int_{B_0} \mathbf{T} \otimes \mathbf{X} \partial B_0 \tag{2.8}$$

where traction $\mathbf{T} = \frac{d\mathbf{f}}{dA}$, i.e., the ratio in force $d\mathbf{f}$ acting on the infinitesimal area dA. The complete far-field strain is described through the displacement of three reference points $\mathrm{RP}_{x,y,z}$. The reaction force in the three Cartesian directions are sampled at the time steps and divided by the original face area of B_0. For large deformations, this results in the engineering stress i.e. the first Piola Kirchoff stress $\bar{\mathbf{P}}$. The macroscopic deformation $\bar{\mathbf{F}}$ is either given or can also be derived using the prescribed far-field displacements. Using these two quantities, further continuum quantities can also be derived. For a detailed understanding of the method please refer Saeb et al. [2016].

A python implementation of the method described in Stier et al. [2013] and applied in Bednarcyk et al. [2015] and Sodhani et al. [2015] was used. For the application of periodic boundary conditions (PBC) in a finite element setting, one has to make sure that the structure being simulated is periodic and that the mesh is also periodic. In case of a non-periodic structure, like in most naturally occurring micro-structure it is not possible to implement PBC Hence, for such cases, linear displacement boundary conditions (LDBC) Saeb et al. [2016] were implemented, which was achieved by only considering the contribution

of the uniform part uniform part ($\bar{\mathbf{F}}$) of the deformation gradient ($\mathbf{F}$).

A graphical summary of the overall multi-scale method used in this work is presented in Fig. 2.4. Initially, we started with an intuitive approach of generating the textile model using CT scans. The properties for the reconstructed textile structure were obtained through micro-scale modelling. After evaluating the advantages and disadvantages of this approach, we introduced an idealized multi-scale approach. In this method, meso- and micro-level models are generated based on geometrical parameters. An intermediate-level was introduced to bridge the gap between micro- and meso-levels. Different intermediate level models were evaluated for their accuracy by comparing the simulation results with the experiments.

2.4.3 Multi-scale modelling using reconstructed geometry from scans

In this approach, geometry of the textile structure in the textile-silicone composite was obtained through CT scans. Because it is still challenging to obtain the individual fibre strands, the textile structure is split into two levels as shown in Fig. 2.5.

The CT scans of the textile-silicone composite were carried out at the Institute of Textile Engineering (ITA) at RWTH Aachen university. Grey scale images across the breadth of the sample were captured with each layer being one voxel thick. The 3D reconstructed geometry along with the top view of the sample are shown in Fig. 2.6. The 3D textile structure with the yarn (fibre bundle) paths and loops was reconstructed from the scans using the Mimics and 3-matic suite from Materialise, Belgium.

In principle, the textile structure in the textile-silicone composite is repetitive in construct (with repeating hexagonal patterns) and computing the entire geometry would be computationally expensive. Hence to save the computational costs, a suitable periodic RUC from the reconstructed geometry was

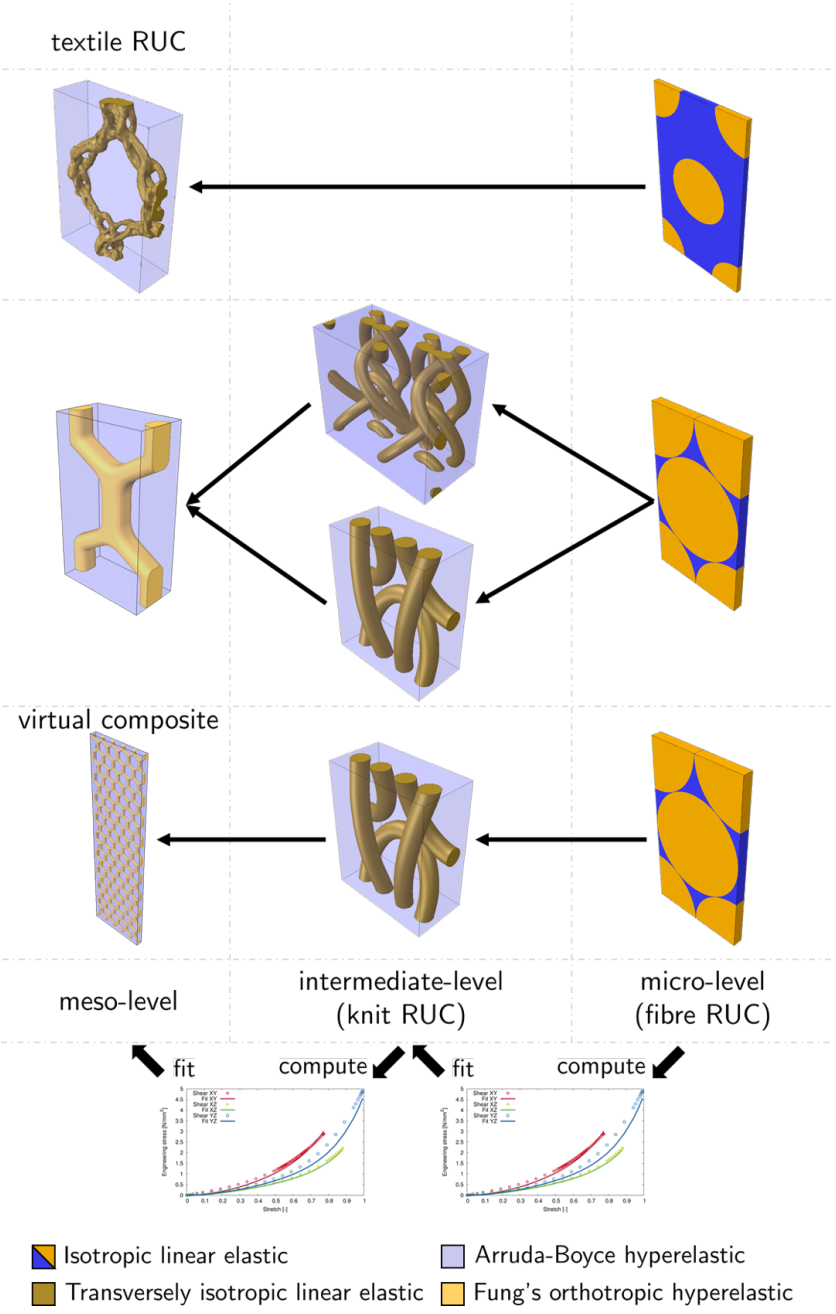

Figure 2.4: Summary of the multi-scale modelling used in this work

selected for the meso-level RUC. The surface of the reconstructed geometry was smoothed in order to obtain a reasonably good mesh quality. The final RUC from the reconstructed geometry is shown in Fig. 2.6.

The RUC from the reconstructed geometry consists of two phases, the silicone

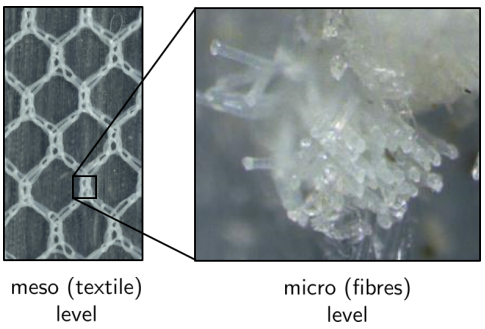

Figure 2.5: The textile-silicone sample has been divided into textile level (meso) and the fibre level (micro)

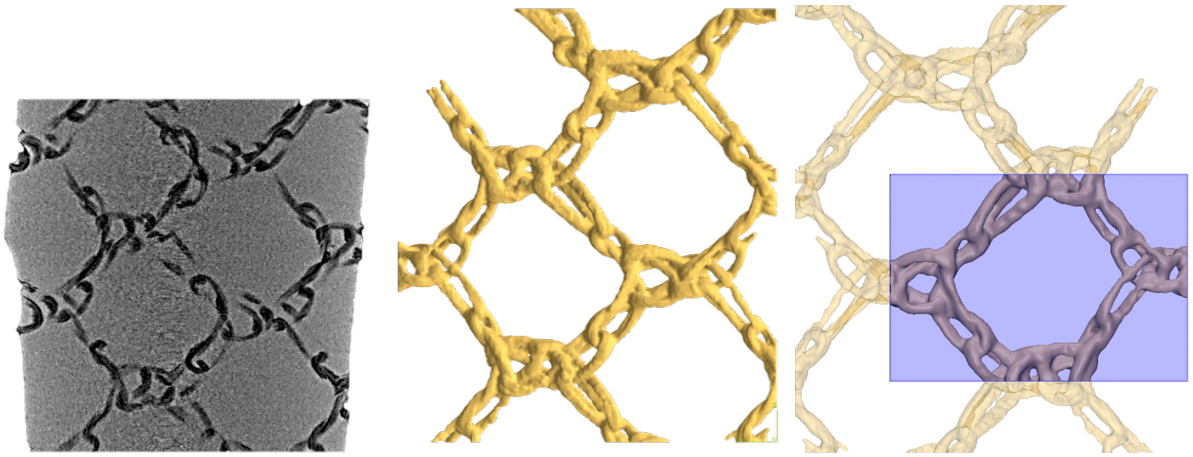

(a) (b) (c)

Figure 2.6: (a) Top view of the centre layer of the CT scans; (b) reconstructed geometry from the CT scans and (c) choice of the suitable RUC

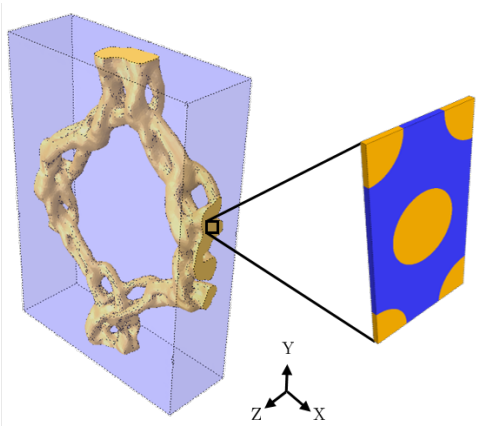

Figure 2.7: Meso- and the micro-levels of the textile structure

matrix and the yarns. Material properties of the silicone matrix were obtained from the experiments. However, material properties of the yarn (fibre bundles) cannot be obtained directly from experiments. Hence, the hierarchical multi-scaling approach was used to derive the material parameters. Considering the fibre volume fraction of the sample (2.54%) and the textile structure in the reconstructed RUC (7.264%), material parameters to model the yarns were obtained by modelling it using a hexagonal dense packing (see Fig. 2.7) with a fibre volume fraction of 34.942% (resulting into the effective fibre volume fraction of 2.54% = 34.942% x 7.264%).

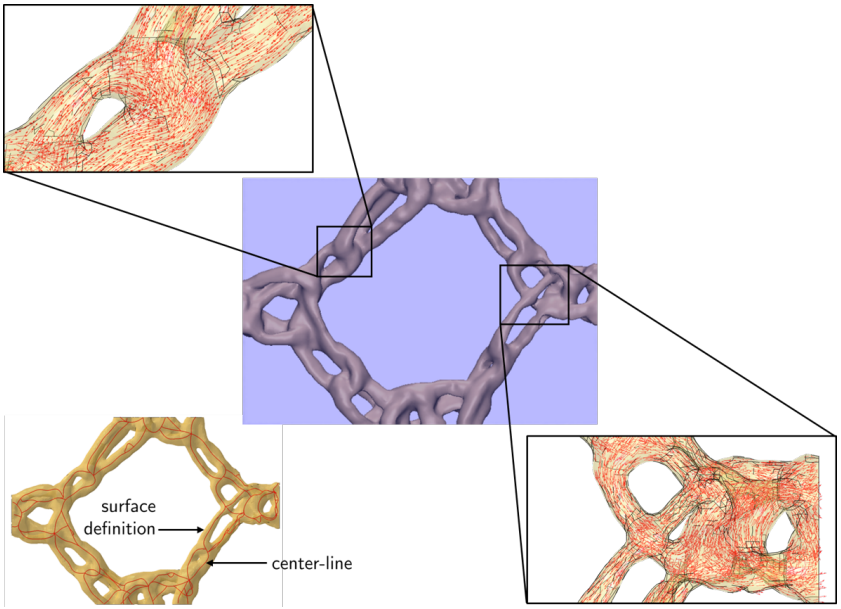

Figure 2.8: Surface & centreline definitions for the textile structure along with the primary direction of the material orientations.

Using this approach, properties of the yarn had to be approximated by transversely isotropic elasticity. In a finite element setting, this could be defined by assigning appropriate material orientations to the gauss points of the elements associated with the yarn. In Abaqus, this could be achieved using a discrete material orientation algorithm, for which the surface definition of the yarn and centre line of the reconstructed textile geometry were required. Both these quantities were obtained from the Mimics and 3-matic suite of Materialise. The

material orientations, centre line and the surface definition of the reconstructed geometry are shown in Fig. 2.8.

It is important to note that the geometry obtained from the scans is not exactly periodic, resulting in a non-periodic mesh. Therefore, we used linear displacements based boundary conditions. It is known to produce relatively stiff results compared to PBCs Saeb et al. [2016], but it is necessary because of the imperfection in the geometry.

2.4.4 Multi-scale modelling using idealized geometry

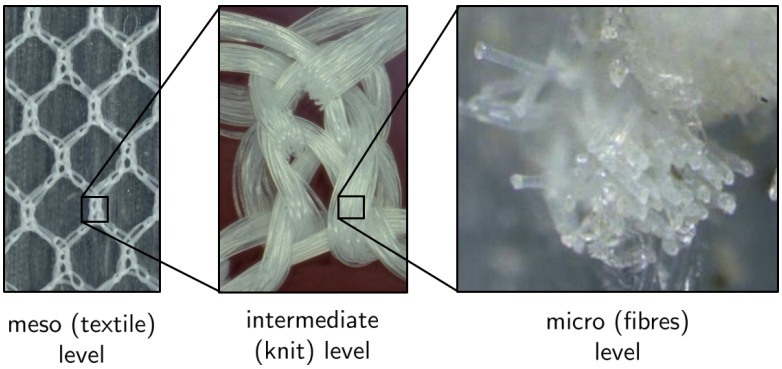

Figure 2.9: Different levels considered when modelling the textile-silicone composite using idealized geometry.

Even though the multi-scale modelling approach presented in the preceding sections stays almost true to the actual geometry, it has its disadvantages. An alternative approach developed using idealized geometries for multi-scale modelling will be discussed in this section. The structure was divided into three levels as shown in Fig. 2.9. One of the primary necessities of this approach was that every idealized level considered is consistent with the overall volume fraction $\approx 2.564\%$ of fibres in the textile-silicone composite. In this approach, we first model the levels for which dimensions can be easily measured or are known, i.e., we first model the meso-level followed by the micro-level. We then introduce an intermediate-level to bridge the gap between meso- and

micro-level models.

Meso (textile) level We start with the textile structure at the meso-level. It was modelled such that a spatial envelope around the complex knitted repeating hexagonal pattern of the textile is modelled using an idealized solid structure as shown in Fig. 2.10. The geometric model which, when repeated in the XY plane, resembles the overall textile structure seen in Fig 2.10a. Dimensions to model the embedded geometry were obtained by calculating the statistical mean of the quantities measured under a microscope; edge length(a), thickness of thinner (t_1) & thicker (t_2) section and angle (θ), which are reported in Table 2.2. Using these dimensions, a 2D wire-frame of the honeycomb textile domain was constructed, extruded and filleted to obtain the desired inclusion geometry. It was observed that the textile layer was located at the mid-plane through the breadth (b) of the sample with some minor undulations along the sample length. The textile layer breadth was one third of the overall sample breadth (b). The RUC was modelled to have the same breadth as the textile-silicone composite with the textile layer restricted to one third RUC breadth. The textile structure and the matrix were modelled using the Fung's orthotropic and isotropic hyperelasticity material models, respectively. Periodic boundary conditions were modified to be applied only to the degree of freedom on the surfaces perpendicular to the XY plane.

From the generated geometry, volume fraction of the embedded textile structure was evaluated to be 15%. Knit and fibre level models were generated keeping in mind the overall fibre volume fraction.

Micro (fibre) level After the meso-level model, the micro-level structure was used to evaluate the material parameters of the yarns. 24 PET fibres with a diameter of 17 μm were assumed to be tightly bundled together in a yarn. Although the number of fibres is not large enough to ignore the edge effects,

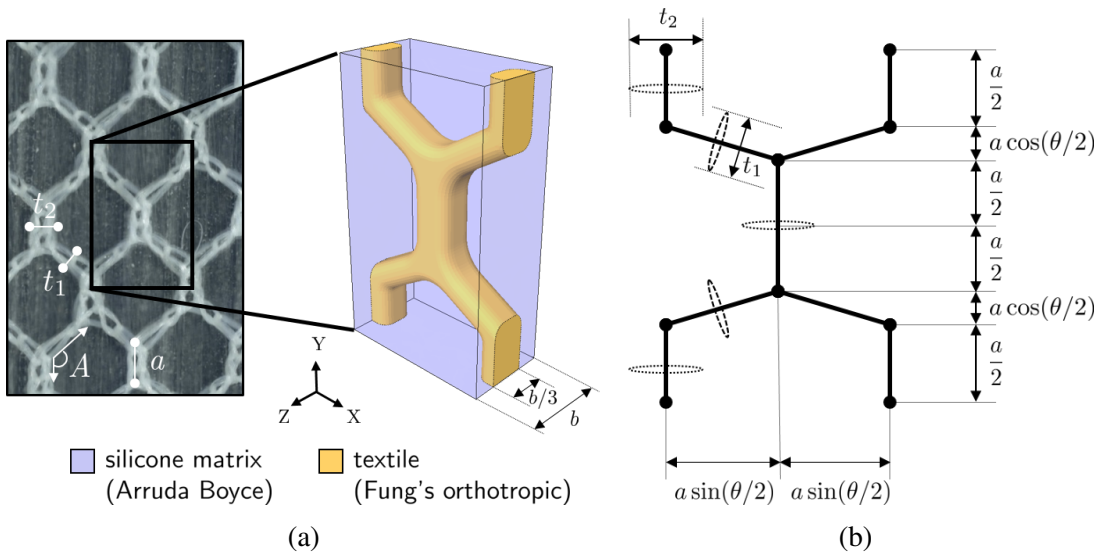

(a) (b)

Figure 2.10: (a) Idealized textile geometry modelled using the dimensions shown; (b) centreline wire model of the textile.

Table 2.2: Dimensions of the meso-level model

Dimension	Values
edge length (a)	1.3560 mm
thinner section ($t1$)	0.4133 mm
thicker section ($t2$)	0.6008 mm
angle (θ)	120°

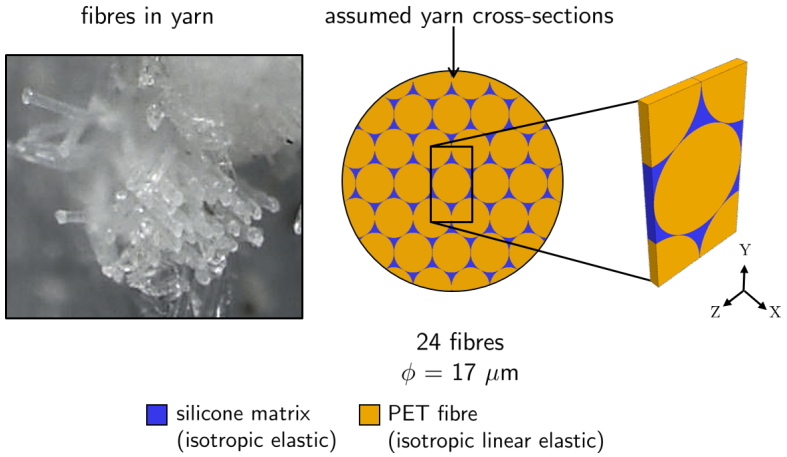

Figure 2.11: Fibre level modelling

the tow was idealized using a hexagonal dense packing RUC considering the assumption of a periodic composite. As a result, modelled yarns have a high

fibre volume fraction which meant that the fibre distribution does not play a role in its effective response. The boundary effects on the peripheral fibres are assumed to be restricted by modelling the yarn with a circular cross-section at the upper-level, having a volume fraction of 90% as shown in Fig. 2.11. The individual material response of the fibres and matrix were captured using a linear elastic material model. The RUC was subjected to a far-field strain of only 1% and PBC Homogenized material response from this level was used to represent the yarn.

Intermediate (knit) level From the different structural levels shown in Fig. 2.9, the meso and micro models were generated using dimensions and geometry which could be easily defined. There is also a distinct scale separation between the two levels (see Table 2.3).

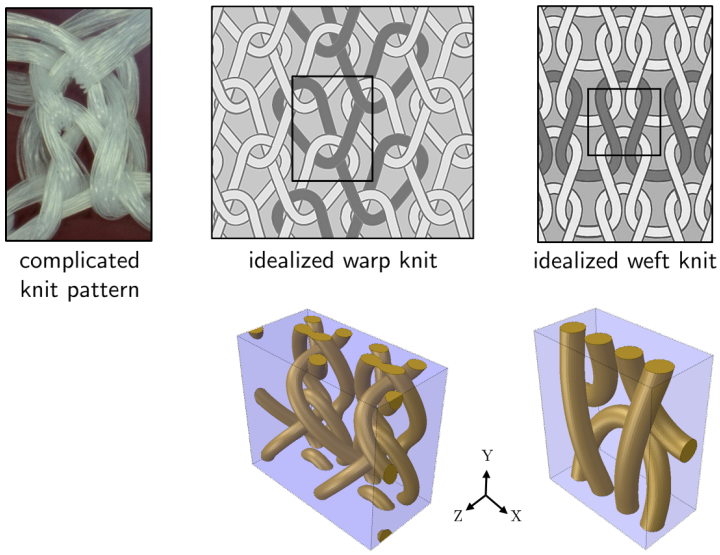

Figure 2.12: Real and idealized knits at the intermediate-level

To bridge the gap between meso and micro-levels, a intermediate-level was introduced, which was modelled using an idealized knit model. Considering the overall fibre volume fraction (i.e. 2.565%) in the textile-silicone composite and having modelled the meso and micro-levels with 15% & 90% fibre volume

fraction, respectively, the intermediate-level had to be modelled using a fibre volume fraction of $\approx$ 19% (i.e. 90%x19%x15% = 2.565%).

Fig. 2.12 shows a close-up of one of many interlocking yarn loops (knit) in the textile. Modelling such a complex looping structure is computationally challenging, expensive and often requires complex multi-contact simulations of the knitting process to achieve the initial unloaded equilibrium geometry. Even though the knitted textiles have a repetitive pattern, it is difficult to identify a consistent path along which the yarns are knit. Hence, it was necessary to simplify the knit for computationally efficient modelling.

In this work, the complex knits were approximated by an idealized warp and weft knit structure, and compared. The warp knit was modelled with TexGen Lin et al. [2011], using the parameters presented in Goktepe and Harlock [2002]; Honglian et al. [2009] and Zhang et al. [2012]. The algorithm used to generate the weft knit has been elaborated in Appendix A. The yarns have a circular cross-section and were assigned transversely isotropic elasticity parameters, which were obtained by homogenizing the micro-level model. The matrix was modelled as isotropic hyperelastic. Intermediate-level RUC were subjected to PBC. The homogenized material response from this level provided the input parameters for textile structure at the meso-level. Care was taken to avoid modelling the contact between fibres or yarns, as it was assumed that silicone would percolate (or the tissue would proliferate - as silicone is a substitute for tissue model) between the fibres and yarns.

Dimensions of all the levels are reported in Table 2.3. It can be observed from the mentioned dimensions that there does not exist a scale separation between the meso and the intermediate-level RUC. The complexity of modelling the textile structure using intricately knitted patterns motivated the use of intermediate level and because it's effective response is averaged over the volume, it may be used to determine the material parameters of the textile at

meso-level. Anisotropy of the yarns was ensured using local orientations.

Table 2.3: Dimensions of the RUCs

Dimension	Micro-level	Intermediate-level (warp knit)	Intermediate-level (weft knit)	Meso-level
length	17.065 μm	1.342 mm	1.342 mm	2.380 mm
width	29.557 μm	1.647 mm	1.647 mm	4.122 mm
breadth	1.706 μm	0.700 mm	0.700 mm	1.245 mm

Virtual textile composite The textile level RUC was generated with an assumption that there were no boundary effects even though the specimen under consideration had a finite width considering the length scales at different levels. This assumption works reasonably well for composites undergoing small deformations with varying length scales, but the same cannot be stated for soft composites undergoing large deformations. Hence, a virtual textile composite that mimics the experimental sample as shown in Fig. 2.13 was generated with an intention to compare the effective response of meso-level RUC with the macro-level full specimen simulation. Only a quarter of the entire sample was modelled and symmetric boundary conditions as shown in the figure were used to simulate the response of an experimental specimen.

Dimension	Values
length	41.22 mm
width	9.58 mm
breadth	1.254 mm

Table 2.4: Dimensions of the virtual textile sample

All the finite element (FE) models were created using the commercial software Abaqus Hibbitt et al. [2001]. The elements used were C3D4 (linear tetrahedral) and C3D8R (eight-node brick elements with reduced integration and enhanced hourglass stiffness) depending on the structural model in consideration. The details of the mesh are reported in Table 2.5. All the structural models were simulated using the implicit (standard) solver of Abaqus.

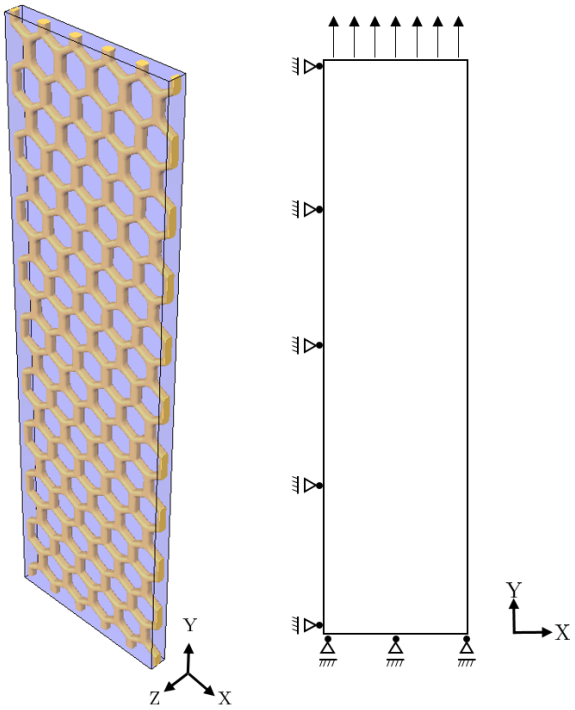

Figure 2.13: Virtual textile composite and the boundary conditions applied on it

Table 2.5: Element type, number of elements and nodes in different geometric models

Models	Elements	Element Type
Micro Recon. geom.	5810	C3D8R
Meso Recon. geom.	585475	C3D4
Micro Ideal geom.	117946	C3D8R
Intermediate-Warp	1107276	C3D4
Intermediate-Weft	921635	C3D4
Meso Ideal geom.	547992	C3D4
Virtual Composite	3320792	C3D4

2.5 Results and Discussions

2.5.1 Material characterization

Constituents of the textile-silicone composite were characterized using uni-axial test data.

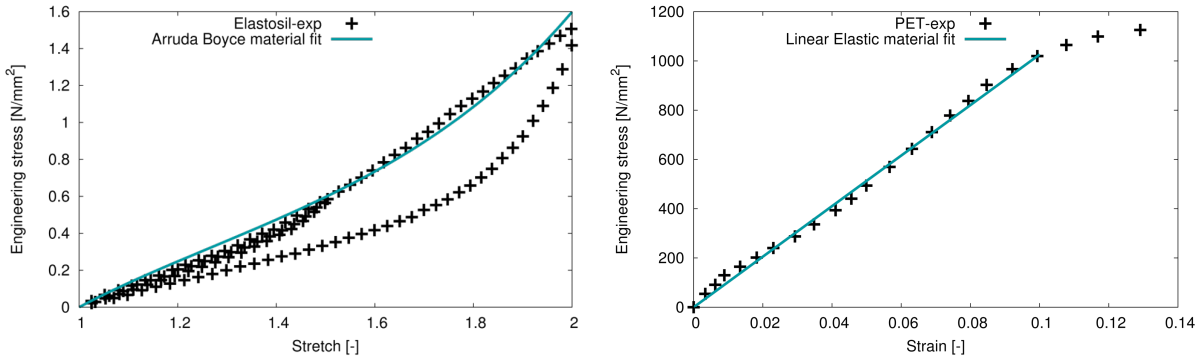

(a) (b)

Figure 2.14: (a) Engineering stress vs. stretch for silicone; (b) Engineering stress vs. strain for PET fibres (Lechat et al. [2011])

Silicone matrix Silicone was tested under cyclic loading using dog-bone specimens to characterize the silicone phase of the composite. Experimental results for the engineering stress vs. stretch is plotted in Fig. 2.14a. Silicone has a hyperelastic material response, which undergoes softening under cyclic loading representing the Mullins' effect. This is because for hyperelastic materials softening only occurs at strains smaller than the maximal applied strain. This implies that if the material is subsequently loaded to a higher strain (compared to the previous cycle), the stress strain relation returns to the path that would have been observed in a single monotonic loading experiment (see Schmoller and Bausch [2013]). Therefore, the silicone matrix is characterized only by the loading curve of both cycles because, the textile-silicone composite is subjected to monotonic uni-axial tensile loading. The silicone matrix was characterized using linear elasticity for the micro model where the elastic constant E was found to be 1.1495 MPa, and all the other levels were characterized by the Arruda and Boyce [1993] model where the constants μ_{ab} and n were found to be 0.2665 MPa and 1.2856 respectively. Silicone was modelled as nearly incompressible.

PET fibres The PET fibre material parameters were obtained by using experimental data from Lechat et al. [2011] as shown in Fig. 2.14b. The stress vs. strain curve is from a tensile test on a single PET fibre. Since plasticity is not included in the present model, part of the curve before the plastic threshold has been approximated by a model of linear elasticity. Young's modulus of the PET fibres was obtained to be $E = 10.259$ GPa and Poisson's ratio ν was assumed to be 0.35.

2.5.2 Multi-scale modelling using reconstructed geometry from scans

In this approach, the geometry obtained by reconstructing the scans was subjected to a virtual tensile test. Material properties for the embedded structure were derived by homogenizing the results of a micro-level RUC (as shown in Fig 2.7) subjected to a far field strain of 1%, resulting in properties of a transversely isotropic elastic type material. The results obtained from the meso-level model were then compared with the experimental results as shown in Fig. 2.15. From the comparison, it can be observed that results from the virtual tensile test are a reasonable match with experimental results until about a global strain of 15% (or a global stretch of 1.15) after which they diverge into a parabolic curve in contrast to an exponential-type experimental curve. Because the meso-level RUC was subjected to a large deformation with geometric non-linearity, the transversely isotropic elastic material used for the textile structure results in a St. Venant-Kirchoff type transversely isotropic elasticity which accounts for the parabolic curve as shown in Fig. 2.15.

Since the effective behaviour of the textile-silicone composite is dominated by stiff fibres, the effective response of the RUC also results in a parabolic curve after the threshold of small deformations. The simulation end in non-converging result. This could be either due to excessively distorting elements at the interface between two materials with a large stiffness contrast or due

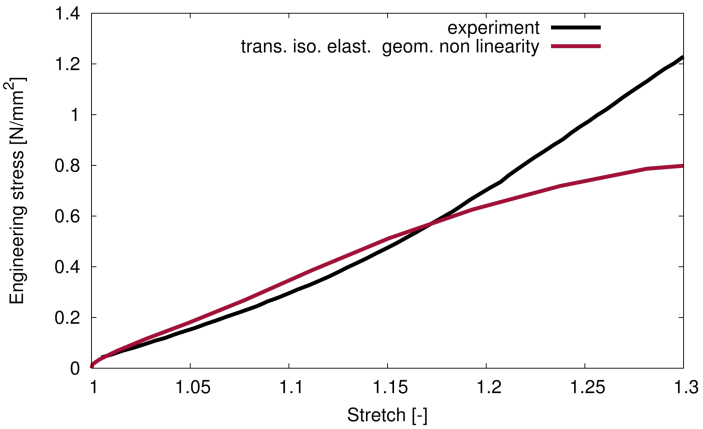

Figure 2.15: Comparison of simulation prediction vs. experimental result for reconstructed geometry

to inherent non physical behaviour of St. Venant-Kirchoff material models under complex loading conditions (especially compression) or both. To get a better prediction from simulation results for higher strains, one would need to improve the mesh quality while further improving the surface definition of the geometry obtained from scans.

Another important observation is that the textile structure has a varying cross-section (see Fig. 2.6, 2.7), implying an inconsistent volume fraction of fibres in different geometric sections. As one yarn only has 24 fibres, the boundary effects of changing textile cross-section cannot be neglected. Thus, the RUC with constant volume fraction to determine the effective material properties of the textile structure is not the most accurate approach.

2.5.3 Multi-scale modelling using idealized geometry

The work flow of this approach is summarized in Fig. 2.4. By applying a far-field strain of 1% to the micro-level model results were homogenized to obtain the effective transversely isotropic elastic material parameters of the yarns at intermediate-level. The far-field strains were applied in all the three uni-axial directions and three shear deformation modes in order to fully popu-

late the elasticity tensor (see Sodhani et al. [2015]). The material parameters, Young's modulus, shear modulus and the Poisson's ratio, were obtained from the compliance tensor (which is the inverse of the stiffness tensor). As mentioned earlier, in this case, the boundary effects on the RUC due to less number of fibres were neglected because yarns in the intermediate-level RUC have a consistent circular cross-section, achieving an uniform volume fraction.

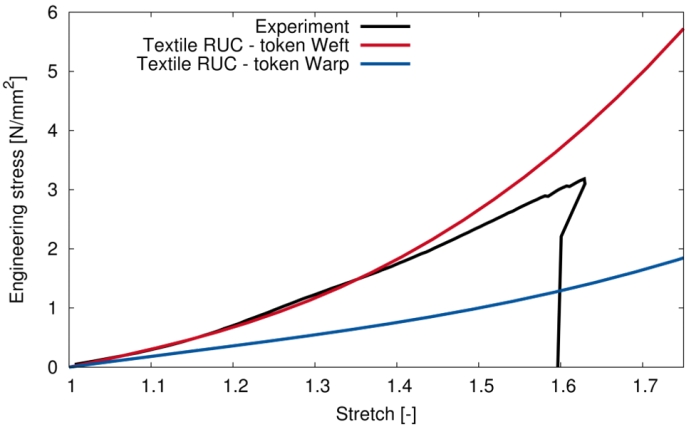

Figure 2.16: Comparison of simulation results compared to the experiments

The warp and weft knit models at the intermediate-level were tested and the same virtual tests were repeated to obtain the effective response. Engineering stress vs. strain/stretch curves were obtained keeping eq. 2.8 in mind. Orthotropic hyperelastic material parameters for textile at the meso-level were obtained by fitting the material model to these curves. The meso-level model was then subjected to uni-axial tension of 75% far field strain and the effective response obtained by the homogenization process was compared to the experimental results as shown in Fig. 2.16.

From the comparison, it is clear that the weft knit intermediate model represents the effective response of the complex knitted structure more closely than the warp knit intermediate model. It is well known in literature that a warp knit textile model is more compliant of the two. The structurally stiff behaviour of the weft knit can be attributed to the presence of two straight yarns in the RUC,

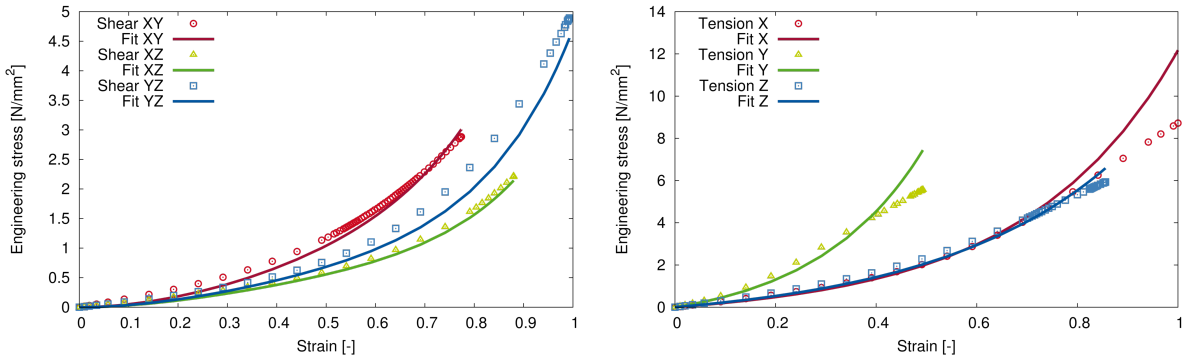

(a) (b)

Figure 2.17: Virtual experiments and their fits using Fung's orthotropic hyperelasticity for warp knit

which have higher resistance to deformation once they align in the loading direction. However, such a yarn is missing in the warp knit allowing it to be more compliant till it reaches a locking stretch. This can be observed from the effective responses of both warp and weft knit when subjected to tensile loading in the Cartesian Y direction (see Fig. 2.17b, 2.18c). The effective response of the virtual testing carried out on the intermediate-level models were fitted using Fung's orthotropic hyperelastic material model.

The material response of the meso-level with properties from the weft intermediate level model (see Fig. 2.16) is in good agreement with the experimental result until a global strain of 40% following which it diverges. The good agreement of the stress-strain response at relatively low strains can be attributed to the accurate realization of the scaffolding structures and the overall volume fraction of fibres in the composite. Divergence of the simulation results to a stiffer response can be associated with the following reasons; (i) matrix damage leading to localized damage, de-lamination (similar to Maurer et al. [2014]) or void formation resulting in matrix softening was not considered; (ii) idealization of the underlying intermediate-level does not accurately capture the mechanics of knitted textile at large deformations.

The Mises stress and logarithmic strain contour plots are shown in Fig. 2.19a

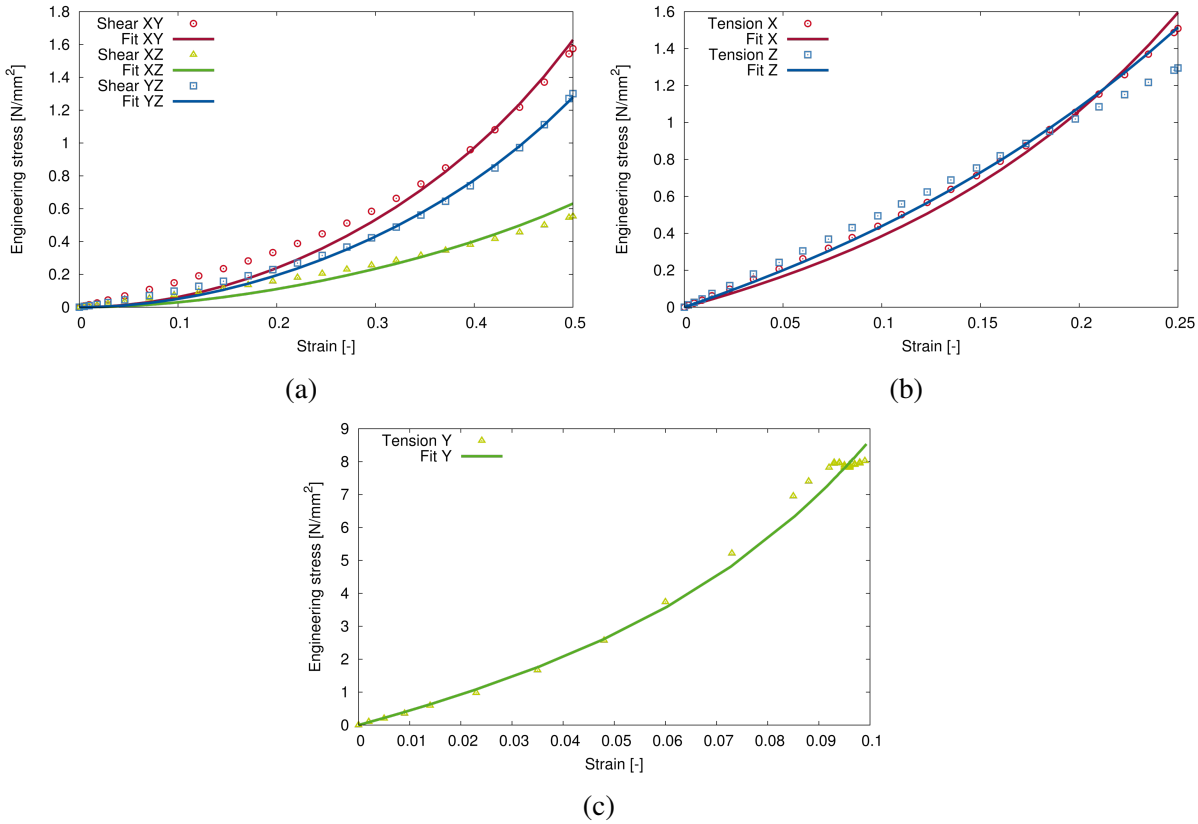

Figure 2.18: Virtual experiments and their fits using Fung's orthotropic hyperelasticity for weft knit

and 2.19b. It can be observed that the strains localize in the pure silicone matrix pockets. For a global strain of 75% the matrix strains is around 90%. The localization is not very high because of the low fibre volume fraction in the composite.

Comparing the dimensions of the meso-level RUC to that of the textile sample (see Table 2.1 & 2.3), one can conclude that there might not be a significant scale difference between the two levels, implying that the meso-level cannot be assumed to be free of boundary effects, which is a fundamental assumption for applying the periodic boundary conditions. Hence, to quantify the error introduced by modelling the textile using a simplified meso model, the virtual composite geometry with the textile structure was generated and subjected to uni-axial tensile loading. One can observe a prominent Poisson's effect

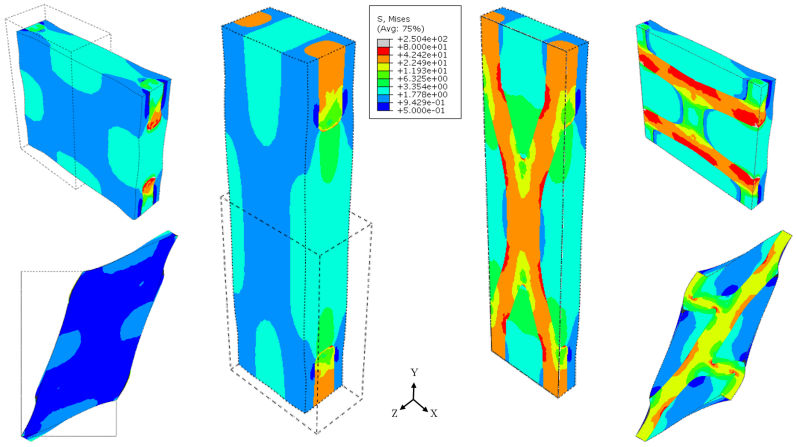

(a) Mises stress contour plots on surface and at the mid-plane of the meso-level model with uni-axial and shear loading

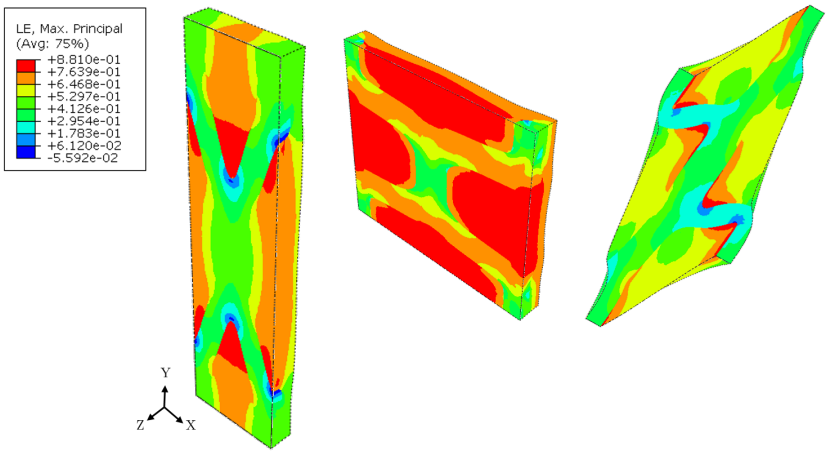

(b) Logarithmic strain contour plots at the mid-plane of the meso-level model with uni-axial and shear loading

Figure 2.19: Contour plots of the meso-level model

in both the Textile RUC and the virtual composite models as seen in Fig. 2.20a, i.e., there is a proportional decrease in the lateral measurement to the corresponding increase in length. Although the effective response of both the models is overlaying one another, there is an error of $\approx 10\%$ introduced in the Poisson's effect. This implies that the boundary effects under tension were not accurately captured by the RUC. Since the textile-silicone (or textile-tissue) composite is used as a heart valve which undergoes large bending deformation

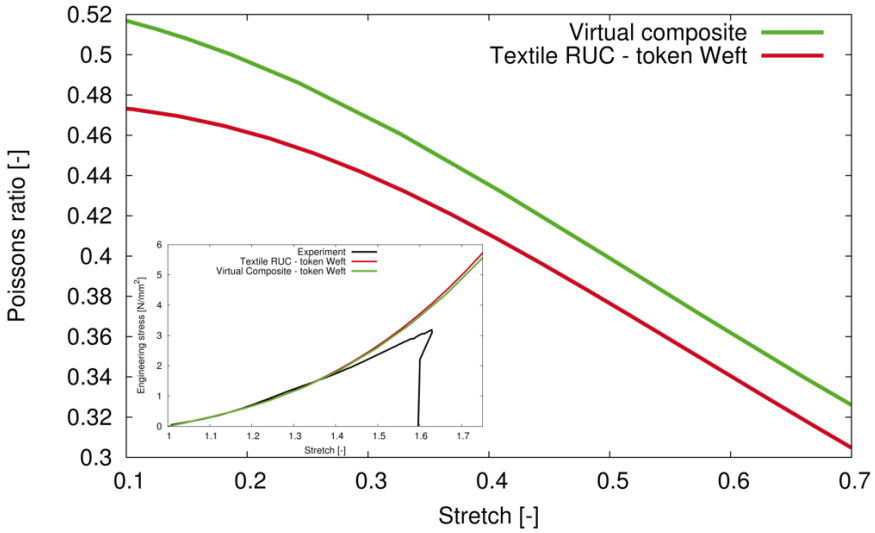

(a) Comparison of the lateral contraction with longitudinal stretch

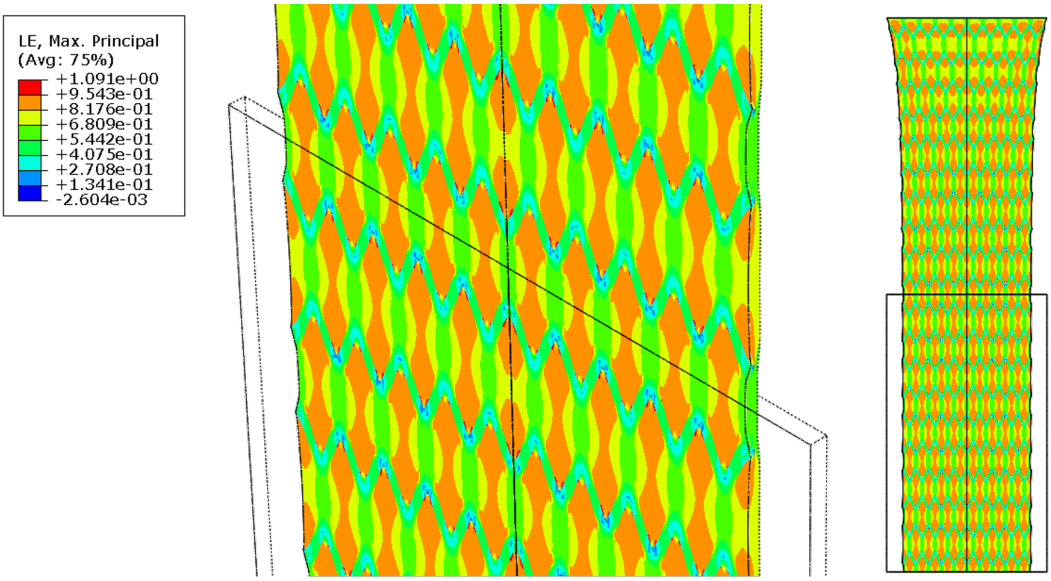

(b) Logarithmic strain contour plots at the mid-plane of virtual textile composite

Figure 2.20: Poisson's ratio comparison and contour plots of the virtual textile

(rotations) and relatively small stretches, we considered the results obtained from the virtual experiments of the RUC as a trade off between numerical accuracy and computational effort.

The presented method was already applied to derive the material properties of a textile-silicone based heart valve, where more complex virtual experiments were carried out on the meso (textile) level model to obtain the effective

response of the heart valve (see Sodhani et al. [2016]). Structural kinematics of the heart valve were also found to be in good agreement with those of the tissue-engineered heart valve.

All the material parameters obtained using virtual experiments are reported in Table 2.6. The results obtained were fitted using a Monte Carlo multi-curve fitting algorithm. At first, the tensile tests were used to fit the corresponding parameters. Keeping the obtained parameters fixed, the remaining parameters were fitted to the shear response.

Table 2.6: Parameters obtained by fitting corresponding models to virtual experiments

Parameters Trans. Iso.	Micro Recon. geom.	Micro Ideal geom.	Parameters Fung's ortho.	Intermediate -Weft	Intermediate -Warp
E_p	3.208	521.57	c	1.241	4.701
E_n	3585.4	9233.09	λ	11.621	16.796
μ_{np}	0.8	21.47	b_1	2.683	0.249
μ_p	0.824	183.49	b_2	38.792	0.915
ν_p	0.9459	0.422	b_3	1.959	0.246
ν_{np}	0.000394	0.020	b_4	20.524	4.462
			b_5	10.463	3.046
			b_6	17.088	3.421
			b_7	2.498	0.079
			b_8	0.570	0.020
			b_9	1.501	0.230

2.6 Conclusion and Outlook

The aim of the current study was to show the competence of a hierarchical multi-scale modelling approach to predict the behaviour of biocompatible materials. Initially, real geometry was generated using CT scans and compared with the experimental results. The complex structure of the textile reinforced composite was then reduced to simplified models at meso and micro-levels. Structural disparity between these two levels was bridged using a intermediate-level (similar to calibrating), which was chosen such that it predicted the results

that were in good agreement with those from the experiments. The presented multi-scale technique could be used to study knitted textile-tissue composites which are otherwise difficult to experiment on and optimize for their mechanical compatibility. Apart from predicting the global response, the current approach can also predict non-affine local deformation along with the stress and strain states in the matrix - to better engineer the ingrowth of tissues. Such a method could be used to optimize the textile structure along with its orientation saving on both time and resources while improving the end product.

The approach can be made more reliable and robust by further investigations to quantify the deviation of global and local responses due to the changes in volume fraction of individual structural levels ensuring the effective fibre volume fraction. Investigations are also needed to determine the effect of different idealized knit patterns and varying the cross-section at the intermediate-level on the overall results. This would aid in creating a library of intermediate-level models, which could be used analogously to a "plug and play" approach.

The presented approach could eventually aid in improved understanding of engineered tissue in presence of a scaffold (textile mesh) leading to improved biocompatible topologies.

2.7 Appendix - Modelling knit level RUC

The complex knit structure was idealized using a weft knit RUC which contains segments from four identical weft knit loops as shown in Fig. 2.21. Modelling of the weft knit loops entails parametric spline generation for the yarn path based on structural points defining the loop (Fig. 2.22, Table 2.7). Methods for solid modelling of realistic yarn loops for plain weft knits using splines, have been previously presented by Kyosev et al. [2005] and Li et al. [2014].

In the current approach, the yarn path was modelled using NURBS and a circular cross section was swept along it. All the structural parameters

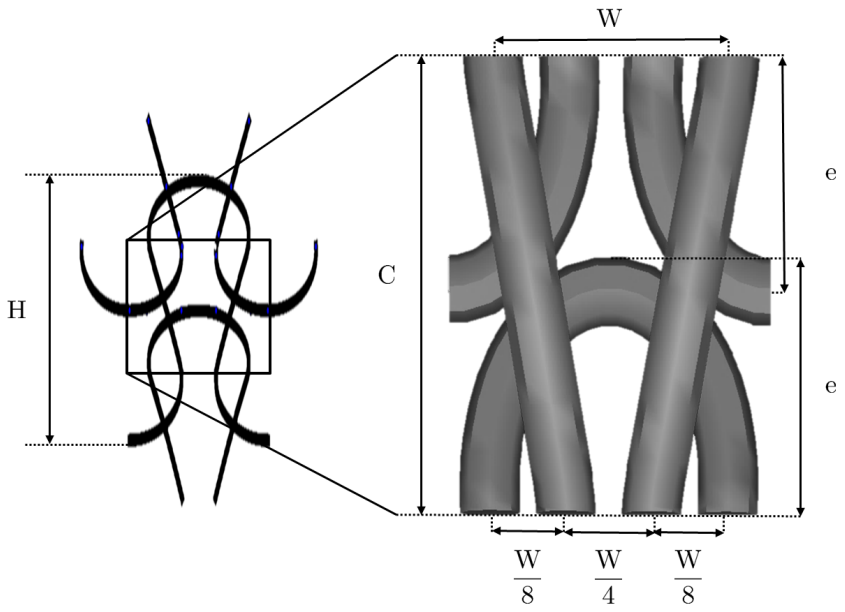

Figure 2.21: Kint level RUC model with structural parameters and dimensions

Table 2.7: Structural parameters for defining the weft knit loop

Loop dimension	Relationship
Wale length	$W = f_1 * (1.2d)$B
Loop height	$H = f_2 * W$
Course length	$C = H/2$
Overlapping length	$e = H/4$
Bend thickness	$T = f_3 * (1.5d)$

were formulated as a function of yarn diameter d, controlled using variables f_1>4,f_2>1, and f_3>1. These variables uniquely define the structure of a weft knit. Values of f_1,f_2,f_3 were constrained to ensure that the generated weft knit RUC passes through the nine 3D form defining structural points P_i as elaborated in Fig. 2.22. Although these constraints ensure no intersections between yarns at these structural points, choice of the control points C_i guiding the spline between these points can lead to intersections between yarns (see Fig. 2.23). Therefore, a quantitative and qualitative study for generation of an acceptable weft knit configuration was needed. A weft knit model devoid of intersections or contact between yarns was considered as an acceptable configuration.

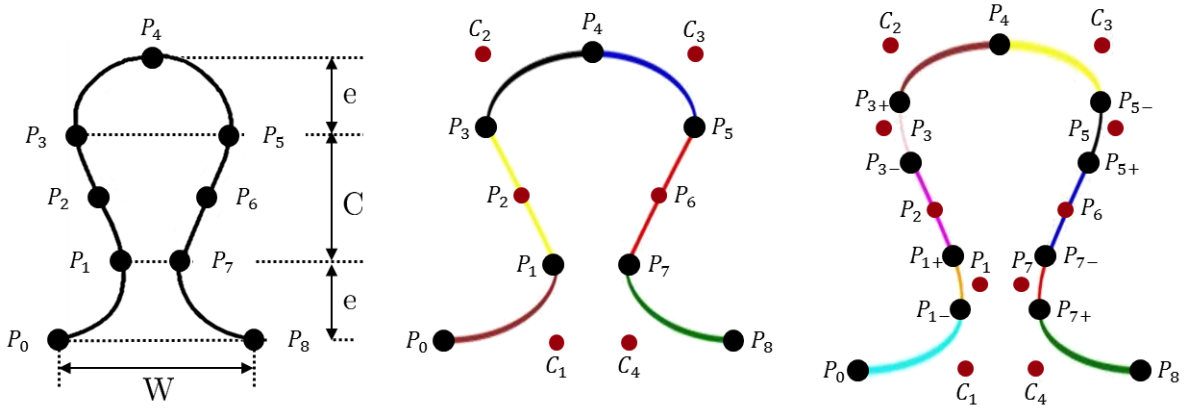

Figure 2.22: Left to right: structural points of a weft knit loop; six spline segments passing through the structural points P_i of the loop; ten spline segments for filleted weft knit loop

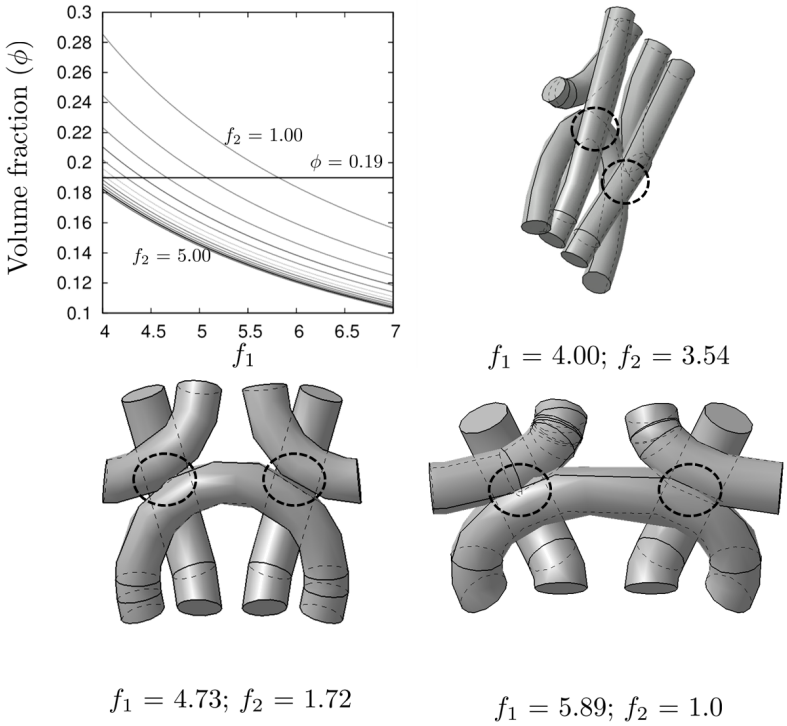

Figure 2.23: Volume change and intersection in generated geometry for the parameter set [d = 0.086 mm, f_3 = 1.0]

The weft knit loop was initially generated using the primary structural points [P_i with $i = 1..8$] and control points [C_i with $i = 1..4$]. At this stage, the spline

segments at the structural points are C^0 continuous. But to model the RUC, the weft knit loop should be at least C^1 continuous at these points. Hence, filleting of the loop was introduced by adding additional structural points (Fig. 2.22). The coordinates of these points, along with their weights and knot vector, is given in Table 2.8

An important aspect to modelling the weft knit RUC is to maintain its volume fraction. Volume of the splines was computed numerically by linearising the splines. In the absence of an inverse solution for modelling an acceptable weft knit configurations for a given volume fraction, a forward solution was required. This involved iterative generation of weft knit configurations. Contact/intersections along the width, height and thickness directions could be removed by increasing the values of any one of the structural variables f_1,f_2 and f_3, respectively. For a constant volume fraction, increasing one of these variables leads to a decrease in the values of the other two parameters. Thus, removing intersections in one direction can lead to an intersection in other directions.

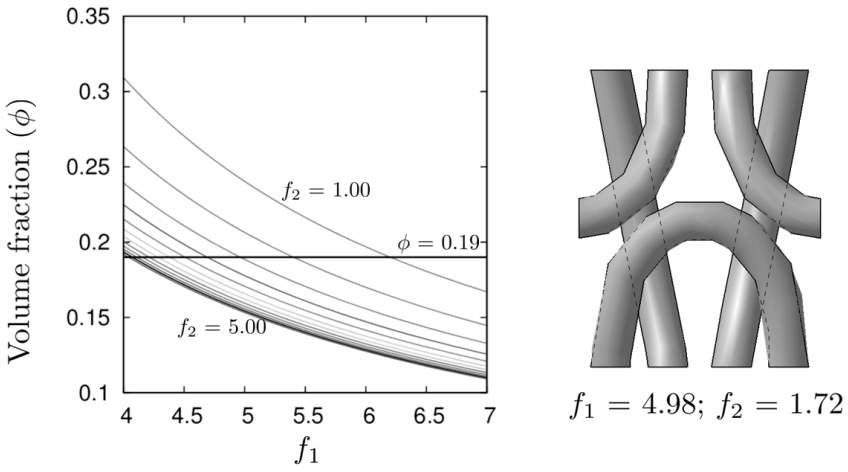

Figure 2.24: Geometric model of acceptable configurations (no intersections): [d = 0.110 mm; f_3 = 1.2]

The change of volume fraction when varying f_1 and f_2 for constant yarn

Table 2.8: Co-ordinates of the structural, control and guiding points are mentioned in the table below. These are used to generate the filleted weft knit loop segments for the knit level RUC.

Structural points	Co-ordinates	Weights
P_0	[-W/2,0,0]	1
C_1	[-W/8,0,0]	$1/\sqrt{2}$
P_{1-}	curv1(0.8)	1
P_1	[-W/8,e,2eT/H]	$1/\sqrt{2}$
P_{1+}	curv2(0.2)	1
P_2	[-W/4,e+(C/2),(2(e+C/2)/H)T]	1
P_{3-}	curv2(0.8)	1
P_3	[-3W/8,e+C,(2-2(e+C)/H)T]	$1/\sqrt{2}$
P_{3+}	curv3(0.2)	1
C_2	[-3W/8,C+2e,0]	$1/\sqrt{2}$
P_4	[0,C+2e,0]	1
C_3	[3W/8,C+2e,0]	$1/\sqrt{2}$
P_{5-}	curv4(0.8)	1
P_5	[3W/8,C+e,2(1-(C+e)/H)T]	$1/\sqrt{2}$
P_{5+}	curv5(0.2)	1
P_6	[W/4,e+C/2,2((e+C/2)/H)T]	$1/\sqrt{2}$
P_{7-}	[-W/4,e+C/2,(2(e+C/2)/H)T]	1
P_7	[W/8,e,2(e/H)T]	$1/\sqrt{2}$
P_{7+}	curv6(0.2)	1
C_4	[W/8,0,0]	$1/\sqrt{2}$
P_8	[W/2,0,0]	1
Weft knit spline loop construction		
Structural points = $[P_0, C_1, P_{1-}, P_1, P_{1+}, P_2, P_{3-}, P_3, P_{3+}, C_2, P_4, C_3, P_{5-}, P_5, P_{5+}, P_6, P_{7-}, P_7, P_{7+}, C_4, P_8]$		
Weights = $[1, 1/\sqrt{2}, 1, 1/\sqrt{2}, 1, 1/\sqrt{2}, 1, 1, 1, 1/\sqrt{2}, 1, 1/\sqrt{2}, 1, 1/\sqrt{2}, 1, 1/\sqrt{2}, 1, 1/\sqrt{2}, 1, 1/\sqrt{2}, 1]$		
Knot vector = $[0, 0, 0, 1, 1, 2, 2, 3, 3, 4, 4, 5, 5, 6, 6, 7, 7, 8, 8, 9, 9, 10, 10, 10]$		

diameter (d) and RUC thickness (f_3) is shown in Fig. 2.23 and Fig. 2.24. Figure 2.23, shows three different weft knit models generated for a volume fraction of 19% with varying combinations of [f_1,f_2] for a constant diameter of $d = 86\mu m$ and thickness $f_3 = 1$. All three configurations have intersections in different locations within the model. Increasing the radius of the yarn leads to an affine expansion of the weft knit configuration, which tends towards optimal

values of $[f_1, f_2, f_3]$ for an acceptable weft knit configuration. In Fig. 2.24, weft knit configuration for a yarn diameter $d = 110\mu m$ for $f_3 = 1.2$ is shown. The weft knit configuration obtained had no yarn intersections which has been used for further computations. Transversely isotropic linear elastic material model was used to represent the yarns (homogenized fibres), for which the material parameters were obtained from the effective response of the fibre level RUC.

3 Article 2: Multi-scale modelling of textile reinforced artificial tubular aortic heart valves

This article was published as:

Sodhani D, Reese S, Moreira R, Jockenhoevel S, Mela P, Stapleton SE. Multi-scale modelling of textile reinforced artificial tubular aortic heart valves. Meccanica. 2017 Feb 1;52(3):677-93.

Disclosure of the individual authors' contributions to the article:

D. Sodhani conceptualized the multi-scale modelling technique, generated the required geometries and carried out the simulations; P. Mela & R. Moreira conducted the in-vitro experiments provided intellectual content and gave conceptual advice; S.E. Stapleton provided the python script for fitting anisotropic material models along with intellectual content and gave conceptual advice; S. Reese & S. Jockenhövel provided intellectual content and gave conceptual advice; S. Reese, P. Mela and S.E. Stapleton were engaged in obtaining funds for the research; All authors drafted the work for intellectual content; All authors approved the publication of the final manuscript.

3.1 Abstract

Tissue engineered heart valves equivalent to the native aortic heart valves are in development as an alternative to available prostheses. To achieve sufficient mechanical stiffness for application in tissue engineered valves exposed to the systemic circulation, the tissue is reinforced by a textile scaffold. Mechanical testing of structurally different textiles used as reinforcement in tissue engineered heart valves is expensive and time-consuming. The current study seeks to predict the behaviour of textile reinforced artificial heart valves using a multi-scale modelling approach. The complex textile structure was divided into simplified models at different scales. Virtual experiments were conducted on each of these models and their response was fitted by appropriate isotropic and anisotropic hyperelastic material models. The textile response was then used in a macro heart valve model, which was subjected to dynamic cardiac loading. It was shown that the current modelling approach is in good agreement with the real valve behaviour.

3.2 Introduction

Valvular heart disease is characterized by damage to or a defect in one of the four heart valves: the mitral, aortic, tricuspid or pulmonary. We focus our attention on the aortic valve, which governs blood flow between the heart's left ventricle and the aorta, and thereby the blood vessels leading to the rest of the body. Normally, functioning valves ensure that blood flows with proper force in the proper direction at the proper time. In valvular heart disease, the valves become too narrow and hardened (stenotic) to fully open, or are unable to close completely (incompetent). This leads to a malfunctioning heart due to the thickening of heart muscle or forming of blood clots Iung and Vahanian [2011]; Novaro [2014].

Medical treatment depends upon the extent of the disease. One suitable treatment for the stenosis of aortic valve is transcatheter aortic valve replacement which delivers an artificial valve to the site of the diseased valve through a catheter. In the recent past there is a considerable interest in developing artificial aortic tissue engineered heart valves (TEHVs). Tissue engineering (TE) of heart valves might overcome the well-known complications of contemporary devices such as the need for a life-long anticoagulation therapy in the case of mechanical prostheses Padala et al. [2011]; Pibarot and Dumesnil [2009], the degeneration and therefore limited durability of the biological heart valves Padala et al. [2011]; Pibarot and Dumesnil [2009] and the limited availability of homografts Llames et al. [2012]. The ultimate goal is to provide the patient with an implant produced with and by the patient's own cells, able to remodel and self-repair, with physiological haemocompatibility, biologically and mechanically equivalent to the native tissue. Different kinds of TEHVs are in development by various groups. One such TEHVs is being developed by the group at the Applied Medical Engineering institute of RWTH Aachen University Weber et al. [2013], as shown in Fig. 3.1.

Since experimental testing of different TEHVs can be extremely time-consuming and expensive, numerical models are desired to predict the effect of geometrical and material changes on performance. Hence, to predict the behaviour of the artificial heart valve, which is basically a textile reinforced elastomeric composite, a well known approach in the field of composites known as multi-scale modelling is employed. In this paper, we try to establish the validity of the approach for soft biological composites. Once the framework is set up, virtual testing and prediction of suitability of various soft biological composites in artificial heart valves can be developed into a very efficient tool for artificial heart valve development.

Various works on multi-scale modelling of heart valves exist in literature,

where the problem at hand is tackled at organ, tissue, cell and molecular scales Weinberg and Mofrad [2007]; Weinberg et al. [2010]. In these approaches, the material characteristics of the higher scale is obtained from the lower scale, whereas the response of the underlying structure is often not accounted for clearly. Argento et al. [2012] present an approach of mechanical characterization of the scaffolds for tissue engineered heart valves, by accounting for the effect of underlying scaffold structure, which is similar to the approach presented in this paper. In this work, the complex structure of the textile is divided into three simplified structural level models. The effective response obtained after conducting virtual experiments at the lower level model is used to represent the behaviour at a higher level. In this manner the behaviour of the textile embedded into the matrix is obtained. This effective response of the textile is then used to simulate the artificial textile reinforced heart valve under realistic loading conditions.

This paper is organized as follows. Initially a brief introduction is given to artificial aortic heart valves (section 3.3). The structural multi-scale levels, along with a small introduction to the modelling approach is provided in section 3.4. This is followed by a brief overview of the constitutive material models used in this paper (section 3.5). The results are discussed in section 3.6. This paper then ends with a conclusion and an outlook.

3.3 Artificial aortic heart valves

The tube-in-stent valve consists of a tubular tissue engineered fibrin based construct sewn into a stent at three single attachment points and along a circumferential line at the annulus according to the single point attachment commissure (SPAC) technique Goetz et al. [2002]. The valves are produced by using fibrin gel as a cell carrier embedding vascular cells isolated from human umbilical cord veins and a tubular knitted textile structure as a co-scaffold Moreira et al.

[2014b]. Initially, the knitted polyethylene terephthalate (PET) mesh is embedded into the fibrin gel containing the cells. The tubular mesh construct is fixed during the static cultivation for one week after which it is sutured into a self-expandable nitinol stent. First the construct is sewn at the three single points to form the commissure points and then circumferentially to define the annulus (Fig. 3.1).

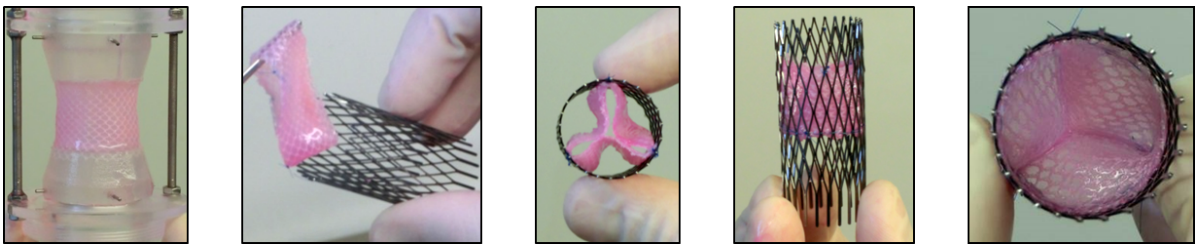

Figure 3.1: Fabrication of the tube-in-stent valve. From left to right: tubular construct after one week of static cultivation still fixed at the silicone connectors, after release from the silicone connectors and placed into the stent, after suturing at the three commissure points and at the base of the tubular construct circumferentially (annulus) Moreira et al. [2014a]

After static conditioning, the TEHV is conditioned for 14 days in a custom-made bioreactor positioned in an incubator. With the use of actuators and membranes the bioreactor is able to mimic the flow between the ventricle and the aorta. The valve is tested under aortic flow and pressure conditions according to ISO 5840-3 i.e., cardiac output of 5L/min, 100 mmHg mean aortic pressure and 70 bpm (beats per minute) frequency. The pressures are measured by pressure transducers positioned immediately upstream and downstream from the valves. The instantaneous flow is measured by a flow meter positioned upstream from the valves. Pressure and flow values are recorded by a LabVIEW^{TM} application.

For the ease of production, testing and simulation, silicone, whose mechanical properties are similar to that of engineered tissues Martins et al. [2006], is used in this study as a replacement for tissues. The silicone based heart valve is subjected to the same process as a tissue engineered heart valve, except for

the cultivation period.

3.4 Finite element simulations

TEHVs used in this study can be treated as a composite at the macro level, where the textile made by knitting multiple yarns (bundled fibres) is used as a scaffold on which the engineered tissues are grown (see Fig. 3.2). Hence, to predict the behaviour of a TEHVs, one needs to understand the structural response of its constituents at different levels. Therefore, a multi-scale modelling approach is employed. The benefit of this approach is that individual components of the composite can be modelled by means of a simple material model which can be characterized using simple experiments. The effective response of the material over different scales can then be obtained from virtual experiments.

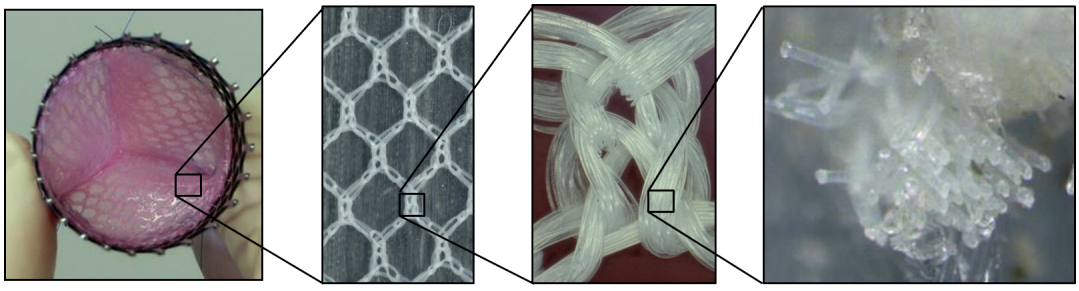

Figure 3.2: Different structural levels of TEHVs

All the finite element (FE) models are created using the commercial software Abaqus Hibbitt et al. [2001]. The elements used are C3D4 (linear tetrahedral) and C3D8R (eight-noded brick elements with reduced integration and enhanced hourglass stiffness) depending on the structural model in consideration. All the structural models are simulated using the implicit (standard) solver of Abaqus, whereas the heart valve model is solved using the explicit solver. Only the material models built into Abaqus are used in this work.

3.4.1 Multiscale modelling

The micro-structure has been simplified and divided into four levels. The schematic representation of the different levels used in multi-scale modelling is shown in Fig. 3.3. The modelling approach of repeating unit cells (RUC) Hassani and Hinton [1998] is implemented at textile, knit and fibre levels. A unit cell, when repeated in all or specified directions, represents the micro-structure, i.e. the structure is periodic along the pre-defined directions. Virtual experiments are conducted at a lower level RUC which then produces the effective material response. This effective material response is subsequently fitted by another material model used to represent the behaviour of the internal structure within the RUC at a higher level. The same procedure is repeated until all the scales under investigation are accounted for. This approach is often referred to as hierarchical multi-scaling Bednarcyk et al. [2015]. For the structures that are periodic, displacement based periodic boundary conditions (PBCs) are used for the prediction of effective material response Bednarcyk et al. [2015]. At the different levels different material models are utilized (see also Fig. 3.3). These models are briefly discussed in section 3.5.

Silicone matrix and the PET fibres are characterized using experimental results, whereas virtual experiments conducted on the RUC are used to characterize the material properties of the internal structure in a higher level RUC. All the material properties obtained are mentioned in the sections below.

3.4.2 Fibre level structural model

The fibre level represents the micro-structure of the yarn. 24 PET fibres with a diameter of 17 μm are bundled together as a yarn. Within a yarn, it is assumed that all the fibres are aligned in the direction of the yarn. Although the number of fibres is probably not large enough to ignore the edge effects, the tow was idealized using a hexagonal dense packing (HDP) RUC considering

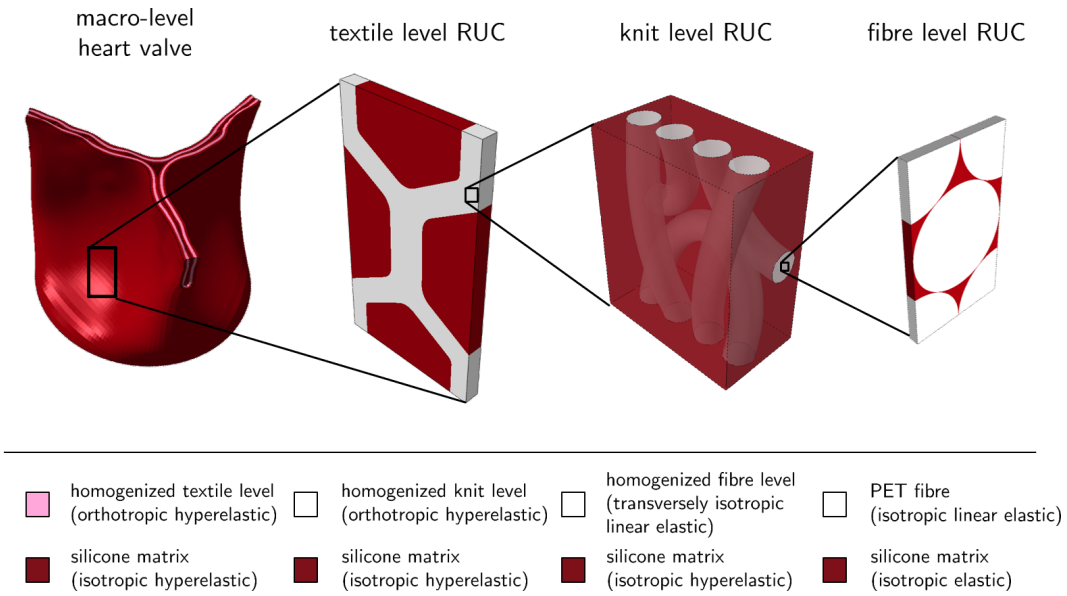

Figure 3.3: Schematic representation of multi-scale modelling of the heart valve

the assumption of a periodic composite. The boundary effects on the peripheral fibres are assumed to be restricted by modelling the yarn in the knit level model using a circular cross-section, with a volume fraction of 90%.. Therefore, the HDP RUC is modelled with a volume fraction of 90% as shown in Fig. 3.4. The material response of the fibres and the matrix are captured using a linear elastic material model. The homogenized material response from this level is used to represent the yarn in the knit level. The mesh of the fibre level structural model has 1061514 C3D8R elements.

3.4.3 Knit level structural model

Fig. 3.5 shows some of the knit patterns in the textile. Multiple yarns are knit together to form a textile. The knitted textile mesh was produced at the Institute of Textile Technology (RWTH Aachen University) using medical grade PET multi-filament fibres.

Modelling such a complex knit pattern is computationally challenging and expensive. As it can be observed, even though the kitted textile has a repetitive

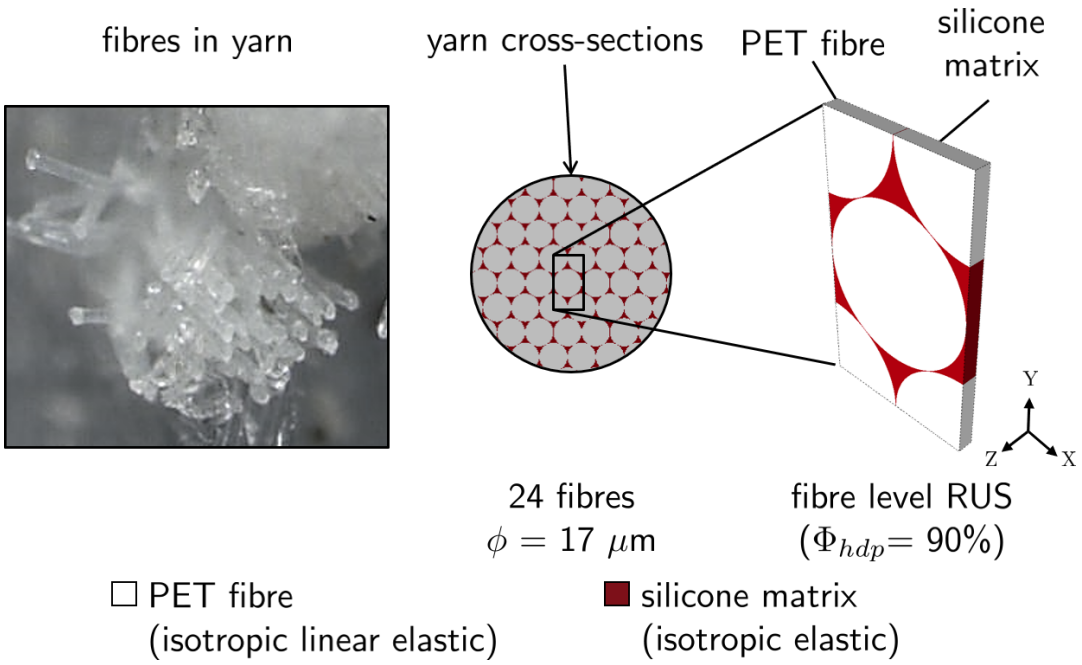

Figure 3.4: Fibre level structural model

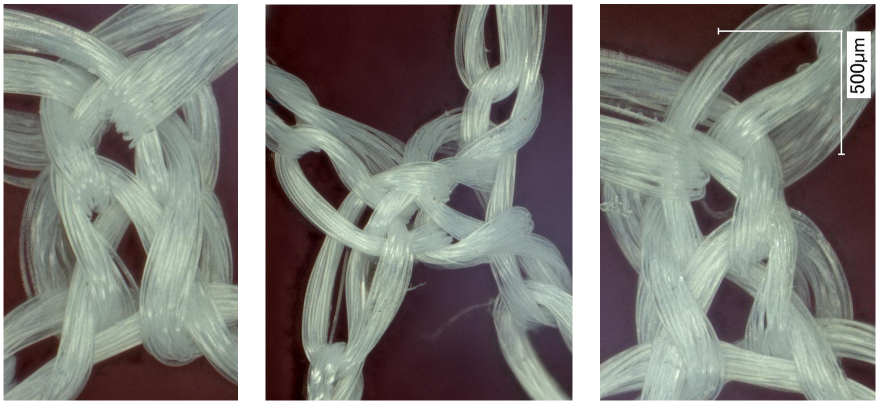

Figure 3.5: Different knit patterns in the textile

pattern, it is difficult to identify a consistent path along which the yarns are knit. Hence, it is necessary to simplify the knit for computationally efficient modelling. The simplified knit pattern has to account for the continuous load transfer within the yarns from one knit to another and also the locking of yarn alignment in loading direction due to the looping structure of the knit. Therefore, in this work the complex knits are approximated by a simplified knit pattern with a volume fraction of 19% as shown in Fig. 3.6. As the yarns are

modelled using transversely isotropic elasticity, proper material orientations are assigned to the yarns for which the material properties are obtained from the homogenized response at the fibre level. Matrix is modelled as an incompressible hyperelastic material. The homogenized material response from this level is then used to represent the textile structure in the textile level RUC. The mesh of the knit level structural model has 921635 C3D4 elements.

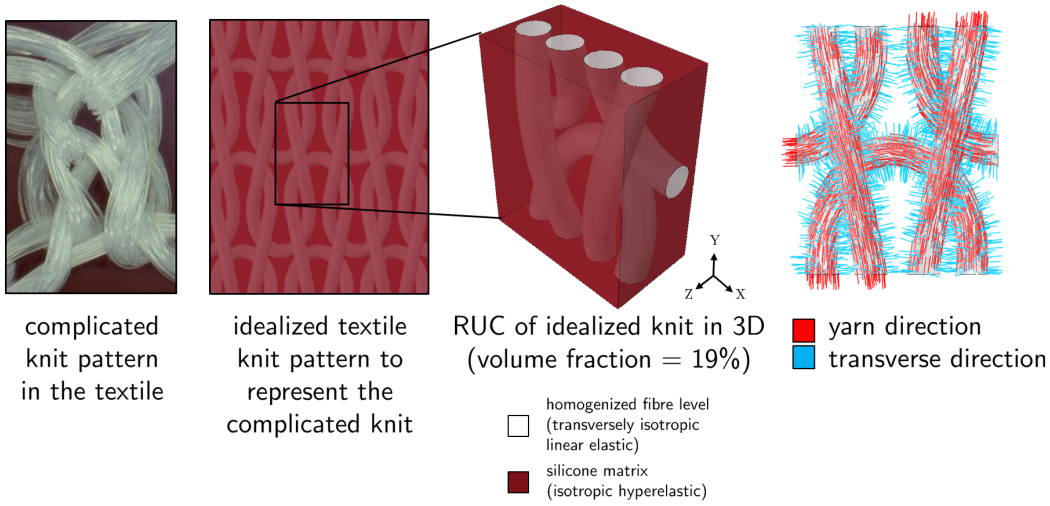

Figure 3.6: Knit structural model

3.4.4 Textile level structural model

Fig. 3.7 shows the textile pattern. Structurally, it represents a honeycomb pattern. The honeycomb pattern should provide the textile with equivalent in-plane stiffness. This is modelled using a RUC with an internal structure of volume fraction 36.67%, as shown in Fig. 3.7. On repeating the RUC in XY plane, one obtains a honeycomb pattern as shown. Orthotropic Fung's hyperelastic material model is used to represent the internal structure in the RUC, and the matrix is modelled as incompressible hyperelastic material. The homogenized knit level response is smeared over the internal structure using local directions as shown in Fig. 3.7. Homogenized material response from

this level is used to represent the centre layer in the heart valve model. The mesh of the textile level structural model has 192930 C3D8R elements.

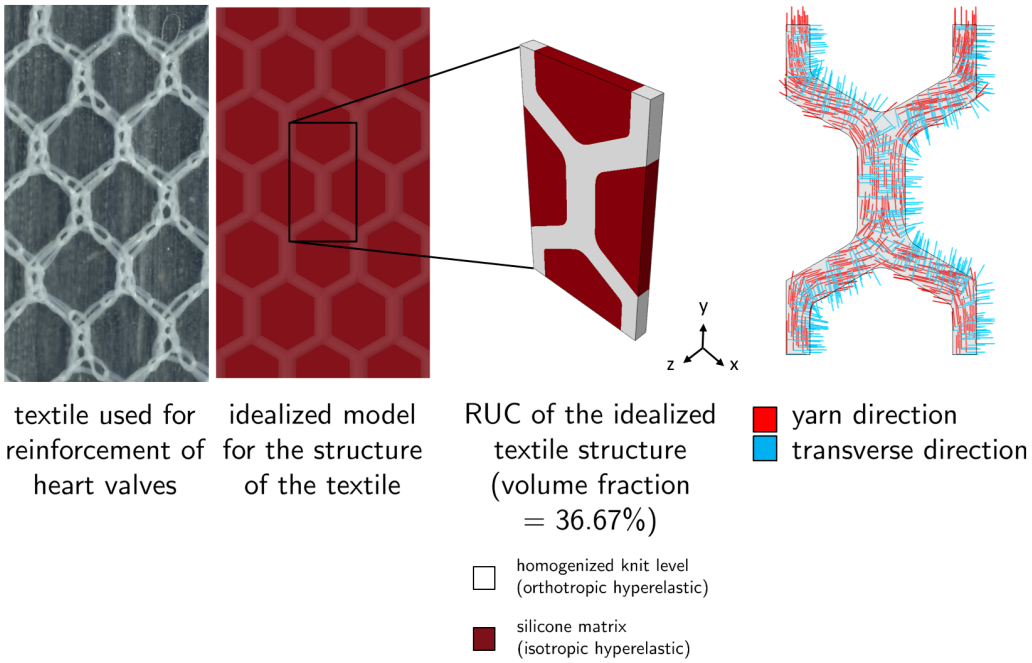

Figure 3.7: Textile level structural model

3.4.5 Macro level heart valve model

Fig. 3.8 shows the macro level heart valve model. The macro model of the heart valve is divided into three layers along the thickness. The centre layer is where the textile reinforcement is present. Only one element (i.e. single integration point over thickness) is used to represent the textile layer in the heart valve simulation. This layer is modelled by the orthotropic hyperelastic material model, with material parameters obtained by fitting the Fung's model to the virtual experiments conducted at the textile level model.

The outer and the inner layers are considered to be pure matrix (silicone or engineered tissue) layers and are modelled using the isotropic hyperelastic (Arruda Boyce) material model. The material properties for the matrix are ob-

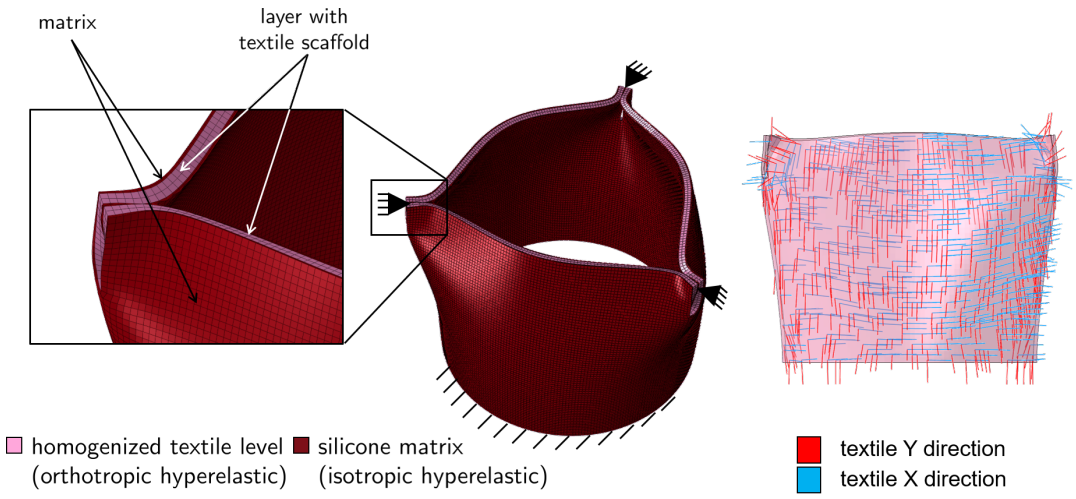

Figure 3.8: Macro scale heart valve level in its initial sutured configuration along with fixed boundary conditions

tained by fitting the Arruda Boyce model to the experimental results conducted on Elastosil samples. Considering the fibre/internal structure volume fraction across all the different layers, the overall volume fraction of the textile in the heart valve is 2.2%, whereas from the measurements, it is calculated that the TEHVs have a fibre volume fraction of $\approx$ 2.4%. The macro scale heart valve level is now subjected to the loading of three cardiac cycles and compared to experimental results. The macro model of the heart valve has 25317 C3D8R elements.

The simulations in the paper are based on the tubular valve construct as shown in Fig. 3.8 (see also Stapleton et al. [2015]). The diameter of the heart valve is 23 mm with a thickness of 0.7 mm and a height of 18 mm. Simulation is carried out on the initial tubular construct to achieve the geometry of the sutured heart valve. The deformed geometry is then extracted from the output file to obtain a stress free initial sutured configuration. Aortic and ventricular surface pressures are applied to simulate the cardiac cycle while keeping the suture points and the base of the heart valve fixed. Boundary conditions are summarized as in Fig. 3.8.

Parameters	Aortic pressure	Ventricular pressure
A_0	0.01322	0.006065
A_1	-0.0009058	0.001718
A_2	-0.0009038	-0.002571
A_3	-0.0005186	-0.00141
B_1	0.001583	0.007505
B_2	0.0002181	0.001291
B_3	-0.000355	0.001006
ω	7.712	7.701

Table 3.1: Parameters for periodic aortic and ventricular pressure loading of the heart valve

The experimental aortic and the ventricular pressure which are similar to the cardiac cycle (Fig. 3.9), are fitted by a Fourier expansion ($a = A_0 + \sum_{n=1}^{N}[A_n \cos n\omega(t - t_0) + B_n \sin n\omega(t - t_0)]$ for $t \geq t_0$) and applied as a periodic change in amplitude within Abaqus Hibbitt et al. [2001] as shown in Fig. 3.9. The parameters of the fit for ventricular and aortic pressures using $N = 3$ are given in Table 3.1.

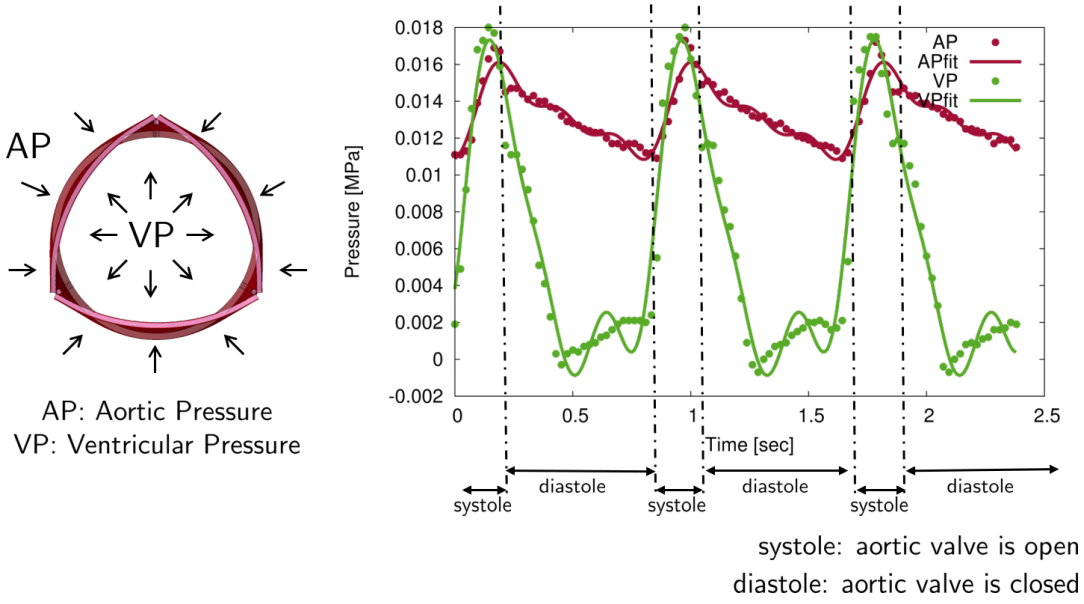

Figure 3.9: Experimental pressure and it's fit (AP: aortic pressure; VP: ventricular pressure). The fitted curve is used as hydrostatic loading for the finite element simulation of the macro-level heart valve

3.5 Material models

Four different material models are used across different levels. The fibres are modelled as linear-elastic and isotropic whereas an isotropic hyperelastic material model is applied for the matrix. The yarns are assumed to behave transversely isotropically as well as linear-elastically. To fit the response at the knit and the textile levels, Fung's orthotropic hyperelastic material model Fung et al. [1979] is used. Various other orthotropic/anisotropic hyperelastic material models such as the ones suggested by Holzapfel and Gasser [2001]; Reese [2003]; Holzapfel [2004]; Gasser et al. [2006]; Ehret and Itskov [2007] could also be used to represent orthotropic/anisotropic material response.

3.5.1 Transversly isotropic material model

The material properties of the yarn, used in the knit level RUC, are modelled using a transversely isotropic material law. Transverse isotropy is a special case of orthotropy, where the material has the same properties in one plane and different properties in the direction normal to this plane. These materials can be described by five independent elastic constants. By convention, the five elastic constants in transversely isotropic constitutive equations are the Young's modulus and Poisson's ratio in the symmetry plane, E_p and ν_p, the Young's modulus and Poisson's ratio in the normal direction, E_n and ν_{np}, and the shear modulus μ_{np}. Considering the out of plane direction to be the z-direction, the

compliance matrix takes the form

$$\begin{bmatrix} \epsilon_{\mathrm{xx}} \\ \epsilon_{\mathrm{yy}} \\ \epsilon_{\mathrm{zz}} \\ 2\epsilon_{\mathrm{yz}} \\ 2\epsilon_{\mathrm{zx}} \\ 2\epsilon_{\mathrm{xy}} \end{bmatrix} = \begin{bmatrix} \frac{1}{E_{\mathrm{p}}} & -\frac{\nu_{\mathrm{p}}}{E_{\mathrm{p}}} & -\frac{\nu_{\mathrm{np}}}{E_{\mathrm{n}}} & 0 & 0 & 0 \\ -\frac{\nu_{\mathrm{p}}}{E_{\mathrm{p}}} & \frac{1}{E_{\mathrm{p}}} & -\frac{\nu_{\mathrm{np}}}{E_{\mathrm{n}}} & 0 & 0 & 0 \\ -\frac{\nu_{\mathrm{pn}}}{E_{\mathrm{p}}} & -\frac{\nu_{\mathrm{pn}}}{E_{\mathrm{p}}} & \frac{1}{E_{\mathrm{n}}} & 0 & 0 & 0 \\ 0 & 0 & 0 & \frac{1}{\mu_{\mathrm{np}}} & 0 & 0 \\ 0 & 0 & 0 & 0 & \frac{1}{\mu_{\mathrm{np}}} & 0 \\ 0 & 0 & 0 & 0 & 0 & \frac{2(1+\nu_p)}{E_{\mathrm{p}}} \end{bmatrix} \begin{bmatrix} \sigma_{\mathrm{xx}} \\ \sigma_{\mathrm{yy}} \\ \sigma_{\mathrm{zz}} \\ \sigma_{\mathrm{yz}} \\ \sigma_{\mathrm{zx}} \\ \sigma_{\mathrm{xy}} \end{bmatrix} \tag{3.1}$$

where for symmetry the corresponding off diagonal terms should result into the same values.

3.5.2 Arruda Boyce material model

Elastosil silicone matrix material is modelled across all scales/levels (except the fibre level) using the Arruda Boyce model Arruda and Boyce [1993] which is an isotropic hyperelastic constitutive model used to describe the mechanical behaviour of rubber-like and other polymeric substances. This model is based on the statistical mechanics of a material with a cubic representative volume element containing eight chains along the diagonal directions. The material is assumed to be incompressible. The strain energy density function for the incompressible Arruda and Boyce [1993] model is given by

$$W = Nk_B\theta\sqrt{n}\left[\beta\lambda_{\mathrm{chain}} - \sqrt{n}\ln\left(\frac{\sinh\beta}{\beta}\right)\right] \tag{3.2}$$

where n is the number of chain segments, k_B is the Boltzmann's constant, θ is the temperature in Kelvin and N is the number of chains/density of chains in the network of cross-linked polymers.

$$\lambda_{\mathrm{chain}} = \sqrt{\frac{I_1}{3}}\ ;\ \ \beta = \mathcal{L}^{-1}\left(\frac{\lambda_{\mathrm{chain}}}{\sqrt{n}}\right)\ ;\ \ \mu_{ab} = Nk_B\theta \tag{3.3}$$

λ_{chain} represents the stretch of a chain. I_1 is the first invariant of the right Cauchy-Green deformation tensor, and $\mathcal{L}^{-1}(x)$ is the inverse Langevin function. μ_{ab} is the shear modulus obtained by fitting the experimental results.

3.5.3 Fung's orthotropic material model

The generalized Fung strain energy potential in Abaqus is based on the two-dimensional exponential form proposed by Fung et al. [1979], which was suitably generalized to arbitrary three-dimensional states using Humphrey [1994]. It has the form

$$W = \frac{c}{2}(e^Q - 1) + \frac{K}{2}\left(\frac{(J^2) - 1}{2} - \ln J\right) \tag{3.4}$$

with Q being defined by

$$Q = \mathbf{E} : \mathbb{B} : \mathbf{E} \tag{3.5}$$

$\mathbb{B}$ is a dimensionless symmetric fourth-order tensor of anisotropic material constants and $\mathbf{E}$ represents the Green-Lagrange strain tensor. The orthotropic form of the generalized Fung model with eleven independent variables is used in this work. The Voigt notation of the $\mathbb{B}$ matrix is given by

$$\hat{\mathbf{B}} = \begin{bmatrix} b_1 & b_7 & b_8 & 0 & 0 & 0 \\ b_7 & b_2 & b_9 & 0 & 0 & 0 \\ b_8 & b_9 & b_3 & 0 & 0 & 0 \\ 0 & 0 & 0 & b_4 & 0 & 0 \\ 0 & 0 & 0 & 0 & b_5 & 0 \\ 0 & 0 & 0 & 0 & 0 & b_6 \end{bmatrix} \tag{3.6}$$

It is well known in literature that parameter fitting of the Fung model largely depends on the choice of initial values. Hence, care has been taken to choose the initial values reasonably while fitting this model to the virtual experiments

at different levels.

3.6 Results and Discussions

3.6.1 Silicone matrix

The silicone matrix is characterized using tensile tests. The specimens had a gauge length of 31.28 mm, a width of 6.35 mm, and a nominal thickness of around 1.15 mm. The specimens were preloaded with 0.5 N, and stretched at 3 mm/min until failure. The engineering stress vs. stretch is plotted in Fig. 3.10. As can be seen from Fig. 3.10, silicone has a hyperelastic material response, which undergoes softening under cyclic loading representing the Mullins' effect. As the heart valve is subjected to cyclic fatigue loading, the silicone matrix is characterized only by the unloading curve of the last cycle. For the fibre level model, silicone matrix is characterized using linear elasticity (Fig. 3.11 (a)) where the elastic constant E is found to be 0.7323 MPa, and for all the other scales, the matrix is characterized by the Arruda Boyce model where the constants μ_{ab} and n are found to be 0.0862 MPa and 1.1762 respectively. Silicone is modelled as nearly incompressible.

3.6.2 PET fibres

The PET fibre material parameters were obtained by using experimental data from Lechat et al. [2011] as shown in Fig. 3.11 (b). This stress vs strain curve is from a tensile test on a single PET fibre. The curve appears to be linear initially (except for an initial non-linear period which is assumed by the authors to be remnants of the load transfer in the experimental set-up rather than actual material behaviour) until it became plastic. Since plasticity is not included in the present model, only linear elasticity is considered where the $E = 10.259$ GPa was found and $\nu = 0.35$ was assumed.

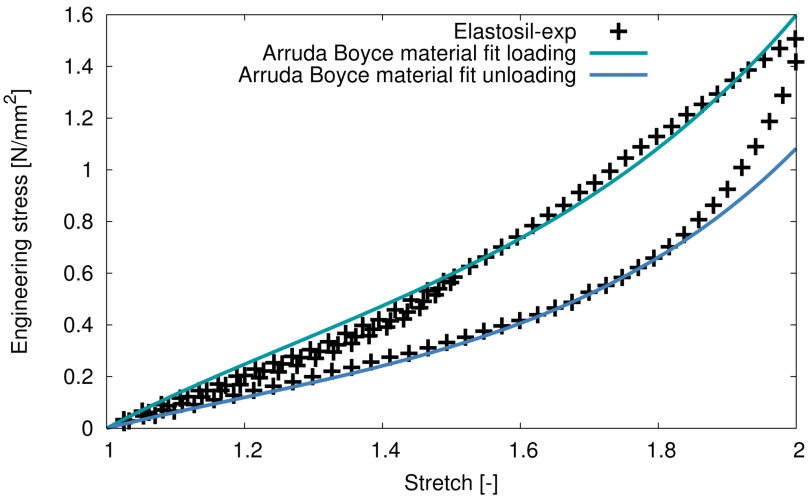

Figure 3.10: Experimental data used for non-linear material fit (using Arruda Boyce model) of the loading & unloading path for silicone

3.6.3 Fibre level structural model

The material response of the yarn (used as an internal structure in the knit level RUC) was derived from the homogenized response of the fibre level RUC. A far-field strain of 1% was applied to the RUC in three uni-axial strain and three shear deformation modes in order to fully populate the elasticity tensor (see Sodhani et al. [2015]). The material parameters, Young's modulus, shear modulus and the Poisson's ratio, were obtained from the compliance tensor (which is the inverse of stiffness tensor) as follows: $E_p = 346.43$, $E_n = 9233.01$, $\mu_{np} = 13.72$, $\mu_p = 122.33$ MPa, $\nu_p = 0.417$ and $\nu_{np} = 0.013$.

3.6.4 Knit level structural model

To characterize the material response of the knit level model, virtual tensile and pure shear tests were carried out at the knit level RUC for a far field strain of 25%. The material response was then fitted with the orthotropic hyperelastic Fung's model. The effective material response and the material fit are as shown in Fig. 3.13. c and K were found to be 1.008 and 4.163 MPa, respectively.

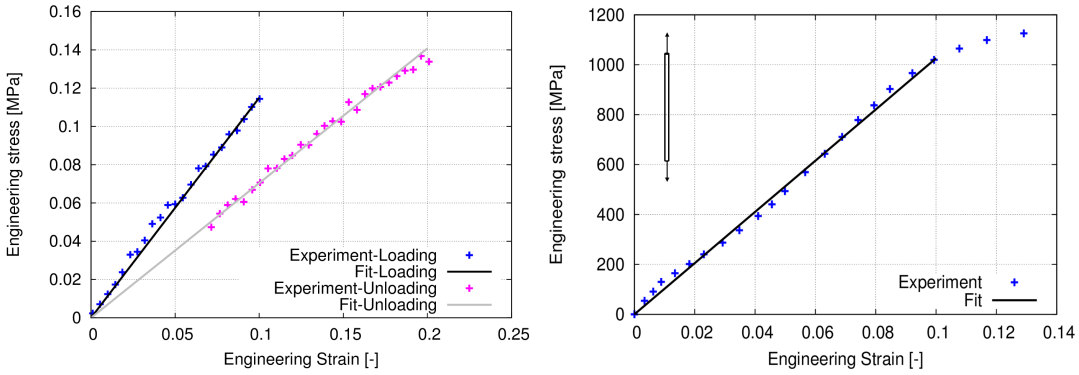

(a) (b)

Figure 3.11: Experimental data used for elastic fit of material models (a) silicone; (b) PET fibres Lechat et al. [2011]

Nine independent parameters constituting the $\hat{\mathbb{B}}$ matrix are given in Table 3.2.

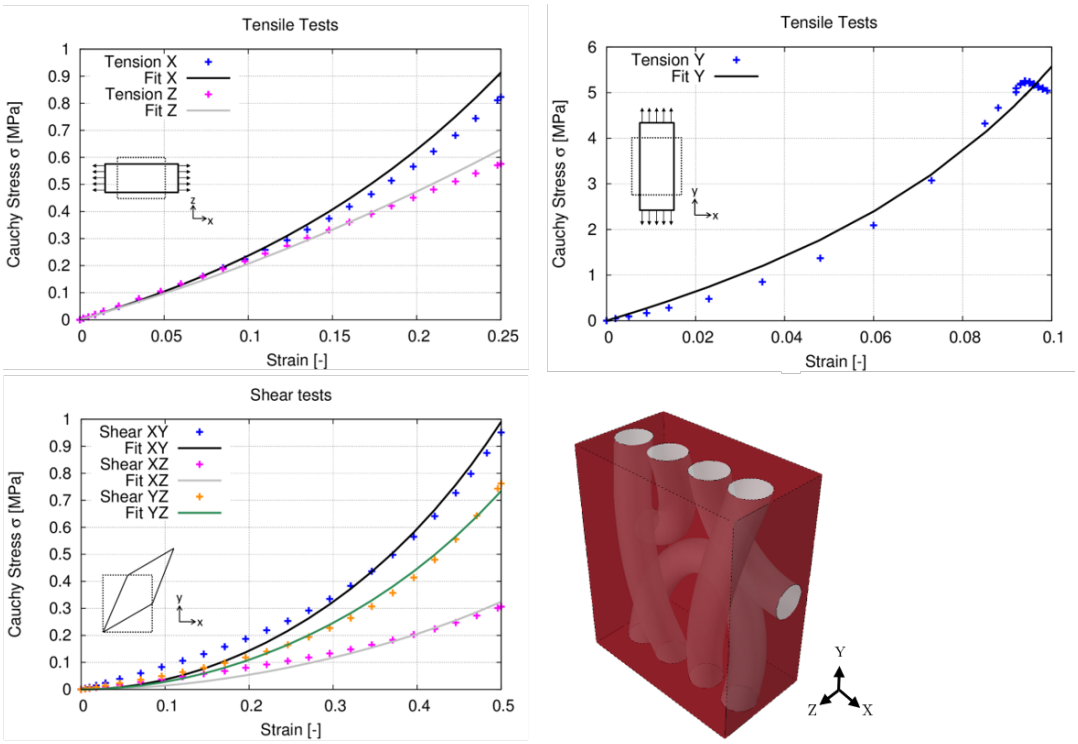

Figure 3.12

Figure 3.13: Results and fit from virtual tensile and shear experiments at the knit level

3.6.5 Textile level structural model

The material parameters obtained from the knit level model were then used to represent the internal structure in the textile level RUCs. Effective material response of the RUC was obtained by subjecting it to a far field tensile strain of 50% and pure shear strain of 25%. These were then fitted with the orthotropic hyperelastic Fung's model. As expected, one can observe that the RUC has comparable stiffness in X and Y directions, which is the effect of the honeycomb structure. A shear test was carried out only in the XY plane to obtain the b_4 parameter. Parameters b_5 and b_6 were assumed to be the same as b_4. The effective material response and the material fit are as shown in Fig. 3.14 where c and K were found to be 1.1635 and 2.000 MPa, respectively. Nine independent parameters constituting the $\hat{\mathbf{B}}$ matrix are given in Table 3.2.

Parameters	Knit level model	Textile level model
b_1	1.939	1.1957
b_2	33.412	1.2917
b_3	0.779	0.6059
b_4	14.649	12.5
b_5	6.039	12.5
b_6	11.409	12.5
b_7	2.591	0.0828
b_8	0.229	0.1396
b_9	1.319	0.1493

Table 3.2: Parameters of the $\mathbf{b}$ matrix for Fung material model for the knit level and the textile level model

3.6.6 Heart valve model

The parameters obtained from the textile level model were then used to represent the textile region, which is the centre layer in the heart valve model. As mentioned earlier, the inner and outer layers are considered to be pure matrix, which was represented by the Arruda Boyce material model. The material

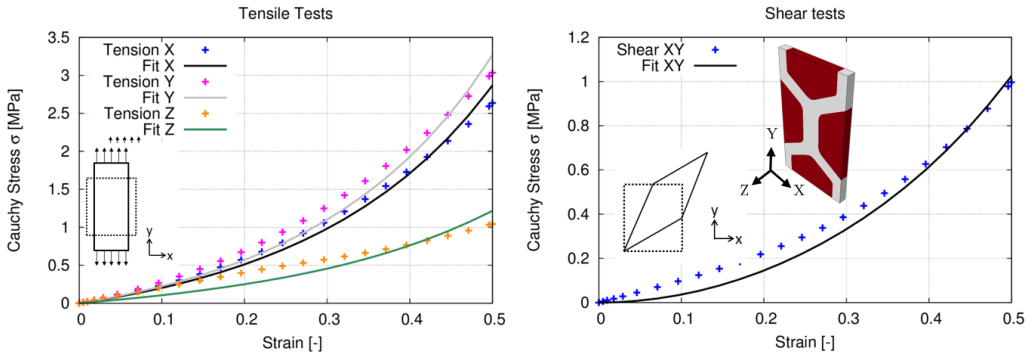

Figure 3.14: Results and fit from virtual experiments at the textile level

parameters were provided earlier. The deformed and undeformed configuration of the closed and open heart valve are shown in Fig. 3.15. It can be observed that during the opening phase of the cardiac cycle the heart valve opens more than its initial sutured configuration. Fifteen critical points on the loading cycle are pointed out and the logarithmic strain contour plots of the heart valve for these positions are shown in Fig. 3.16. From the contour plots, it is clear that in spite of having a symmetric geometry initially, the deformed geometry of the heart valve is not symmetric. In reality, this is due to the different bifurcation modes present for the folding of heart valve leaflets based on the position of the suture point in the corners, as explained by Stapleton et al. [2015]. In our simulations, results are not entirely symmetric because of the choice of the fixed nodes at the suture points. As the initial meshed structure (as shown in Fig. 3.8) is extracted from a simulation (explained in section 3.4.5), it is difficult to choose exactly the same corresponding nodal positions at each suture point. This creates a small perturbation of the symmetry. To evaluate the degree of un-symmetry, the principle logarithmic strains along three pre-selected paths, at the top, middle and bottom of the heart valve, have been plotted in Fig. 3.17. All the paths start at the vertical line crossing suture point “S1“, pass through the verticals along the suture points ”S2“ and ”S3“, before ending at its start point. Logarithmic strains are plotted over the normalized distance

of each path. Five different graphs for the second loading cycle, comparing the logarithmic strain at the mentioned critical points in the cardiac cycle for all the three paths, have been compared. It can be observed that when the valve is completely closed (point 6), there are large strains around the three suture points at the top (peaks), and in the centre at the bottom. The strains in the middle of the heart valve are relatively small in the centre but high under the suture region. During the systole phase (points 7 and 8) of the cardiac cycle, strains in all of the heart valve are relaxed, because during this phase the pressure difference between the aortic and the ventricular side of the heart valve is very small and the deformed heart valve is close to its undeformed configuration (see Fig. 3.15). In the initial diastole phase (point 9), the strains developed at the centre in the bottom are high compared to the other regions. This is because the bottom of the heart valve, which is fixed, is subjected to localised strain as the top part of the heart valve i.e. the leaflets move inward (bend) to close the valve. This is similar to a cantilever beam subjected to bending. The strains around the suture region are relatively small, as they are not subjected to large local deformation during this phase. The stain pattern in the middle layer is the same as described earlier. Maximum difference between the aortic and the ventricular pressure exist at this point. During the diastole phase when the aortic pressure decreases and the ventricular pressure increases (point 11), it can be observed that the fluctuation in the pressure difference leads to localised strains in the corners i.e. the suture region of the heart valve, because the pressure change is not sufficient to open the leaflets of the heart valve.

One can also observe some opening in the heart valve simulation during the diastole phase of the cardiac cycle. This is due to the use of only three elements over the thickness of the heart valve. To improve the closing response of the heart valve during the diastole phase, a higher number of integration points

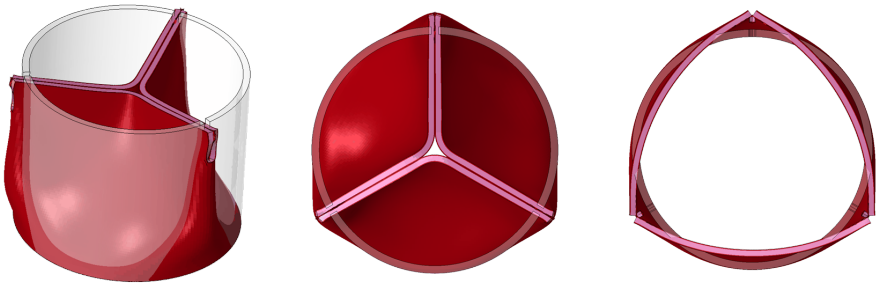

Figure 3.15: Deformed and undeformed configuration in the iso-geometric view and top view

over the thickness should be used.

The maximum principal logarithmic strain obtained in the heart valve is $\approx$ 0.55, which occurs at the constrained points in the heart valve, i.e. near the sutured region. This is equivalent to nominal strains of $\approx$ 70%. In most parts of the heart valve, the local maximum principal logarithmic strains are less than 0.4, which is equivalent to nominal strains of $\approx$ 50%. Therefore, the choice for the far field strain up to 50% at the textile level model is adequate to capture the effective response of the reinforcing textile at the macro level. Furthermore, the lower two levels are idealizations hence, it was assumed that the chosen far field stain limits are enough to predict the behaviour. Also, to be more precise one will need to account for local damage in the matrix due to higher far field strains. This is outside the scope of the present work.

To validate the results of the simulation with the experimental set-up, either a digital image correlation for the strain patterns in the artificial heart valve is needed or the fluid flow through the artificial aortic valve needs to be simulated to compare the flow volume. Both of the above mentioned validation approaches were outside the scope of this paper, which will be accounted for in future work. Hence, an image processing method to acquire the percentage of the open cross-section of the heart valve during the systole phase of the cardiac cycle to its initial cross-section was used to validate the modelling approach. Fig. 3.18 shows snapshots of the experimental heart valve over the cardiac

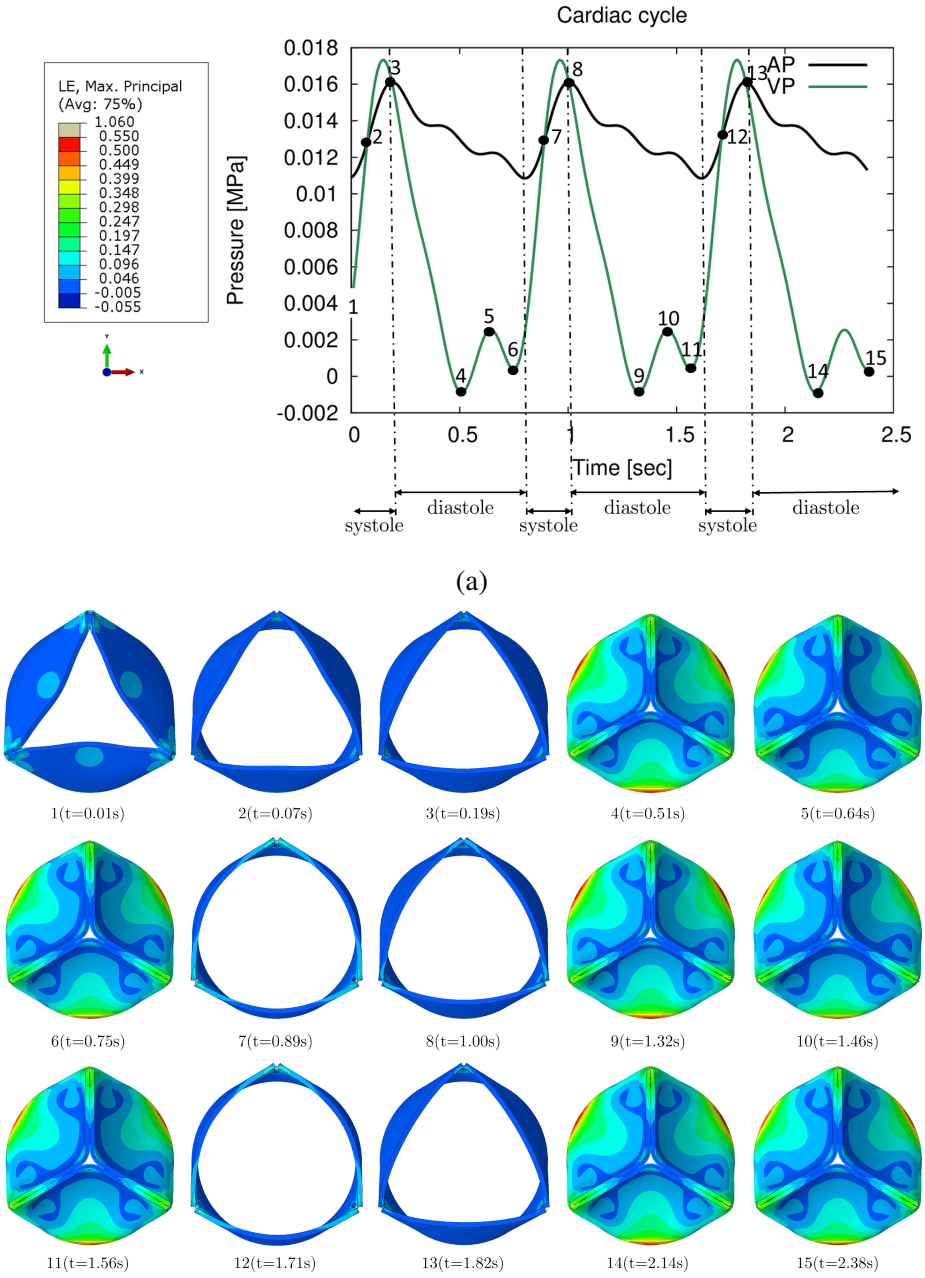

(a)

(b)

Figure 3.16: Initial configuration (a) loading curve along with the legend of the logarithmic strain plot (AP: aortic pressure; VP: ventricular pressure); (b) logarithmic strain contour plot

cycle in comparison with the snapshot of the simulation at the same time step. Comparison of this ratio is as shown in Fig. 3.18. From the comparison, it can

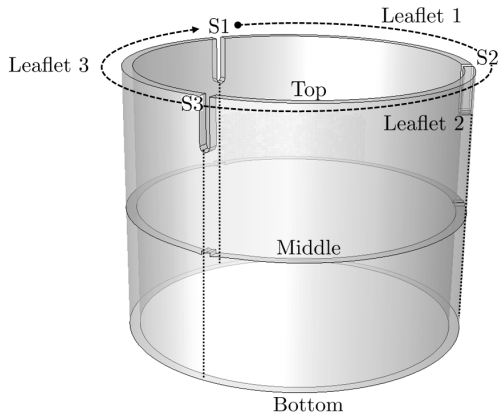

(a) Different paths

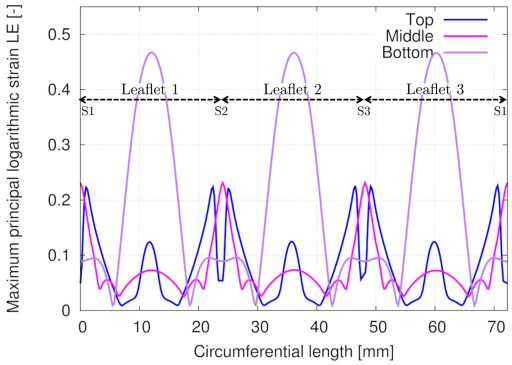

(b) at point 6

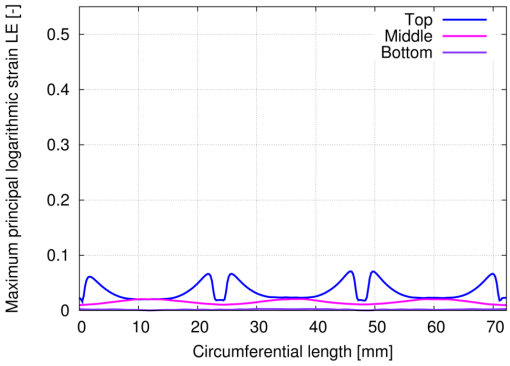

(c) at point 7

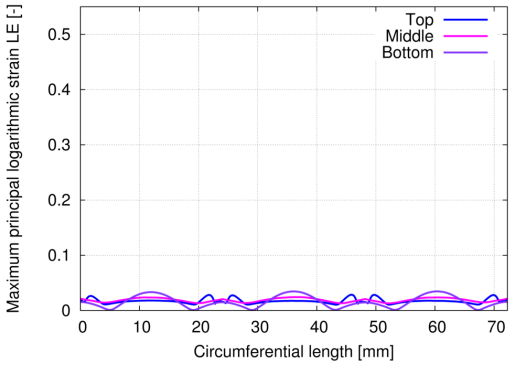

(d) at point 8

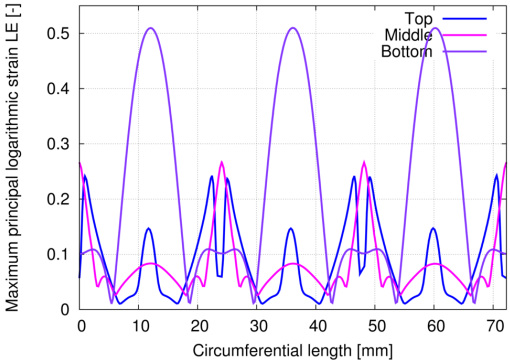

(e) at point 9

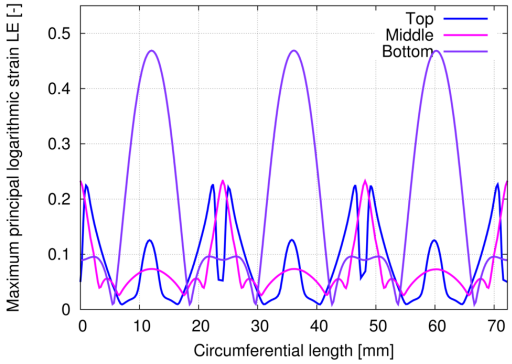

(f) at point 11

Figure 3.17: Logarithmic strains along different paths for the given time points

be observed that the percentage opening of the experiment and the simulation during the systole phase of the cardiac cycle are almost the same, whereas in the diastole phase, the simulated heart valve does not close completely due to the

reasons mentioned earlier. In the opinion of the authors, the current validation method, though not the most accurate, serves to validate the approach used to simulate the behaviour of the textile reinforced artificial heart valve.

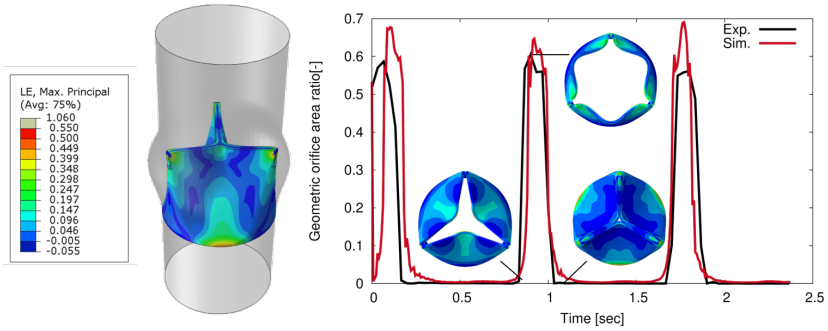

Figure 3.18: Experimental and simulation comparison of the open area ratios and their respective snapshots

3.7 Conclusion and Outlook

The goal of the current study was to show that competence of the multi-scale modelling approach to predict the behaviour of textile reinforced aortic heart valves, has been achieved. First, the complex structure of the heart valve was reduced to simplified structural models at different scales. Then, different relatively simple material models available in a commercial finite element tool were introduced. Repeating unit cells (RUCs) of these simplified structural models were then meshed to obtain a finite element (FE) model. These were then subjected to periodic boundary conditions and loaded using far field strain to obtain an effective material response. The effective material response was then fitted using the appropriate material models.

A macro FE model was constructed for the heart valve. The model was divided into three zones over the thickness. The outer layer was modelled as pure silicone matrix, whereas the material properties of the textile layer were derived from the hierarchical multi-scaling approach. Dynamic simulation of

the heart valve was carried out, where, in the first step the heart valve was sutured to avoid excessive distortion at one point. In the next step, ventricular and aortic pressures were applied on the inner and the outer surface of the heart valve. The obtained deformation pattern of the heart valve and percentage open area of the cross-section during systole and diastole phase of the cardiac cycle are in good agreement with the experimental results.

Further, the closing response of the heart valve needs to be improved, which can be achieved by mesh refinement over the thickness of the heart valve and a modified multi-scale modelling approach. Blood flow simulation using fluid-structure interaction also needs to be carried out to realistically simulate the cardiac cycle and analyse the flow volume through the valve. For more efficient modelling of the TEHV, a material model accounting for extra-cellular fibre (elastin and collagen) alignment within the matrix under cyclic loading during cultivation needs to be developed. To make the approach more reliable and robust further investigations are needed to quantify the deviation of the final result due to the change in volume fraction of individual structural levels, such that the modelling is faithful to the overall volume fraction of the heart valve. Also, further investigations are needed to determine the effect of different knit patterns in the knit level model on the overall results.

4 Article 3: Fluid-structure interaction simulation of artificial textile reinforced aortic heart valve: validation with an in-vitro test

This article was published as:

Sodhani D, Reese S, Aksenov A, Soğanci S, Jockenhövel S, Mela P, Stapleton SE. Fluid-structure interaction simulation of artificial textile reinforced aortic heart valve: Validation with an in-vitro test. Journal of biomechanics. 2018 Jul 20.

Disclosure of the individual authors' contributions to the article:

D. Sodhani conceptualized the multi-physics simulations, generated the required geometries, derived the necessary material properties and carried out the simulations; P. Mela conducted the in-vitro experiments, provided intellectual content and gave conceptual advice; A. Aksenov & S. Soğanci provided the support and licenses for using the FlowVision tool; S.E. Stapleton, S. Reese & S. Jockenhövel provided intellectual content and gave conceptual advice; S. Reese, P. Mela and S.E. Stapleton were engaged in obtaining funds for the research; All authors drafted the work for intellectual content; All authors approved the publication of the final manuscript.

4.1 Abstract

Prosthetic heart valves deployed in the left heart (aortic and mitral) are subjected to harsh hemodynamical conditions. Most of the tissue engineered heart valves have been developed for the low pressure pulmonary position because of the difficulties in fabricating a mechanically strong valve, able to withstand the systemic circulation. This necessitates the use of reinforcing scaffolds, resulting in a tissue-engineered textile reinforced tubular aortic heart valve. Therefore, to better design these implants, material behaviour of the composite, valve kinematics and its hemodynamical response need to be evaluated. Experimental assessment can be immensely time consuming and expensive, paving way for numerical studies. In this work, the material properties obtained using the previously proposed multi-scale numerical method for textile composites was evaluated for its accuracy. An in-silico immersed boundary (IB) fluid structure interaction (FSI) simulation emulating the in-vitro experiment was set-up to evaluate and compare the geometric orifice area and flow rate for one beat cycle. Results from the in-silico FSI simulation were found to be in good coherence with the in-vitro test during the systolic phase, while mean deviation of approximately 9% was observed during the diastolic phase of a beat cycle. Merits and demerits of the in-silico IB-FSI method for the presented case study has been discussed with the advantages outweighing the drawbacks, indicating the potential towards an effective use of this framework in the development and analysis of heart valves.

4.2 Introduction

Tissue engineered heart valves have been proposed as alternatives to the clinically adopted heart valves to overcome their limitations. Mechanical valves require life-long anticoagulation therapy because of the associated risk of throm-

bosis and thromboembolism, while the biological valves which are not as stiff, suffer from structural degeneration and therefore have a limited life. Different tissue engineering strategies have been proposed for the realization of valves which ultimately will consist of healthy tissues produced by the patient's own cells, putatively eliminating the above-mentioned limitations [Cheung et al. [2015]; Namiri et al. [2017]]. Hence, to achieve the mechanical properties in biological valves that would enable the correct functioning of the valve in the systemic circulation, the tissue has been reinforced with a textile for both surgical implantation [Weber et al. [2013]; Moreira et al. [2016]] and percutaneous delivery [Moreira et al. [2014a]]. The textile reinforcement must be carefully designed: too much reinforcement can cause the valve to be too stiff and lose functionality, while too little reinforcement can lead to early failure of the leaflets. To facilitate intentional and intelligent valve design, computational models of heart valves are required that form a link between reinforcement design and valve performance. The ability of a model to predict performance relies on the representation of two main aspects: the loading of the valve and the material properties of the constituents.

First, the loading of the blood flow on the leaflets needs to be represented. Several studies have been carried out to evaluate the influence of topological design and material response by simply considering the hydrostatic pressures acting on the structural domain [Koch et al. [2010]; Li and Sun [2010]; Sun et al. [2010]; Loerakker et al. [2013]; Saleeb et al. [2013]; Gunning et al. [2014]; Morganti et al. [2014, 2015]; Wang et al. [2015]; Sodhani et al. [2016]]. While these methods give a general idea of the performance of the valve, decoupled FE simulations often neglect the interaction of the fluid with the valve surface and its resulting loads.

Hence, FSI models are becoming increasingly important for biomedical engineering applications Luraghi et al. [2017]. A general review of FSI methods

was presented in Hou et al. [2012], while reviews on FEA, CFD and FSI simulation approaches for cardiac valves are found in Votta et al. [2013]. Experimental validation of FSI simulations have been reported in Wu et al. [2016]; Joda et al. [2016]. The number of studies considering FSI to evaluate the valve kinematics are increasing [see e.g. Borazjani and Sotiropoulos [2010]; Marom et al. [2012]; Griffith [2012]; Sturla et al. [2013]; Borazjani [2013]; Bavo et al. [2016]; Wu et al. [2016]; Joda et al. [2016]; Mao et al. [2016]; Luraghi et al. [2017]]. An important consideration for the FSI simulation is the definition of the fluid domain. Other than some exceptions [Shahriari et al. [2012]; Mao et al. [2016, 2017]; Toma et al. [2017]; Caballero et al. [2017]] that use smooth particle hydrodynamic simulations, most works use either a boundary conforming (ALE) or a non-boundary conforming (Eulerian) formulation.

In the ALE approach, two conforming (both structured and unstructured) meshes are used for the fluid and the structural domains. This approach was successfully applied to heart valves [e.g. Annerel et al. [2012]; Chandra et al. [2012]]. However, the inability of the ALE method to cope with large deformation problems restricts its application to the modelling of valves which undergo both large displacements and deformations.

In the immersed boundary (IB) Eulerian approach, introduced by Peskin [1972] for the heart valve, the fluid domain is discretized with a fixed grid where the Navier-Stokes (NS) equations are written in the Eulerian formulation and the structure is modelled with a Lagrangian mesh, free to move in the fluid domain [Bavo et al. [2016]]. This is more suitable for problems with large structural displacements/deformations [De Tullio et al. [2011]; Bavo et al. [2016]; Wu et al. [2016]; Joda et al. [2016]; Luraghi et al. [2017]]. As only the structural grid deforms within a stationary fluid grid, a lower computational cost is incurred. However, the IB method also has its share of disadvantages, such as a less accurate description of the fluid-structure interface. For example, a very

fine resolution of the IB grid would be required to accurately resolve the wall shear stresses at the interface which in turn is computationally very expensive. Various versions are being developed to address this [Griffith [2012]; Flamini et al. [2016]; Borazjani [2013]; Hsu et al. [2014, 2015]; Kamensky [2015]; Joda et al. [2016]].

The second aspect which needs consideration for the design of valves is the material representation. While several studies consider the valve to be a homogeneous elastic material [Koch et al. [2010]; Hsu et al. [2014]; Kamensky [2015]], others model the valve accounting for the collagen fibres in the native tissue valve using phenomenological material models. Such approaches do not facilitate design of the reinforcements. Hence, a multi-scale modelling approach for an artificial textile reinforced tubular aortic heart valve was developed Sodhani et al. [2016, 2018a]. In this approach, the fibre and matrix properties were utilized in lower-scale finite element models to find the homogenized material response based on the textile geometry. While the model was able to facilitate material design, the loading was only represented by a hydrostatic pressure.

Therefore, in the present work, FSI simulations using the IB method have been used to predict the kinematics of the textile reinforced tubular aortic heart valves along with its hemodynamic behaviour. Flow rate and the geometrical orifice area (GOA) ratio (i.e. ratio of open valve cross-section to its closed counterpart) obtained from the FSI simulations were compared to the in-vitro experimental results for validation. Apart from validating the simulation methodologies, these simulations also provide an insight into the flow dynamics and enable performance prediction and material design.

The paper is organized as follows. In Section 4.3 the artificial textile reinforced aortic valve (Section 4.3.1) together with the in-vitro experiment conducted (Section 4.3.2) on the valve is presented. The multi-scale mod-

elling approach used to determine the properties of the valve as well as the FSI procedure to evaluate the valve kinematics are detailed in Section 4.3.3 and Section 4.3.3, respectively. The results obtained from the computational study are compared to the in-vitro experimental results and effectiveness of the entire procedure as well as its advantages and disadvantages are discussed in Section 4.4. Concluding remarks and future perspectives are traced in Section 4.5.

4.3 Materials and Methods

4.3.1 The aortic heart valve

The textile reinforced aortic heart valves developed by Weber et al. [2013] and Moreira et al. [2014a] consist of a tubular tissue-engineered fibrin based construct using a single point attachment commissure technique [Goetz et al. [2002]]. These valves were produced by using fibrin gel as a cell carrier embedding vascular cells isolated from human umbilical cord veins and a tubular warp-knitted textile mesh as a reinforcing scaffold. Initially, the knitted polyethylene terephthalate (PET) mesh was embedded into the fibrin gel containing the cells. The tubular mesh construct was kept in the static cultivation for one week after which it was sutured into the stent. First, the construct was sewed at the three single commissure points and then circumferentially at the bottom to define the annulus (Fig. 4.1a). After this, the valve was dynamically conditioned for a fixed number of weeks in a custom-made bioreactor positioned in an incubator till it achieves enough strength to withstand the systemic circulation. This cultivated tissue-engineered *tex*textile reinforced tubular aortic heart *valve* (TexValve) was then subjected to an in-vitro test (explained below, see Fig. 4.1b).

Following the work of Röhrnbauer and Mazza [2013] and Röhrnbauer et al. [2014], it was assumed that a tubular valve with textile mesh embedded into

silicone (elastomer matrix) would result into the same qualitative conclusions when compared to the corresponding experiment on fully cultivated TexValve. Hence, in the previous work [Sodhani et al. [2016, 2018b]] as well as the present work, silicone matrix was assumed to represent the behaviour of cultivated tissues. Therefore, all the tests (including the in-vitro test of the valve) were carried out on a *si*licone embedded *tex*tile reinforced heart *valve* (siTexValve). siTexValve was prepared with the same radius and height of the TexValve with an exception of thickness. siTexValve was prepared with an uniform thickness across the valve, whereas depending on the combination of cultivation conditions and loading cycles, thickness of a fully cultivated TexValve can quantitatively differ in different parts of the valve. Kinematic response of a varying thickness valve can differ from that of a constant thickness valve. In principal, conducting this study on siTexValve enables us to validate the modelling approach with a relatively simple material and geometry, where, only the textile mesh was anisotropic in comparison with the TexValve, where, both the textile mesh and the tissue-matrix were anisotropic. It is important to note that although the silicone matrix was isotropic, the textile reinforced siTexValve was anisotropic in nature.

4.3.2 In-vitro test

In the in-vitro test, the siTexValve was tested under aortic flow and pressure conditions according to ISO 5840-3 i.e., cardiac output of 5 L/min, 100 mmHg mean aortic pressure and 70 bpm (beats per minute) frequency. The pressures were measured by pressure transducers (CODAN pvd Critical Care GmbH) positioned immediately upstream and downstream from the valve. Instantaneous flow was measured by a flow meter (sonoTT, em-tec GmbH) positioned immediately upstream from the valve. The test set-up is shown in Fig. 4.1b. Pressure and flow values were recorded by a LabVIEW^{TM} application (see Fig.

4.2a).

4.3.3 FSI model for the in-vitro test

In this work, the momentum balance equations for structure (in Lagrangian form) and fluid (in Eulerian form - Navier-stokes equation, see Appendix A) were solved using commercially available solvers. Both structure- and flow-solvers were employed in a co-simulation using the IB method to predict the flow rate across the siTexValve. The coherence of the predicted systolic flow rate and GOA ratio with the experimental measurements would imply that the predicted material behaviour closely matches the reality, along with the flow dynamics in the vicinity of the valve. An offset in the predicted flow rate would suggest divergence of the obtained material parameters and the flow dynamics from the real conditions. The FSI simulations were carried out using co-simulation with explicit finite element commercial solver Abaqus FEA and implicit computational fluid dynamics solver FlowVision (Capvidia NV, Leuven, Belgium), on an Intel Xeons linux cluster of 3.30 GHz with 16 processors.

As seen in Fig. 4.2b, the valve was modelled using the dimensions of the siTexValve measured directly on the sample. Starting with an initial tubular model, simulations were carried out to obtain the stitched state of the valve (for more details see Appendix B). After aligning the compartment and the stitched valve model, a tied-type constraint between the bottom of the valve and the compartment model was implemented arresting the sliding between model surfaces. The three dimensional valve geometry was created and meshed using Abaqus CAE and the compartment i.e., the flow domain was modelled using PTC Creo. As suggested in Katayama et al. [2008], the Sinus of Valsalva (see Fig. 4.2b) which reduces the abnormal stresses on the aortic valve and aids in its smooth closure, has also been modelled. The dimensions of the tubular

valve and the compartment have been reported in Table 4.1.

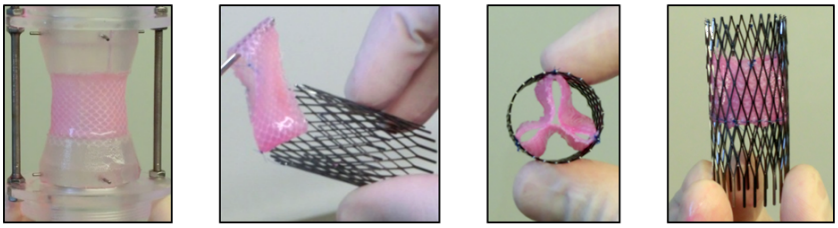

(a)

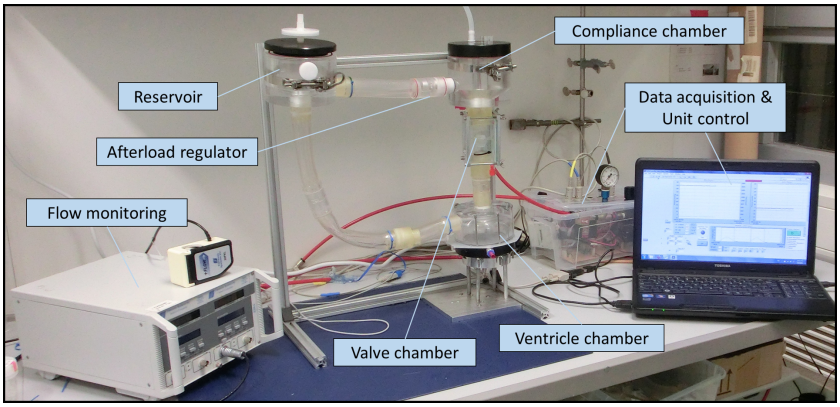

(b)

Figure 4.1: (a) Fabrication of the tube-in-stent valve. From left to right: tubular construct after one week of static cultivation; placement of the valve into a stent; suturing at the three commissure points forming three leaflets from a tubular structure; suturing the tubular construct circumferentially (annulus) [Moreira et al. [2014a]]; (b) in-vitro test set-up

One critical parameter of the simulation is the time step selection which is directly related to the smallest finite element or finite volume element for structure- and flow- solvers respectively. As the Nitinol stent (as seen in Fig. 4.1a) has very thin struts, very fine finite elements would have been required to accurately capture the structural behaviour of the stent. Similarly, very fine finite volume elements would have been required to resolve the flow around the stent even if it was included in the simulation as a rigid body. This would have resulted in exorbitant computational time. Hence, in the interest of keeping the computational costs at an acceptable level, the stent was not modelled in this study.

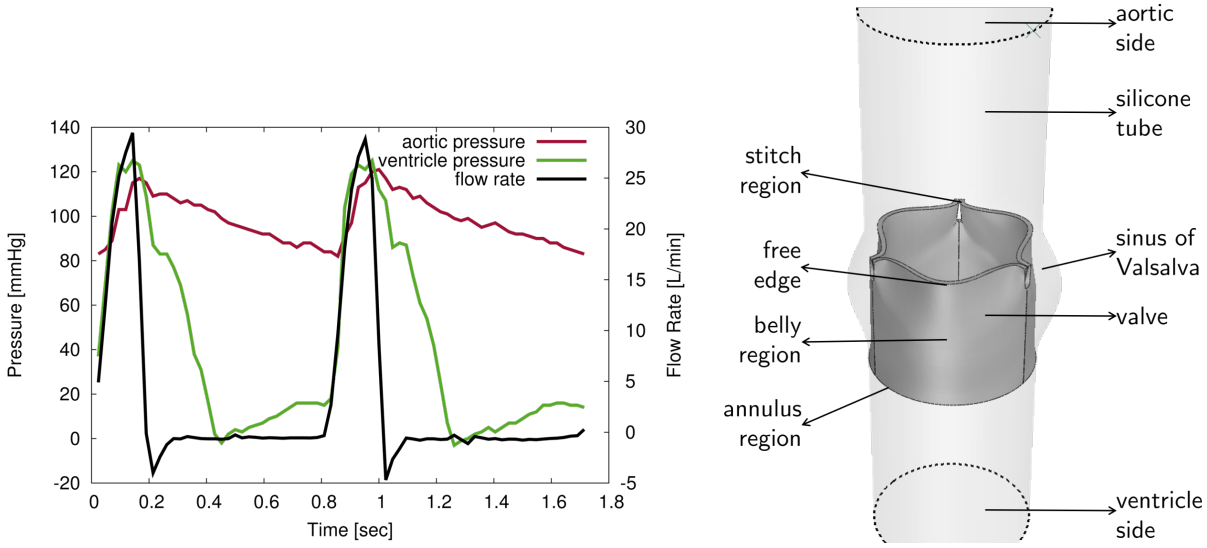

(a) (b)

Figure 4.2: (a) measured aortic and ventricular pressure downstream and upstream of the valve, respectively along with the flow rate; (b) in-silico FSI test set-up for fluid structure simulations

Table 4.1: Dimensions of the tubular valve and the compartment

Dimensions	Tubular valve $[mm]$	Compartment $[mm]$
Length	18	50
Diameter	23	23
Thickness	0.7	-
Sinus of Valsalva diameter	-	30

Material properties The liquid used for cultivations of tissues was a water based cell carrier. Considering that it has a Newtonian behaviour, properties of the liquid with density of 1000 kg/m^3 and a dynamic viscosity of 0.0008 $Pa.s$ (at 27 ^oC) were used. The valve was modelled as an orthotropic hyper-elastic material, parameters for which were obtained using multi-scale material modelling [Sodhani et al. [2018a]]. The silicon compartment model with the sinus of Valsalva was considered to be a rigid body forming the outer boundaries of the flow domain.

Structural multi-scale modelling Design and volume fraction of the textile in TexValve play a critical role in its functionality. Evaluating various textile designs and their volume fraction during the development of a TexValve can be very challenging, time-intensive and extremely costly. It can take several weeks to prepare specimens which are then required to be tested in a sterile environment for characterization before the cells in the samples degrade. Also, mechanical tests are often designed to create a macroscopically homogeneous field of strain over a certain measurement region of the specimen, providing little to no information about the microscopic behaviour of the reinforcement which affect the remodelling of collagen fibres in the sample. Heterogeneity of the deformations on smaller length scales which might increase with a decreasing scale of observation, define the macroscopic behaviour of the TexValve. This is where multi-scale modelling and computational homogenization can be used to characterize the smaller length scales, understand the deformation behaviour and optimize the scaffold structure.

Therefore, effectiveness of the method to derive the material properties for evaluating the kinematics of a valve is tested using a siTexValve. As aforementioned, decoupled FEM simulations have already been used to evaluate the siTexValve kinematics in Sodhani et al. [2016, 2018a] where the interaction of the fluid with the valve surface and its resulting loads were neglected.

Material properties of the siTexValve were determined using a methodology referred to as "hierarchical multi-scaling" in the literature (see Bednarcyk et al. [2015]). This means that an incremental deformation gradient was applied on a structural unit cell model as kinematic boundary conditions. The model was solved according to minimum energy principles and the stresses homogenized over the volume (or reaction forces obtained averaged over the respective boundaries) led to the incremental stress tensor, producing a virtual experimental stress vs. stretch (or strain) curve. This was then used to fit

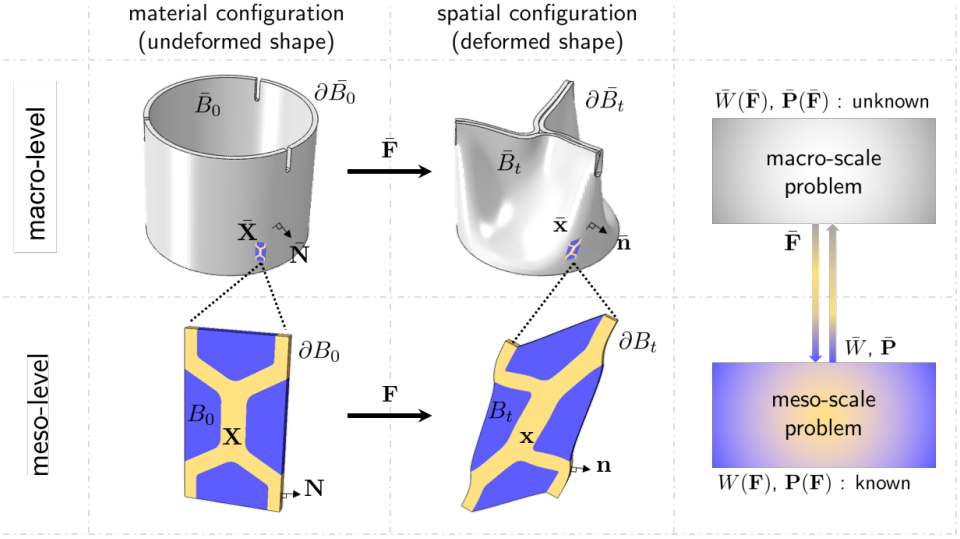

(a)

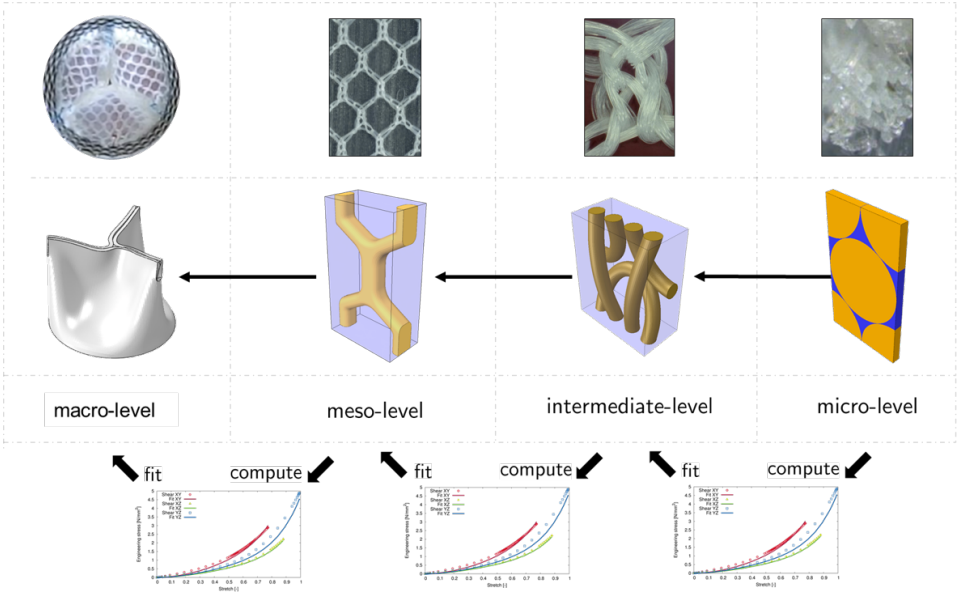

(b)

Figure 4.3: (a) Schematic representation of the multi-scale method Sodhani et al. [2018b]; (b) division of the valve into four structural levels to predict the material parameters of the siTexValve

an appropriate material model to determine the parameters for an upper level model. Fig. 4.3a shows a schematic representation of the method.

The approach is restricted to strain-driven computational homogenization. The central idea of this technique is to prescribe the deformation gradient $\bar{\mathbf{F}}$,

of the macro-scale (upper-level) onto the structure of the micro-scale (lower-level) and to compute the effective response of the micro-scale, in particular the macro-scale Piola stress $\bar{\mathbf{P}}$ (engineering stress). The micro-scale (lower-level) quantities are related to their macro-scale (upper-level) counterparts through volume averaging over the repeating unit cell (RUC). The volume averaging over a domain B_0 with a volume V_0 bounded by the external boundary ∂B_0 is defined as

$$[(\bullet)] = \frac{1}{V_0}\int_{B_0} (\bullet)\, dV \;\text{ with }\; V_0 = \int_{B_0} dV \tag{4.1}$$

In the context of material and geometrical non-linearity, the equivalence of strain energy on the micro- and meso-scale is given by the Hill-Mandel condition Saeb et al. [2016], where $\bar{\mathbf{P}} : \delta\bar{\mathbf{F}} - \langle \mathbf{P} : \delta\mathbf{F} \rangle \overset{!}{=} 0$. The use of periodic displacement-based boundary conditions is a well established technique to fulfil the Hill-Mandel condition and obtain the effective properties/response of a material from its lower level structure, particularly in the context of first-order strain driven homogenization presently used (for example see Bednarcyk et al. [2015]; Sodhani et al. [2015]). As mentioned earlier, to obtain the effective property at the macro-scale (upper-level), only the micro-stress over B_0 needs to be integrated. To circumvent the computationally expensive volume integral of the micro-stresses, the surface integral in the reference configuration was evaluated as follows:

$$\bar{\mathbf{P}} = \frac{1}{V_0}\int_{B_0} \mathbf{T} \otimes \mathbf{X}\partial B_0 \tag{4.2}$$

where traction $\mathbf{T} = \frac{d\mathbf{f}}{dA}$, i.e., the ratio in force $d\mathbf{f}$ acting on the infinitesimal area dA. For large deformations, this results in the engineering stress i.e. the first Piola Kirchoff stress $\bar{\mathbf{P}}$. The macroscopic deformation $\bar{\mathbf{F}}$ is either given or can also be derived using the prescribed far-field displacements. Using these

Table 4.2: Parameters of the Fung material model for the textile layer in the valve model

c (MPa)	K (MPa)	b_1	b_2	b_3	b_4	b_5	b_6	b_7	b_8	b_9
1.1635	2.000	1.1957	1.2917	0.6059	12.5	12.5	12.5	0.0828	0.1396	0.1493

two quantities, further continuum quantities can also be derived. For a detailed understanding of the method please refer Saeb et al. [2016].

The same procedure was repeated until all the scales under investigation were accounted for, finally obtaining the parameters of the heart valve which was modelled using Fung's orthotropic hyperelastic material model. The parameters obtained for the textile layer in the valve are reported in Table 4.2. The outer silicone layer was modelled using Arruda-Boyce [Arruda and Boyce [1993]] hyperelastic material model, parameters for which can be found in Sodhani et al. [2016]. The work flow for multi-scale modelling of the heart valve is summarized in Fig. 4.3b. siTexValve valve was divided into four structural levels with the effective fibre volume fraction of 4.47%.

Meshing of structural and fluid domains The valve model was discretized by 98700 8-node reduced-integration hexahedral elements i.e., C3D8R in Abaqus, and was simulated using the Lagrangian approach. Fluid loads during the co-simulation result in large rotations/bending of the valve walls. Therefore, the fluid solver must continuously track the valve boundaries to resolve the fluid flow and maintain the no-slip boundary condition along the moving valve walls. Curvilinear boundaries of the valve were hence introduced in the computational fluid domain by a set of plane facets (surface mesh). To accurately capture the motion while preserving the curvilinear boundaries of the valve, FlowVision uses the finite-volume approach along with a fully automatized mesh generator based on the Sub-Grid Geometry Resolution (SGGR) method [Aksenov et al. [1996, 1998]] to solve the governing fluid dynamics equations.

SGGR is an advanced analogy of the well-known cut-cell approach. In this

method, an initial Cartesian grid with local adaptation was introduced in the computational domain. Plane facets from the external surfaces of the finite element mesh (of the valve) were used as a boundary for the fluid domain. These facets are formed by a set of external faces $B_{s_{ij}}$ of the finite element mesh (see Fig. 4.4a), where i is the facet number of element j. Motion of these plane facets were accounted for using the Euler approach where, the valve surface was moving along the stationary mesh. Movement of the valve surface creates complex polyhedron cells where, the facets of the valve surface would "cut" the unconformable rectangular fluid cells overlapping it. These complex polyhedron cells contain the information about the corresponding finite element surface mesh. The shape S_m (see eq. 4.3) of one such polyhedron can be expressed as a sum of cell faces E_{lm} (where l is the facet number) and part of the facet i of the j^{th} element cut by the fluid cell.

$$S_m = \sum_{l=1,L} E_{lm} + \sum_{j=1,J} \sum_{i=1,I} dF_{ijm} \tag{4.3}$$

where, L is the number of existing fluid cell faces, I is the number of planar facets from a single finite element and J is the number of finite elements in one fluid cell. All geometrical information necessary for approximation of governing equations were determined, like, volume of the new cell, squares of its boundaries, distances from boundaries to a mass-centre of the cell and its neighbours. All the governing equations were approximated on the basis of the applied grid. In order to account for the geometric changes imposed by the moving walls (directly affecting the fluid flow characteristics), the cell volumes were allowed to change. Solving the fluid dynamic equations on such cells provide a direct data transfer mechanism without any intermediate interpolation. This is a special case for immersed boundary method. For example, the pressure of fluid p_{ij} on face $B_{s_{ij}}$ is found by integrating pressure

over all fluid cells (M) containing this face, given by,

$$p_{ij} = \frac{1}{A(B_{s_{ij}})} \sum_{m=1,M} p_m A(dF_{ijm}) \tag{4.4}$$

where, $A(B_s)$ is the area of face B_s and $A(dF_{ijm})$ is the area of the facets in the cell m. This information can then easily be exchanged between the finite element and fluid solvers.

The grid was refined (adapted) based on two conditions: (1) the fine structures of the valve surface, and (2) high gradients of the fluid flow velocity, in order to achieve the sufficient accuracy of the numerical simulations. The initial grid was an ordinary structured grid. Each cell of the grid can be subdivided (when adaptation occurs) into eight cells of a higher level grid which can be further subdivided. During the simulation, the conditions for the mesh refinement need not be satisfied in some parts of the flow domain. In such cases, the reverse process of making the mesh coarser was applied: where, the previously refined cells were joined together to form a bigger cell. In this way, a fully dynamic mesh adaptation was achieved. Dynamic mesh adaptation can be used for improved computation time with reasonable accuracy as it refines the flow domain around the stationary as well as moving bodies, provided, the starting grid accurately captured the flow dynamics within the bulk of the flow domain.

The initial number of cells in X, Y and Z directions are 22, 78, and 22, respectively. The bounding planes on either side of the fluid domain act as the inlet and the outlet boundaries. The volume adaptation with level 2 (see Fig. 4.4b) and cell division of 8 was used near the valve surface and a volume merge as explained earlier was used in the computational domain. This leads to a fine flow grid around the valve at all times and a coarse flow grid in the flow domain away from the valve, as shown in Fig. 4.4c. As the deformation of the valve was time dependent, the fluid grid was reconstructed dynamically in real-time. Therefore, the total number of cells in the fluid domain was dynamic and in

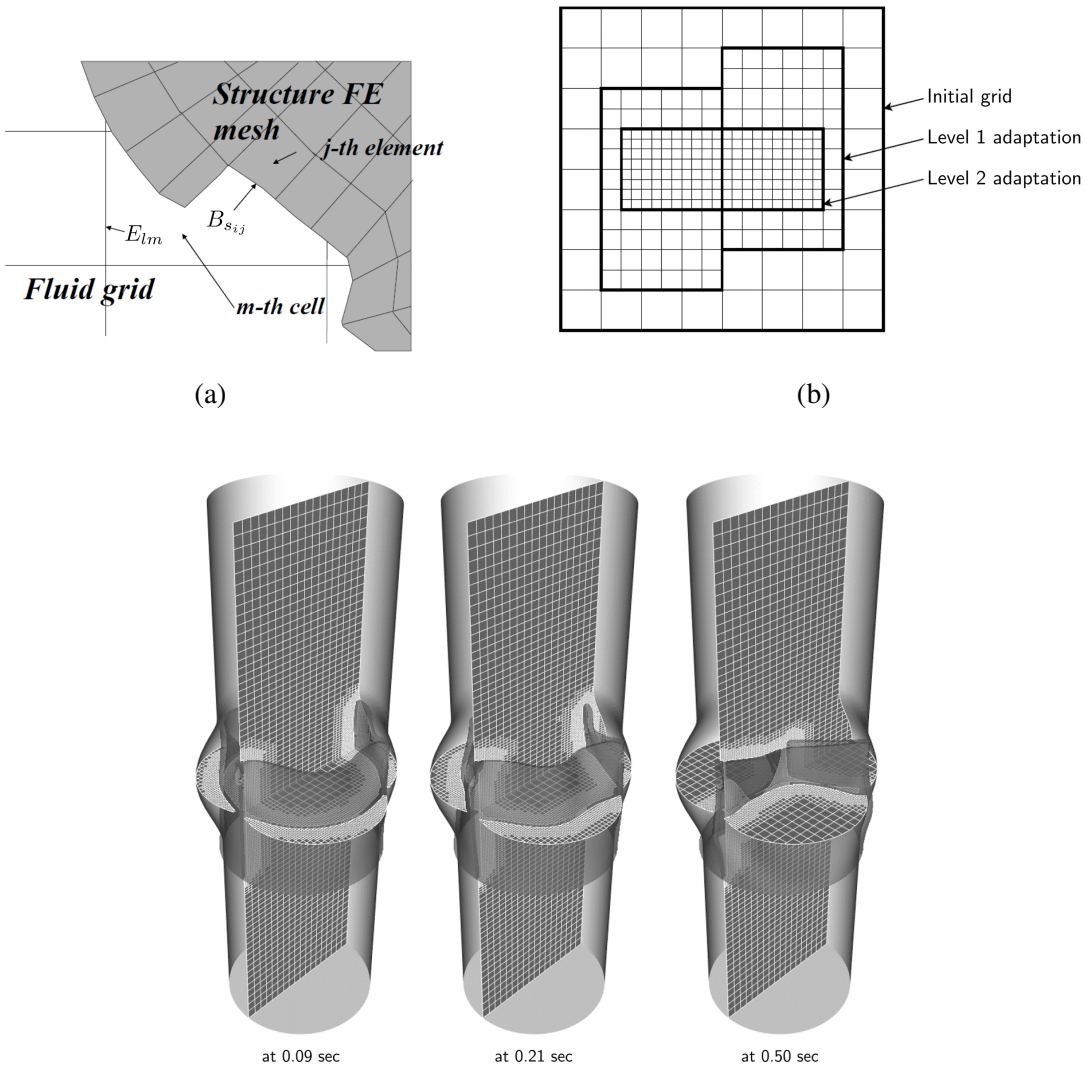

(a) (b)

(c)

Figure 4.4: (a) Cutting of fluid domain by finite element [Aksenov et al. [1998]]; (b) an adaptively refined hierarchical Cartesian grid comprised of two nested levels shown in 2D; (c) fluid domain mesh adaptation around the valve

this particular case ranged between 280,000-300,000 cells.

Boundary conditions As a boundary condition for the structural part, the bottom and the stitched regions of the valve were fixed in all directions. For the fluid part, the transvalvular pressure was applied to the inlet and a zero pressure condition was applied to the outlet (see Fig. 4.2b). Transvalvular pressure

is the difference between the upstream (ventricle) and downstream (aortic) pressures, measured in the in-vitro test. The fluid domain was fixed in space using a reference point. Two cycles, 0.86s each (according to 70 bpm of in-vitro test), were simulated to ensure a stable response of the simulation. The applied transvalvular gradient and the corresponding pressures have been reported in Fig. 4.5b. Apart from the pressure boundary conditions for simulating flow dynamics and structural deformations, no slip boundary conditions were specified on the fluid-structure interface. Pressure p_{ij} and velocity v_{ij} were transferred between the solvers using eq. 4.4 and eq. 4.5, respectively.

$$v_{ij} = \sum_{n=1,N} w_{nij} \dot{u}_{nij} \tag{4.5}$$

where, N is the number of nodes on the element face B_{sij}, w_{nij} is the weight coefficient for calculating face velocity depending on the face geometry.

Contact modelling Management of solid-solid contact directly in Abaqus during the co-simulation plays a critical role in the outcome of the simulation. In literature, it is often observed that minimum threshold distance between the leaflets was imposed, to preserve a gap during the diastole. This introduces unwanted artificial leakage which is reduced by modifying the permeability of the cell located in the area during the coaptation time. But, use of the FlowVision solver enables the complete closure of the valve. To enable this, the single geometry of the tubular valve was divided into three leaflet geometries. These were then tied together at the cutting plane. Contact between the pair of leaflets was modelled using a penalty based general-contact algorithm (an interaction option in Abaqus) with contact surfaces defined on the ventricular side of the leaflets. Contact was also defined on the aortic side of the valve together with the inner-surface of the compartment (specifically the sinus of Valsalva region) using a general contact algorithm.

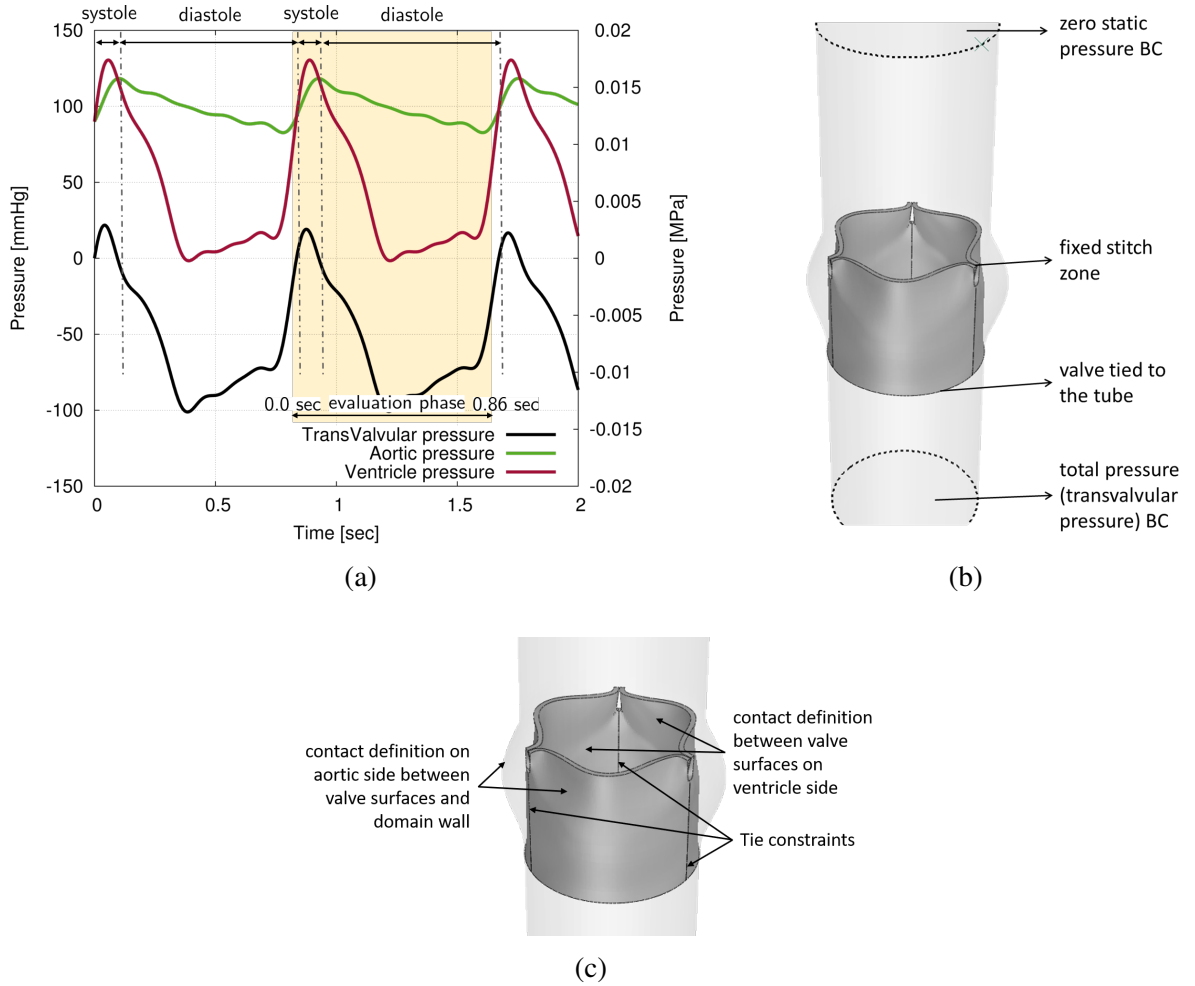

Figure 4.5: (a) The pressure wave forms obtained by fitting a three term Fourier series equation to the experimental curve shown in Fig. 4.2a. The fitted values are reported in Sodhani et al. [2016]; (b) boundary conditions applied on the valve and the flow domain in the FSI simulation; (c) tie and contact definition

Setup of co-simulation The employed simulation method uses a two-way coupling procedure. Information exchange between Abaqus and FlowVision was performed at time steps Δt defined by the user. The time step $\Delta t = t_{n+1} - t_n$ is the so-called FSI time step. This consists of several Abaqus and FlowVision time increments.

The FSI coupling includes the following steps:

- For the structural part (superscript s), eq. 4.13 was solved by Abaqus

to obtain displacements of the nodes, $\mathbf{u}_{n+1}$ corresponding to time t_{n+1}. Fluid pressure p_n was obtained from the previous time step t_n and was assumed constant during the time step Δt.

- Displacement of the nodes, $\mathbf{u}_{n+1}$ was transferred to FlowVision; Velocity of the deformed surface $\mathbf{v}^s$ was calculated.
- Navier-Stokes equation (eq. 4.16) along with interface boundary conditions (eq. 4.17) were solved by FlowVision to obtain fluid loading on the structure.
- Pressure p_{n+1} was transferred to Abaqus at the end of all FlowVision time increments at t_{n+1}.

Decoupled FE simulation The results obtained from the FSI simulation were also compared to decoupled finite element simulations. The boundary and contact conditions for these simulations are identical to those of the coupled FSI simulations. Hydrostatic transvalvular pressure as shown in Fig. 4.5b was applied as an uniform surface pressure on the ventricular surface of the valve. For a detailed description of simulation setup and results analysis please refer to Sodhani et al. [2018a, 2016].

Wall Shear Stress analysis FSI simulations also enable us to compute hemodynamic risk indexes based on the Wall Shear Stress (WSS). WSS is represented by the time varying local signal $S = S(\mathbf{x}, t)$, exerted by the fluid flow on the valve walls. Leaflet wall-shear stress was computed for both sides of one leaflet (aortic and ventricular) similar to the study of Chandra et al. [2012]. The shear stress exerted by the fluid on the arterial wall, $S(\mathbf{x}, t)$, is defined as the tangential component of the traction vector τ_f, $S(\mathbf{x}, t) = \tau_f.\mathbf{t}_f$, where τ_f is the tangent unit vector to the fluid domain in the current configuration and pointing in the mean direction of the fluid.

The two most common risk indicators related to the concept of the hemodynamic shear stress and adopted in the clinical practice, are the time-averaged magnitude of the wall shear stress, (S_a), and the oscillatory shear index, OSI, respectively. OSI characterizes the oscillatory nature or the directionality of the wall-shear stress (OSI = 0: purely unidirectional/pulsatile flow; OSI = 0.5: purely bi-directional/oscillatory flow) whereas S_a represents the average magnitude of the wall-shear stress over one cardiac cycle. The pulsatility and magnitude of the leaflet wall-shear stress was characterized over one cardiac period (T) of 0.86s. OSI and S_a are defined as follows,

$$\text{OSI} = \frac{1}{2}\left[1 - \left(\left|\int_0^T S(t)dt\right| \Big/ \int_0^T |S(t)|dt\right)\right] \tag{4.6}$$

$$S_a = \frac{1}{T}\int_0^T |S(t)|dt \tag{4.7}$$

As it can be observed, OSI and S_a are insensitive to the magnitude and direction of the shear stress, respectively. Therefore, alternative indexes, have been proposed in the recent literature, trying to extend the predictive power of OSI, e.g. the residency time (proportional to $\mu_f/T(1-2.OSI)Sa$) [Himburg et al. [2004]] or TBD_N and $TBD_{\Delta T}$ detailed in Bianchi et al. [2017]; Nestola et al. [2015] based on the three-band decomposition (TBD) approach proposed by Gizzi et al. [2011]. The TBD analysis divides the generic time-varying signal of WSS ($S = S(\mathbf{x}, t)$) into a set of three functions via a control running threshold, $\hat{S}$.

$$S^+(\mathbf{x}, t) = \begin{cases} S(\mathbf{x}, t), & \text{for } S(\mathbf{x}, t) \geq \hat{S} \\ 0, & \text{for } S(\mathbf{x}, t) < \hat{S} \end{cases} \tag{4.8}$$

$$S^0(\mathbf{x},t) = \begin{cases} S(\mathbf{x},t), & \text{for } -\hat{S} < S(\mathbf{x},t) < \hat{S} \\ 0, & \text{for } S(\mathbf{x},t) \leq \hat{S} \text{ and } S(\mathbf{x},t) \geq \hat{S} \end{cases} \tag{4.9}$$

$$S^-(\mathbf{x},t) = \begin{cases} S(\mathbf{x},t), & \text{for } S(\mathbf{x},t) \leq -\hat{S} \\ 0, & \text{for } S(\mathbf{x},t) > -\hat{S} \end{cases} \tag{4.10}$$

The closed time support of function $S^+(\mathbf{x},t)$ is made up by N^+ time intervals, where N^+ denotes the numerosity, and is computed as the number of time intervals where $S(\mathbf{x},t) \geq \hat{S}$. The union of these N^+ time intervals gives the total time duration T^+ when $S^+ \neq 0$. Similarly, N^0 and T^0 (resp., N^- and T^-) are the numerosity and the total duration associated to $S^0 \neq 0$ (resp., $S^- \neq 0$).

Two synthetic risk predictors (TBD_N and $TBD_{\Delta T}$) based on time intervals $T^{+,0,-}(\hat{S})$ and numerosity $N^{+,0,-}(\hat{S})$ are defined to condense the vast information contained in the dynamic evolution of the WSS signal. Values of these risk predictors are calculate by considering k equispaced values of $\hat{S}_k$ for the threshold in range [0,max($S(\mathbf{x},t)$)] over the interval [0,T]. TBD_N and $TBD_{\Delta T}$ are defined as

$$TBD_N(\mathbf{x}) = \frac{\sum_{k=0}^{K} \hat{S}_k N^-(\hat{S}_k)}{\sum_{k=0}^{K} \hat{S}_k [N^+(\hat{S}_k) + N^0(\hat{S}_k) + N^-(\hat{S}_k)]} \tag{4.11}$$

$$TBD_{\Delta T}(\mathbf{x}) = \frac{\sum_{k=0}^{K} \hat{S}_k T^-(\hat{S}_k)}{\sum_{k=0}^{K} \hat{S}_k [T^+(\hat{S}_k) + T^0(\hat{S}_k) + T^-(\hat{S}_k)]} \tag{4.12}$$

The N^- values derived by WSS signals are typical signatures of the recirculation zones, when compared to the contributions given by N^+ and N^0, due to the unidirectional net flows. Moreover, the threshold $\hat{S}$ in the definitions allows to account also for the magnitude of the shear stress. High values of these indicators are related to the presence of low and retrograde WSS signals and thus linked with the possible deposition and growth of the thrombus. For a

detailed understanding of this method, the readers are referred to Bianchi et al. [2017]; Nestola et al. [2015]; Gizzi et al. [2011].

4.4 Results and Discussions

FSI simulations provide a range of results for both fluid and structural analysis. Simulation results between the time range of 0.80s to 1.66s were chosen to illustrate and compare one "close-open-close" cycle (Fig. 4.5b) with the in-vitro tests. The presented results were normalized for one beat cycle of 0.86s.

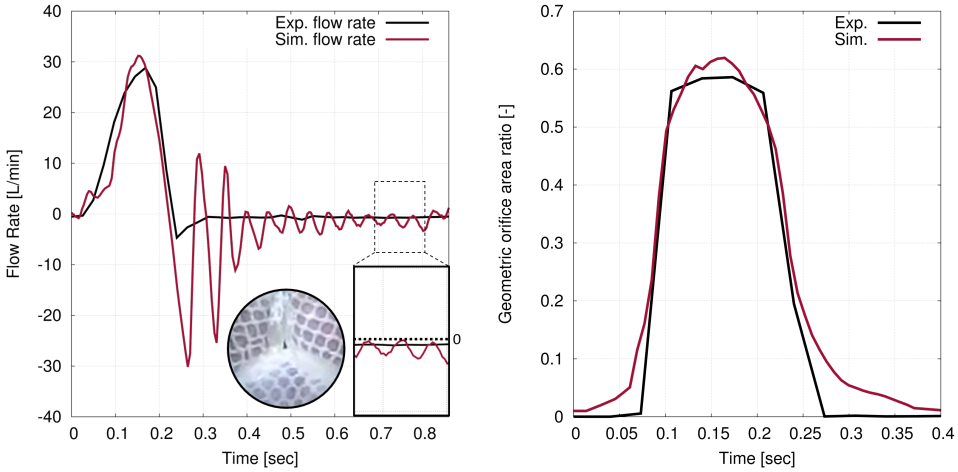

(a) (b)

Figure 4.6: (a) Comparison of the flow rate between in-vitro and the FSI simulation results; insert: close up view of the siTexValve showing a gap at its geometric centre, resulting in a continuous back flow which is corroborated by a negative flow rate recorded in the experiments during the diastolic phase; (b) geometric orifice area ratio obtained by FSI simulations are in good agreement with the in-vitro results during the systolic phase of a beat

A comparison of the flow rate and the GOA ratio, from the in-vitro test and the FSI simulation are plotted in Fig. 4.6a and Fig. 4.6b, respectively. From the graphs one can observe that the simulation results are in good agreement with the experiments during systole but show some discrepancy between the in-silico and in-vitro flow rate waveform during diastole. However, the

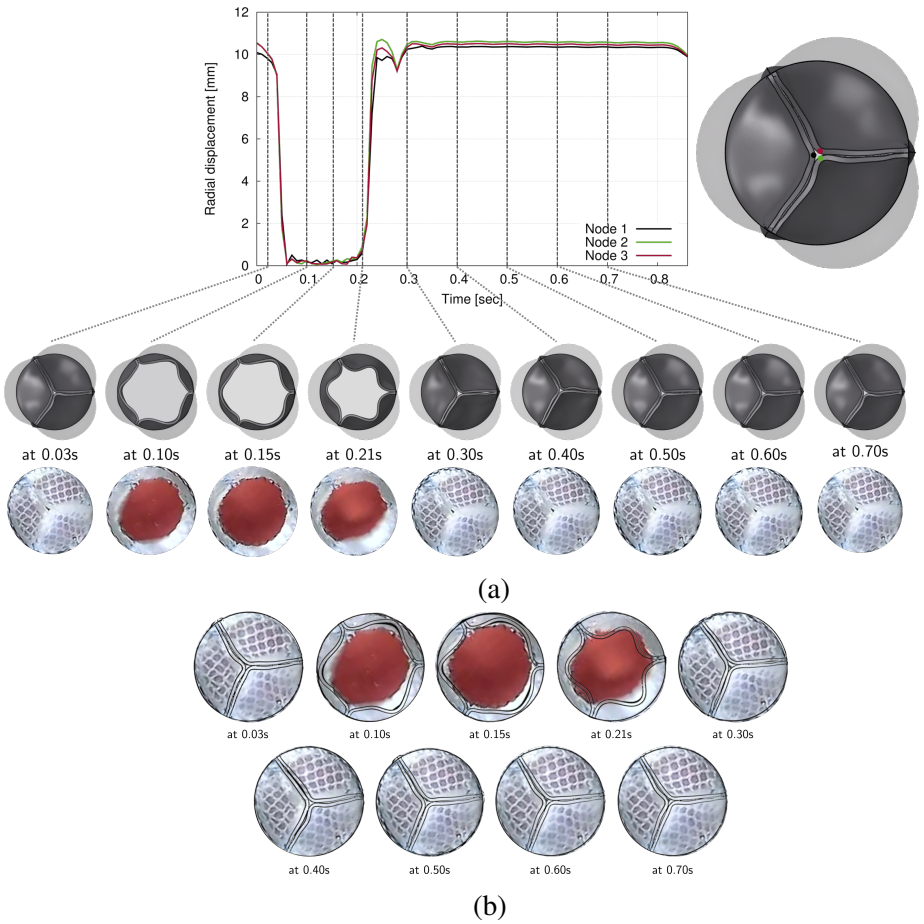

Figure 4.7: (a) radial displacement of three points on centre of the free edges of the tubular valve leaflets has been plotted over one beat cycle and comparison of the valve deformation state at nine different time points in a normalized beat cycle has been presented; (b) overlay of simulated valve deformation on in-vitro valve movement.

simulation results overestimates the peak systolic flow rate and the GOA ratio by 10.3% and 5.03%, respectively. Tubular siTexValve kinematics have also been reported for the entire cycle in Fig. 4.7a, where it can be noted that the open and close kinematics of the valve in the FSI simulation is in good qualitative sync with the experimental results. From the valve kinematics, it can be observed that although the free edges of the valve almost achieve a complete closure during the diastolic phase, there remains a tiny opening in the centre. This incomplete closure of the valve in the simulation results into artificial

valvular leakage (flow from the aortic to the ventricular side), leading to valve reverberations. The small opening further causes localized high pressures (see pressure distribution in Fig. 4.8 at 0.5s & 0.7s) and high velocity zones (see velocity distribution in Fig. 4.8 at 0.5s & 0.7s), resulting into the oscillations observed in the diastolic phase of the flow rate (Fig. 4.6a).

The incomplete closure of the valve is the limitation of valve geometry/design and its meshing. In literature, valves are either modelled using shell elements or solid elements. Often when the valve is modelled using solid finite elements only half a leaflet (or one sixth of a tri-leaflet valve) is modelled with a symmetric boundary condition on both flow and structural domains (e.g. see Joda et al. [2016]; Loerakker et al. [2013]). This introduces a sharp edge and a corner point at the centre of the free edge of the valve leaflet facilitating the complete closure of the valve which is then represented by mirroring the leaflet across the symmetry plane. When the entire valve (i.e. all the three leaflets) is modelled, it can be observed in the work of several authors (e.g. see Hsu et al. [2014]; Kamensky [2015]; Sun et al. [2010]) that the valve does not close completely in the geometric centre leading to a geometric central leakage area. In principle, the leaflets of the valve are dominated by a bending type deformation whereby it would be possible to achieve a better closing behaviour at the centre by refining the mesh but it is not possible using finite elements (even with a very fine mesh) to achieve a complete closure of the valve at it's geometric centre. Hence, contrary to reality often an artificial kink is introduced in the geometry at the centre of the free edge to achieve compete closure of the valve (e.g. see Marom et al. [2012]) or the permeability of the fluid cell in the leakage region is modified during the diastole to prevent leakage (e.g. see Bavo et al. [2016]). But, if observed closely (see Fig. 4.6a), even the siTexValve does not close completely and there is also a constant leakage from the valve used in the in-vitro test as seen in Fig. 4.6a. These simulation strategies were not

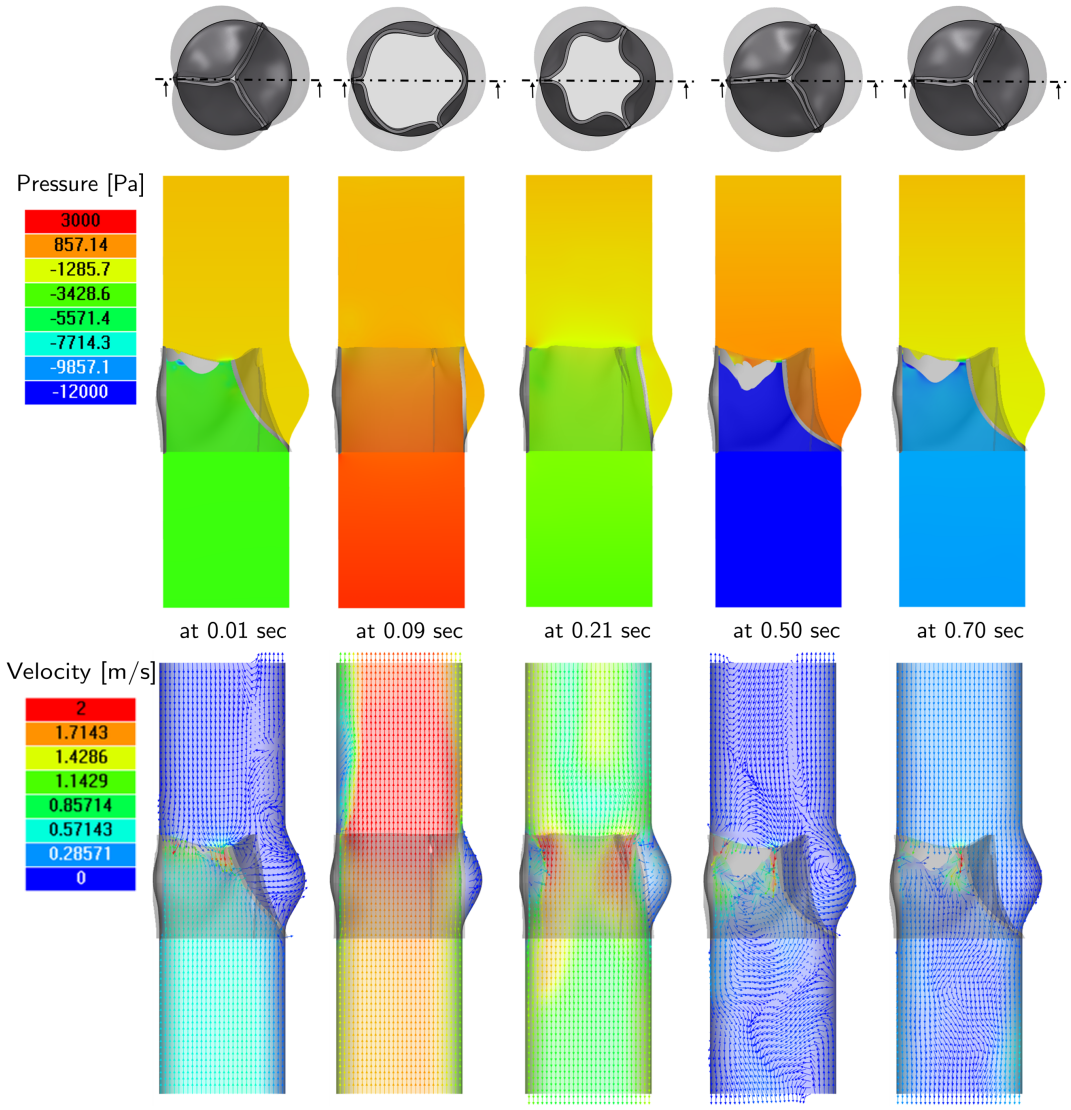

Figure 4.8: Pressure and velocity distribution on a plane passing through the geometric central leakage area are reported. As expected, the absolute pressure build up on the ventricle side of the valve can be clearly observed during the diastolic phase. Velocity vector plots also show the build-up of vortices in the sinus of Valsalva (e.g. at 0.50 sec). These vortices assist in the closing of the valve during the diastolic phase. Changes in pressure at the geometric central leakage area leads to valve reverberations and inversely the reverberations of the valve lead to localized pressure changes. This results into the leakage area behaving like an exit of a nozzle with respect to the flow direction where localized low pressure relative to its surroundings develop, resulting into high velocity back flows (e.g. at 0.50 & 0.70 sec).

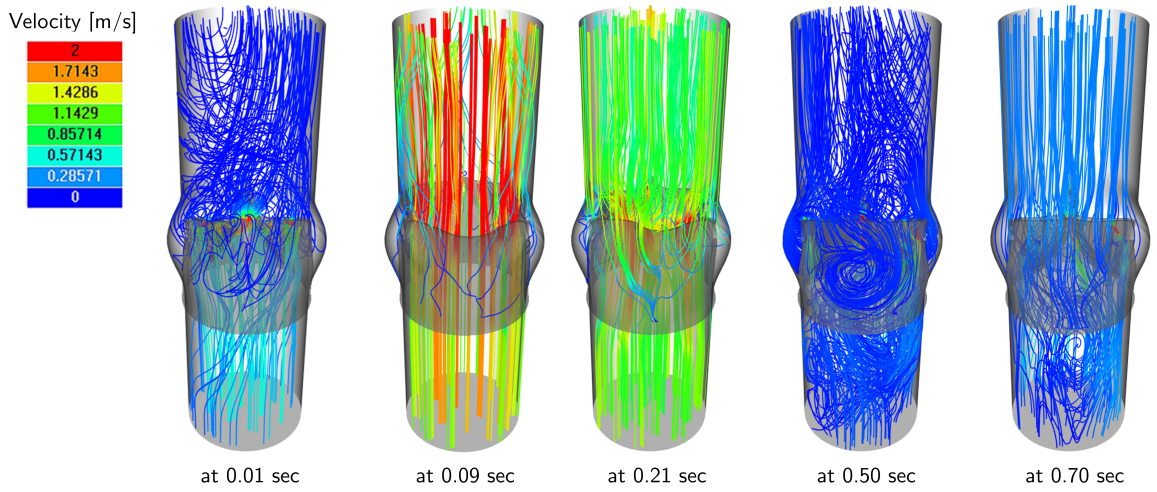

Figure 4.9: 3D streamlines with contours of velocity distribution show the flow pattern (turbulence, laminar & vortices) in the fluid domain at different time points in one beat cycle.

employed in this study while modelling the valve only with five elements over thickness to conserve the computational costs. This results in a physiologically acceptable leakage in the simulation from the geometric central leakage area. The leakage could be reduced/avoided by introducing a small asymmetry in the leaflets of the tubular valve (or in tri-leaflet valve) as suggested in Sun et al. [2010]. A small example of such a computation is presented in Appendix C, which is a part of our on-going study and has not been included in the current work in detail due to the length constraints of the paper.

In the FSI simulation the silicone compartment is assumed to be rigid in contrast to the in-vitro experiment. This is because the results of these FSI simulations are compared to the decoupled FEM simulations Sodhani et al. [2016], where the loads on the compliant silicone compartment are not considered. But, the presence on an elastic compartment would result in a more compliant system as it would dissipate the total energy in the system resulting in reduced valve reverberations in turn reducing the valve leakage (e.g. see Hsu et al. [2014]; Flamini et al. [2016]; Marom et al. [2012]). Maximum

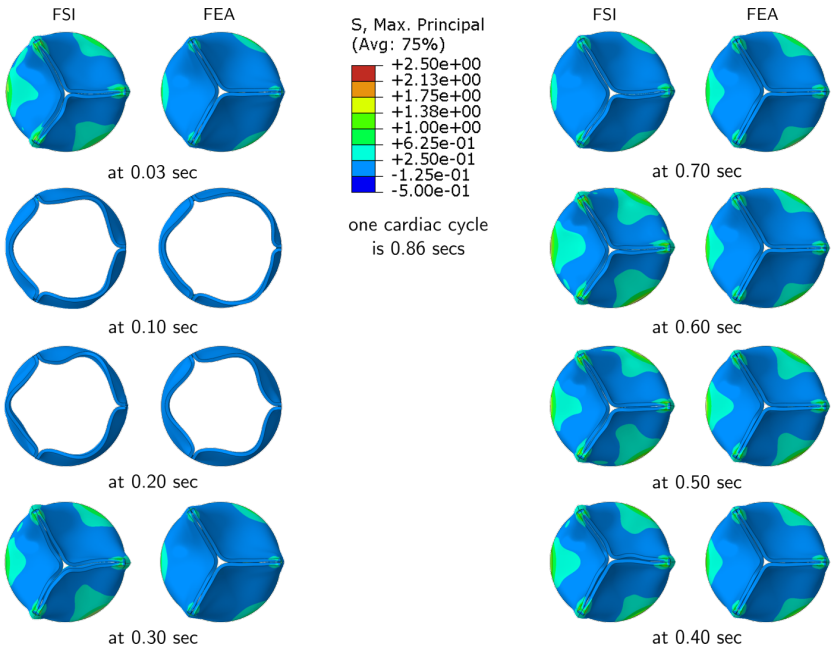

(a)

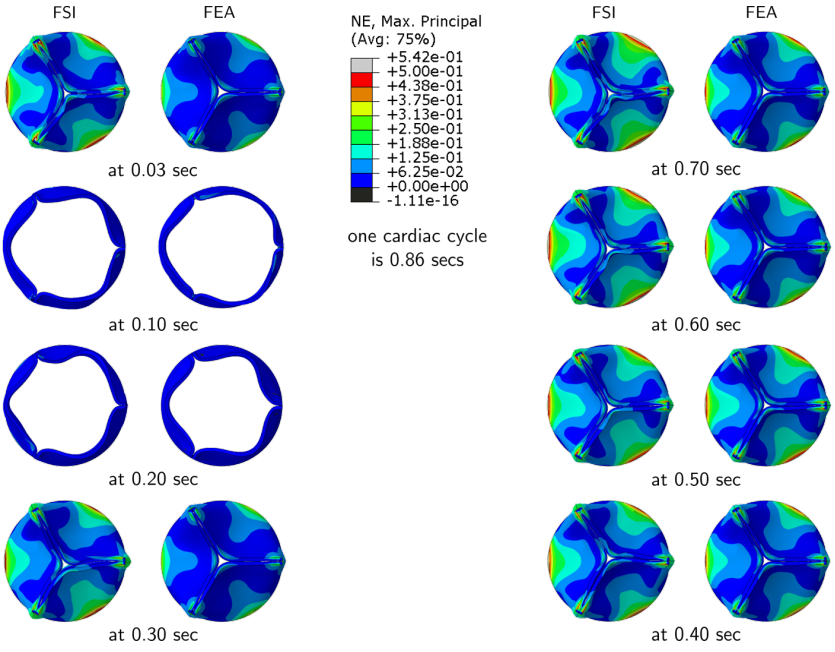

(b)

Figure 4.10: Comparison of induced stresses and strain between FSI and FEM simulations; (a) contour plots for maximum principal stresses [MPa] and (b) maximum principal nominal strains in the valve

principle stresses and maximum principal nominal strains experienced by the valves in both FEA and FSI study are plotted in Fig. 4.10a. The effective

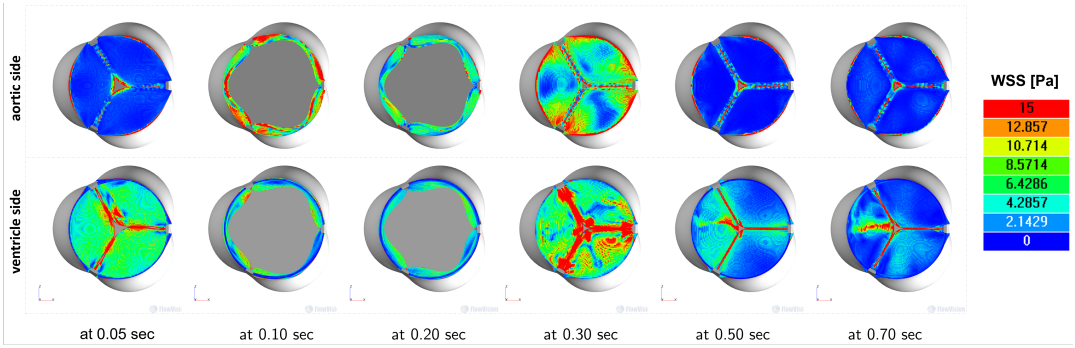

Figure 4.11: Contour plots of WSS at different time points in one cardiac cycle on the ventricle and aortic side

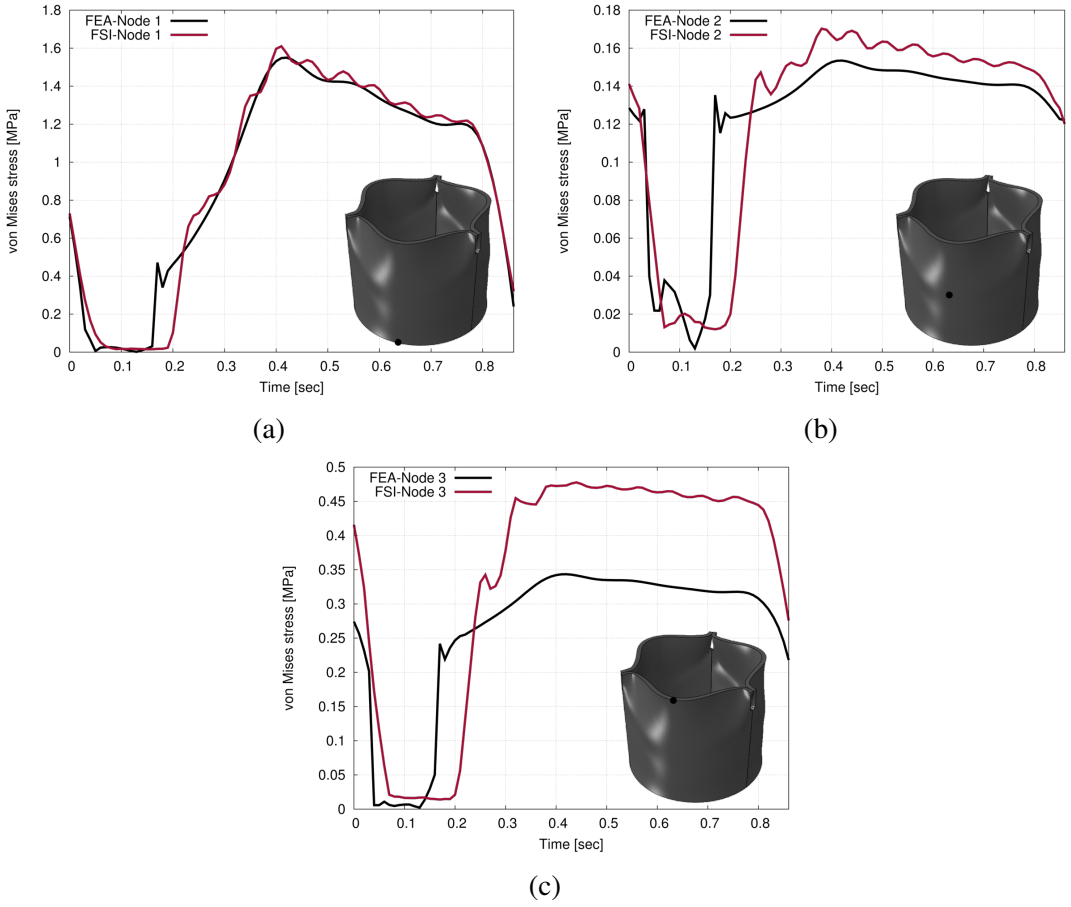

Figure 4.12: Comparison of von Mises stress between decoupled FEA and coupled FSI on a node at (a) the commissure, (b) the belly and (c) the free edge region of the valve;

von Mises stresses were sampled at three different nodes along the centre line of a leaflet, from both the FSI and the decoupled FEA simulations. Higher

effective stresses are observed at the belly (Fig. 4.12b) and free edge (Fig. 4.12c) region of the valve (in the FSI simulation) during the diastolic phase. These higher stresses are attributed to the fluid hammer effect, which cannot be captured in a decoupled FEA simulation. This reiterates the need for FSI study over decoupled FEA study to predict the valve kinematics, as suggested by Luraghi et al. [2017]. As FSI vs. decoupled FEA simulation was not the primary focus of this work, further detailed comparison of these methods have not been reported in this work.

One can also determine various useful indicators such as pressures (Fig. 4.8) & velocity fields (Fig. 4.8), areas of abnormal recirculation, vortices (Fig. 4.9 at 0.5s) and leakages (see velocity distribution in Fig. 4.8 at 0.5s & 0.7s). These indicators could help in improving the valve design and the cultivation cycle. As, the primary goal of this work was to use the FSI simulations to evaluate the kinematics of siTexValve (which is a composite valve) further detailed analysis of the flow domain has not been reported in this work. Furthermore, an extensive process of validation would be required with measurements of other quantities like velocities (e.g. by means of particle image velocimetry) or quantification of valve displacement/deformation using digital image correlation. Appendix E evaluating the wall shear stress has been included for the sake of completeness.

An overall good correlation of the results indicate that the coupled FSI simulation carried out using the explicit Abaqus and implicit FlowVision solvers can reasonably predict the flow dynamics around the valve. Although there are notable differences between in-vitro and in-silico tests, important parameters like duration of valve opening, valve closing and the instant of maximum valve opening were similar (see Fig. 4.6a, 4.6b, 4.7b). Also, considering that the siTexValve was subjected to complex loading conditions leading to large displacements and deformations, a good correlation between the simulation

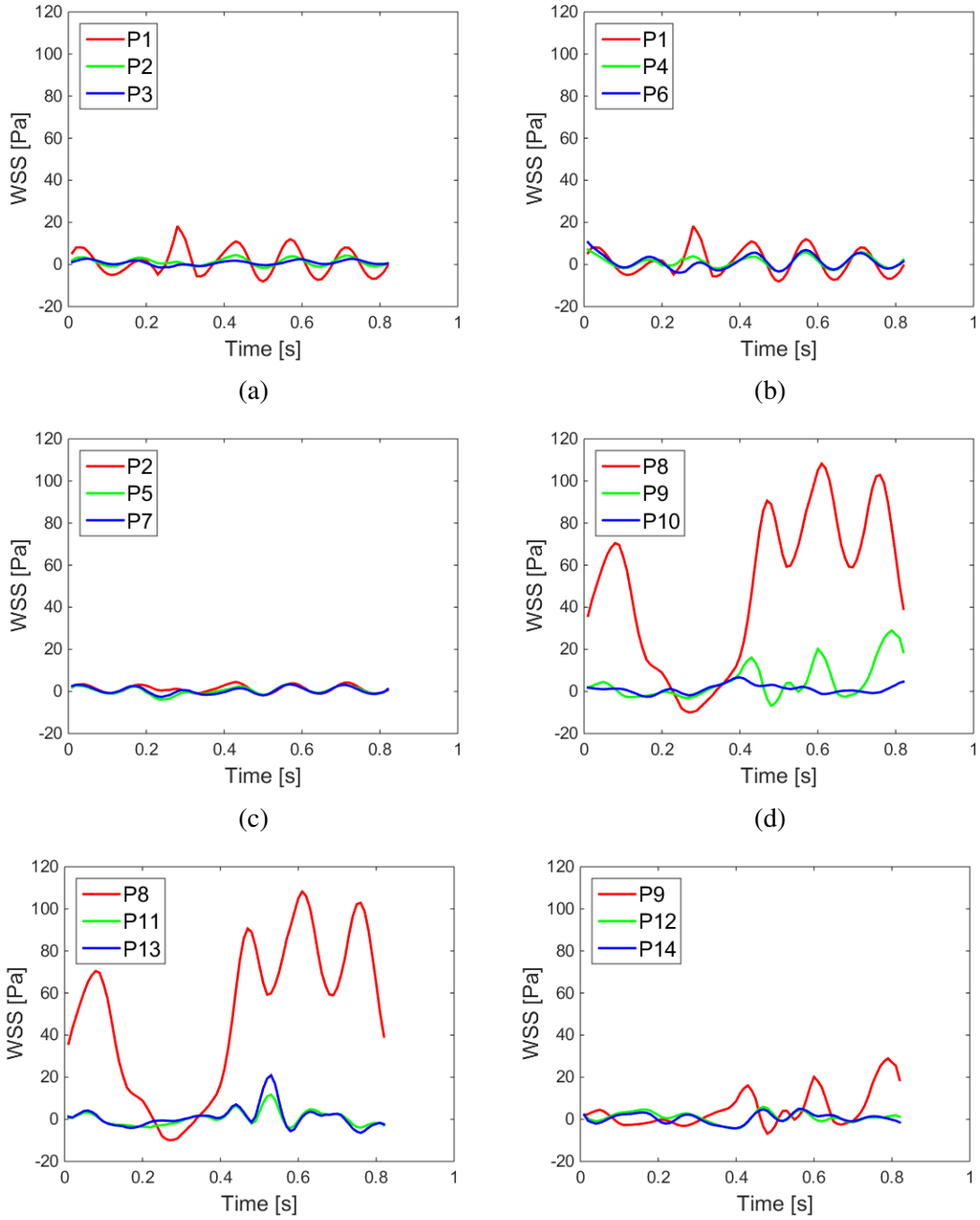

Figure 4.13: Wall Shear Stress for different points (see Fig. 4.14) over one cardiac cycle T = 0.86s

and experimental results confirms the credibility of the multi-scale modelling approach proposed in Sodhani et al. [2018b] for determining robust material parameters.

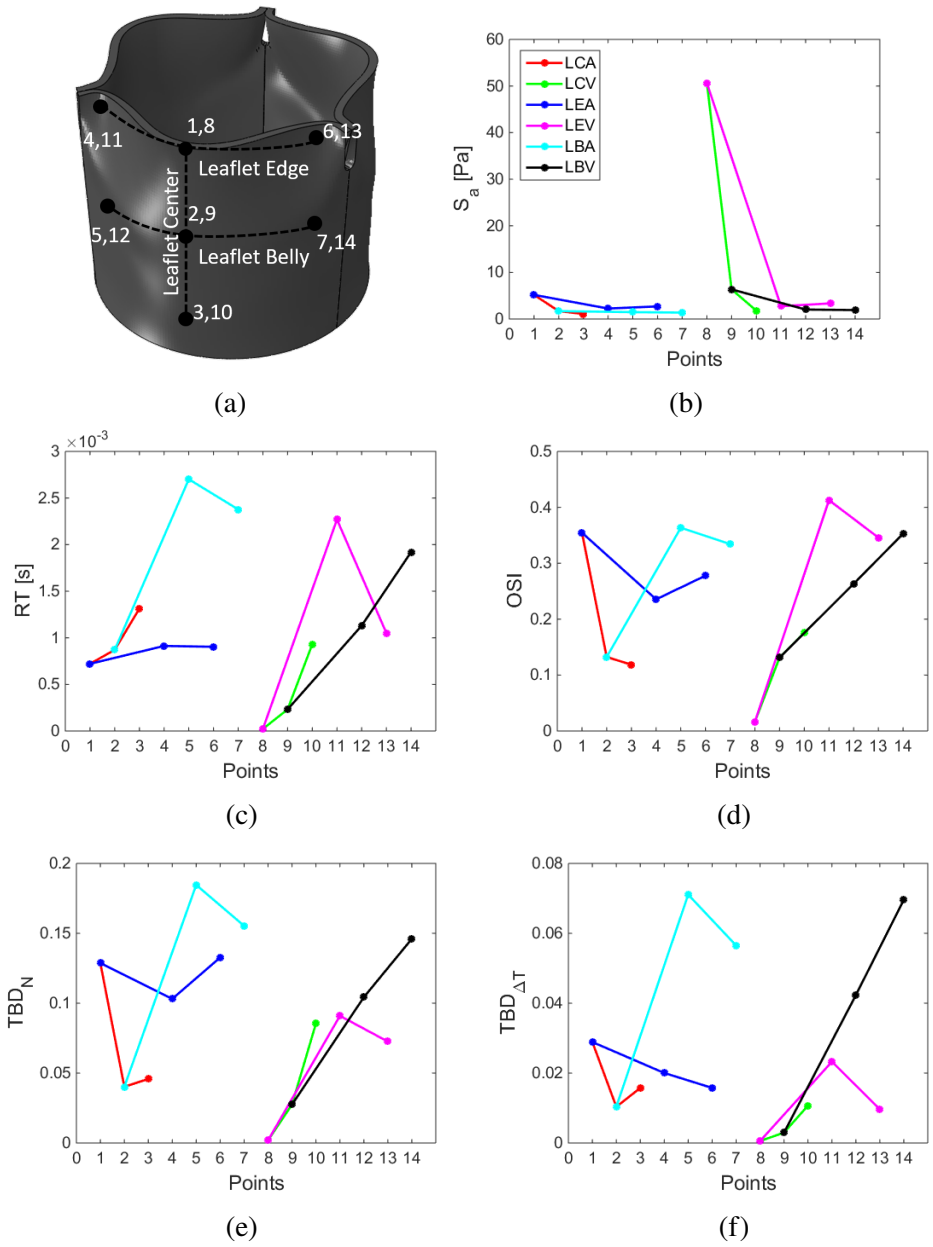

Figure 4.14: Different parameters for risk analysis are plotted for three points in a line at different regions of a leaflet on both aortic and the ventricle side. (a) points on a leaflet for evaluation (1-7 on the aortic side and 8-14 on the ventricle side); (b) average magnitude wall shear stress (S_a); (c) retention time (RT); (d) Oscillatory Shear Index (OSI);(e) Three band decomposition (number of time intervals) TBD_N;(f) Three band decomposition (time interval) $TBD_{\Delta T}$. Legends are as follows: LCA-Line in the Center of leaflet on Aortic side, LCV - Line in the Center of leaflet on Ventricle side, LEA - Line at the Edge of leaflet on Aortic side, LEV - Line at the Edge of leaflet on Ventricle side, LBA - Line in the Belly of leaflet on Aortic side, LBV - Line in the Belly of leaflet on Ventricle side

Fig. 4.13 depicts the time evolution of the computed WSS signal at the fourteen control points P1 to P14 of the fluid-valve interface, where points 1-7 are on the aortic side while the rest are on the ventricle side of the valve (see Fig. 4.14). Moderate oscillating values of the shear stress (peak values less than 20 Pa) are obtained for most of the points in the valve, except the central points on the valve edge (P1 and P8). These features are further confirmed by the time-averaged WSS values within the six distinct regions reported in Fig. 4.14. The high shear stresses (higher at P8 than at P1) are due to the high fluid velocities experienced by the centre points of leaflet edge due to incomplete closure of the valve, as explained earlier. Therefore, the wall-shear stress magnitude predicted along the ventricle side is consistently higher than that computed along the aortic side. This can also be seen from the contour plots of the wall-shear stress on either side of the valve in Fig. 4.11. As expected, the leaflets experience the flow transitioning from unidirectional/pulsatile at the base to oscillating/recirculating at the belly and edge on the aortic side. This is due to the presence of sinus of Valsalva in the computations, which assist in flow recirculation. Also, as the outlets from the sinus of Valsalva into the coronary arteries was not considered, the recirculation of the fluid persists for the entire duration of diastole. Contrary to this, the ventricle side mostly experiences a unidirectional flow which transitions into recirculating zones close to the stitch areas of the leaflets. But, as the retention time of the fluid is in the order of 10^{-3}, risk of deposition and growth of thrombus are rather low. This is further confirmed by the low values (in comparison to the values mentioned in Nestola et al. [2015]) obtained for the two novel risk predictors TBD_N and $TBD_{\Delta T}$. Due to the lack of other experimental or computational data for direct comparison of the risk predictors for the siTexValve when tested in the current experimental set-up, risk analysis presented here is used to evaluate the trends obtained for different risk indicators mentioned in the literature. These

indicators also help in quantifying the hemodynamics of the flow around the valves.

The current study and the approach used have its fair share of limitations, primary being the lack of details like stents or elastic domain resulting in simplification of the case study to conserve the computational costs. This could be overcome by using reduced order approaches (e.g. see Yang and Veneziani [2017]; Bertagna and Veneziani [2014]; Radermacher and Reese [2016]) and optimal utilization of computational resources when simulating the true case sans simplifications. The presence of compliant compartment, stent and the compliance chamber (using multi-scale flow simulations) on the aortic side of the valve would further stabilize the valve motion leading to more accurate valve simulations. Availability of Digital Image Correlation to track valve kinematics and Particle Image Velocimetry to observe the flow patterns would further enhance the evaluation of the robustness and accuracy of the simulations. An optimum asymmetry could also be introduced in the valve model to reduce leakage.

The coupled FSI simulations were carried out on a single node with 16 processors and required around 120 hours for two complete cycles. In contrast, the decoupled FEA simulation for the valve required 48 hours for two complete cycles.

In the current study, multi-scale modelling strategy have been used in a traditional sense of a fibre reinforced composites. The material parameters obtained were appropriate phenomenological representation of underlying constitutes and their structural response. In recent works, e.g. a study by Bianchi et al. [2017], multi-scale modelling has been used to model the tissues structure of an aortic section based on parameters having a clear histological and biochemical meaning. In principle, the current method along with the approach presented in Bianchi et al. [2017], can form a complementary multi-scale method for

TexValve. The multi-scale modelling approach [Sodhani et al. [2018a]] could further be coupled with tissue growth and remodelling models (like Loerakker et al. [2016]) to predict the macroscopic behaviour of textile reinforcements on tissue development in TexValves.

4.5 Conclusion

One of the major challenges with heart valve simulations is the determination of the material properties of the valve. Often, contrary to reality, the valves are assumed to be linear elastic in these simulations [Van Loon et al. [2005]; Koch et al. [2010]; Hsu et al. [2014]; Kamensky [2015]]. This is because, it is difficult to conduct experiments on tissues. Above that, determining a statistically converged experimental result can be very expensive. Therefore, to accurately predict the valve properties and its kinematics, a multi-scale modelling method was proposed in Sodhani et al. [2018a,b]. This method was initially evaluated for a standard composite specimen to evaluate its robustness and accuracy, before using it to evaluate the valve kinematics and validating it with the in-vitro tests conducted on silicone embedded textile reinforced heart valve (siTexValve), where, silicone was used as a replacement for tissue models. The FSI setup used a commercially available tool for modified IB-FSI method with adaptive re-meshing of the fluid domain whereas the material parameters of the tubular valve were derived from the hierarchical multi-scale method. Four hierarchical levels were introduced to derive the properties of the valve starting with its constituents (PET fibres and silicone matrix) and accounting for the textile structure Sodhani et al. [2016]. The FSI setup was used to predict the flow rate and geometric orifice area of the valve subjected to systemic circulation. In-vitro and in-silico systolic flow rate (Fig. 4.6a) and geometric orifice area ratio (Fig. 4.6b) were in good agreement for the considered "close-open-close" phase, i.e., one beat cycle of 0.86s. Hence,

the results produced in this study validate the numerical methodology used to determine the material properties as well as simulate the valve kinematics and flow dynamics.

Clearly, the objective of this work was to evaluate if the multi-scale modelling approach and the structural model of the tubular valves were capable of reproducing the in-vitro test results. As the simulation results obtained were in good agreement with the experimental results, it can be stated that advanced validated in-silico models can expedite the development process of TexValves. These methods represent useful tools in determining design errors and have the potential for optimizing the implant before the fabrication of prototypes.

This study proves the viability of using the multi-scale methodology in conjunction with FSI simulation to evaluate the valve behaviour. Therefore, the method is applicable for initial development of hybrid reinforced valves, and further investigation into the method without the simplifying assumptions are being conducted.

Appendix A: Governing equations

The computational domain is denoted by $\Omega = \Omega_s \cup \Omega_f$, confined within the boundary B_0, where Ω_s is the structural domain surrounded by boundary B_{s_0} and Ω_f is the fluid domain. Considering d'Alembert's principle, the balance of momentum for both structure and fluid can be expressed in tensor notations as:

$$\rho^{f,s}\dot{\mathbf{v}}^{f,s} - \bigtriangledown \cdot \boldsymbol{\sigma}^{f,s} + \rho\,\mathbf{f}^{f,s} = \mathbf{0} \tag{4.13}$$

where, the superscripts s and f represent the structural and fluid domains, respectively. $\mathbf{f}^{f,s}$ represent the body force vectors, such as gravity. For the structural domain, the velocity $\mathbf{v}^s$, is the total (or material) time derivative of the displacement field $\mathbf{u}^s$, i.e., $\mathbf{v}^s = \dot{\mathbf{u}}^s$. In the structural form (superscript s) of

the eq. 4.13, which is used in a Lagrangian description, the first two terms are associated with inertia and internal stresses, respectively. The structural stress follows from the non-linear hyperelastic orthotropic Fung's material model. For the fluid domain which is represented using Eulerian description, eq. 4.13 can be rewritten as (neglecting the superscript f)

$$\frac{\partial(\rho \mathbf{v})}{\partial t} + \bigtriangledown \cdot (\rho \mathbf{v} \otimes \mathbf{v}) = - \bigtriangledown \cdot p\mathbf{I} + \bigtriangledown \cdot \boldsymbol{\tau} + \mathbf{f} = 0 \tag{4.14}$$

where, ρ is the density, $\mathbf{v}$ the flow velocity, $\bigtriangledown\cdot$ the divergence operator, p the static pressure, $\mathbf{I}$ the identity matrix and $\boldsymbol{\tau}$ the deviatoric parts of the stress tensor. The inertia term has been split in variational and convective part whereas, assuming an incompressible Newtonian fluid, the internal stress has been split into volumetric and deviatoric part. For an incompressible fluid considering $\bigtriangledown \cdot \mathbf{v}$, divergence of the deviatoric stress, $\boldsymbol{\tau} = \mu(\bigtriangledown \mathbf{v} + \bigtriangledown \mathbf{v}^T)$ results into

$$\bigtriangledown \cdot \boldsymbol{\tau} = \mu \bigtriangledown \cdot (\bigtriangledown \mathbf{v} + \bigtriangledown \mathbf{v}^T) = \mu \bigtriangledown^2 \mathbf{v}. \tag{4.15}$$

Using eq. 4.15 in eq. 4.14, and averaging over the density of fluid results into the incompressible Navier-Stokes equation

$$\frac{\partial(\mathbf{v})}{\partial t} + (\mathbf{v} \cdot \bigtriangledown)\mathbf{v} - \frac{\mu}{\rho} \bigtriangledown^2 \mathbf{v} = - \bigtriangledown \frac{p}{\rho} + \mathbf{f} \tag{4.16}$$

As the highly dynamic movement of the valve would result in turbulent flows around the valve edges, the effective viscosity μ is calculated using the standard $\mathbf{k} - \boldsymbol{\epsilon}$ turbulent model. To maintain the no-slip condition along the fluid-structure interface B_{s_0}, the following Dirichlet and Neumann conditions can be imposed

$$\mathbf{v}^s = \mathbf{v}^f \text{ on } B_{s0}, \tag{4.17}$$

$$\boldsymbol{\sigma}^s \mathbf{n} = \boldsymbol{\sigma}^f \mathbf{n} \text{ on } B_{s0} \tag{4.18}$$

The non-conforming mesh methods enforces the Dirichlet condition i.e., eq. 4.17, whereas, the conforming mesh methods requiring regular mesh updates enforces the Neumann condition i.e. eq. 4.18. The non-conforming mesh methods can be derived from the theorem of Lagrange multipliers [Haug [1992]], where in most cases they appear as source (or, forcing) terms in the fluid equation. Thus, in these methods, computation of the Lagrange multipliers is essential and directly affects the accuracy of the fluid and solid solutions (for more detailed study readers are referred to Hou et al. [2012]).

Appendix B: Stitching simulation

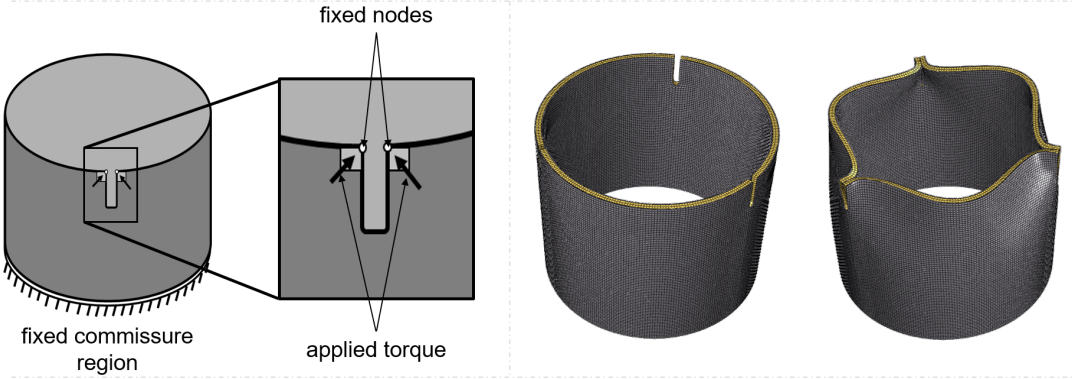

Figure 4.15: Boundary condition and loads on the initial tubular construct to obtain the stitched topology of the valve. Schematic representation (left) and pre & post stitch geometry and FE mesh (right).

To obtain the initial stitched configuration of the tubular valve, U-shaped cuts were introduced in the model to avoid large distortion of elements in the stitch zones. Opposites torques (or rotational forces) were applied on small patches on either side of the U-shaped cuts while the corner node on the inner wall of U-shaped cut was fixed to act like a pivot and twist the valve into stitch

like position. The twisted patches were then compressed together to obtain the topology of the stitched tubular siTexValve. The magnitude of torque and compression were obtained using an iterative process to avoid element distortion. Deformed configuration was then imported into a new model to achieve a stress free stitched valve model. Boundary conditions and applied loads are as shown in Fig. 4.15.

Appendix C: Effect of valve design on closure

As mentioned in Sec. 4.4, and demonstrated by Sun et al. [2010], presence of a small asymmetry in valve design can either improve or degrade the valve closure kinematics. An example of such an effect on improved valve closure kinetics from our ongoing investigations is presented here for completeness. In this particular case an asymmetry in the position of stitched commissure points was introduced making one leaflet of the tubular valve smaller than the other two. So far only decoupled FE simulations were used. The valve closing pattern was also compared to a similar TexValve, Fig. 4.16.

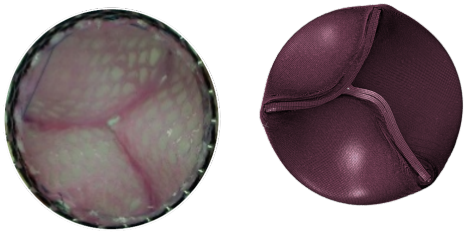

Figure 4.16: Affect of asymmetry on valve closure (right) and comparison with a similar TexValve (left).

5 Conclusions and Outlook

Native heart valves or textile reinforced tissue-engineered heart valves are neither isotropic nor do they have a linear elastic behaviour. One of the major challenges in using simulations-based development of tissue-engineered heart valve prostheses is the determination of the material properties of the composite valve. Hence, one of the goals of the current study was to develop and evaluate the competence of a hierarchical multi-scale modelling approach to predict the behaviour of the reinforcing biocompatible material. The secondary goal was to use the developed modelling approach, to predict the material properties of a prosthetic valve, which were in turn to be used in the simulation of the composite aortic valve. The hierarchical multi-scale method was initially evaluated for its robustness and accuracy using a textile reinforced silicone composite test specimen. The macro-structure was divided into several representative structures using both realistic approximation of the geometry, generated using CT data as well as idealized representative geometrical units. Both these approaches maintained the effective fibre volume fraction of the composite. Owing to the quality and complexity of the reconstructed geometry, it was found that the hierarchical multi-scale method using idealized structures was more robust in predicting the behaviour of the macro structure.

Having established the modelling approach, the method was used to derive the material properties of the macro scale composite valve. The derived material properties were then used in a dry FEM simulation of the valve. The predicted valve kinematics were found to be in good correlation with the experimental

in-vitro valve kinematics but lacked the hemodynamical performance of the valve. A comprehensive comparison of both the valve kinematics as well as its hemodynamical behaviour was evaluated using a multi-physics fluid-structure interaction (FSI) simulation for one heart beat. These simulations predicted the flow rate and geometric orifice area of the valve. In-vitro and in-silico systolic flow rate and geometric orifice area ratio were in good agreement, with some deviations during the diastolic phase of a beat. The predicted stresses and strains in the valve from the FSI and FEM simulations were comparable in most regions of the valve. But some zones of the valve experienced significantly higher stresses in FSI simulations compared to FEM simulations which were attributed to the fluid hammer effect, not included in the dry FEM simulations. This implicates the importance of multi-physics FSI over dry FEM simulations.

The presented multi-scale technique could be used to study knitted textile-tissue composites which are otherwise difficult to experiment on, and to optimize their structure for mechanical biocompatibility. Apart from predicting the global response, the current approach can also predict non-affine local deformation along with the stress and strain states in the matrix - to better engineer the ingrowth of tissues. Therefore, this method could be used to optimize the textile structure along with its orientation saving on both time and resources while improving the product. The presented approach could eventually aid in improved understanding of engineered tissue in presence of a scaffold (textile mesh) leading to improved biocompatible topologies. Hence, advanced validated in-silico models can expedite the development process of TexValves.

5.1 Outlook

To further enhance the simulation technique, a material model accounting for extra-cellular fibre (elastin and collagen) alignment within the matrix under cyclic loading during cultivation needs to be developed/employed. A quick

evaluation of the presented multi-scale technique to predict the effect of reinforcement in a tissue-engineered construct was carried out using a recently published material model by Loerakker et al. [2016]. This material model was developed for computational analysis of cell-mediated compaction and collagen remodelling in tissue-engineered heart valves.

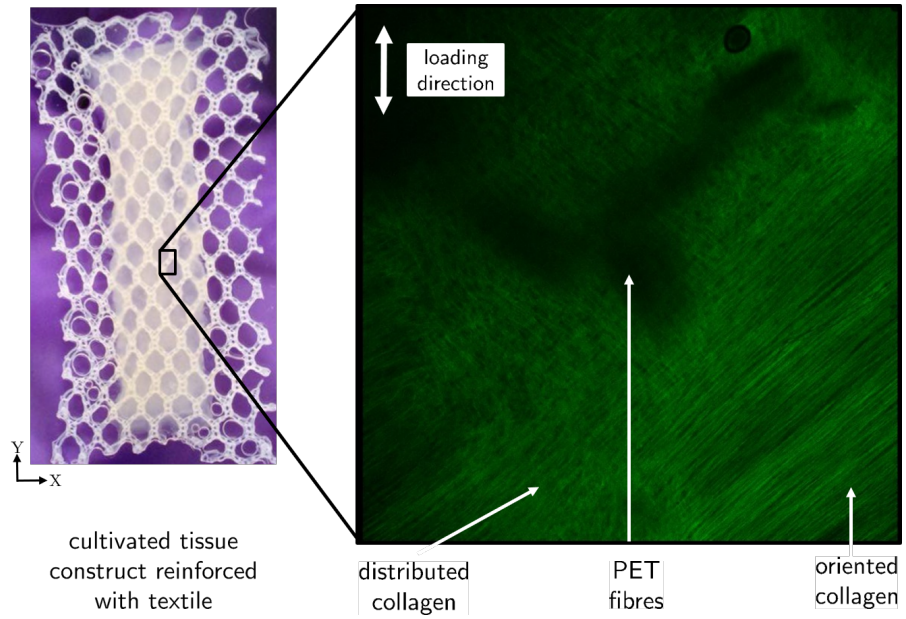

Figure 5.1: Cultivated tissue construct with reinforcing textile and observed collagen orientation using fluoroscopy.

In this evaluation, a tissue construct reinforced with the presented biomedical textile was cultivated for four weeks and analysed for the orientation of developed/grown collagen fibres. The tissue material model provided by Prof. Loerakker was coupled with the textile level RUC model and subjected to the same cultivation cycle of 15% strain at a frequency of 2Hz for four weeks . The textile structure was modelled using the Fungs orthotropic hyperelasticity with parameters derived using the multi-scale method, whereas the matrix was modelled using the mentioned tissue model with reported parameters in Loerakker et al. [2016]. The tissue construct was observed using the fluoroscopy technique for collagen orientations around the reinforcing textile (Fig.

5.1) and compared with the predicted collagen orientation from the simulations(Fig. 5.2). The predicted collagen orientations using the numerical model was closely matching the experimental result, where, one can observe a distinct collagen orientation in the developed tissue away from the textile fibres, and distributed collagen orientations close to the textile fibres.

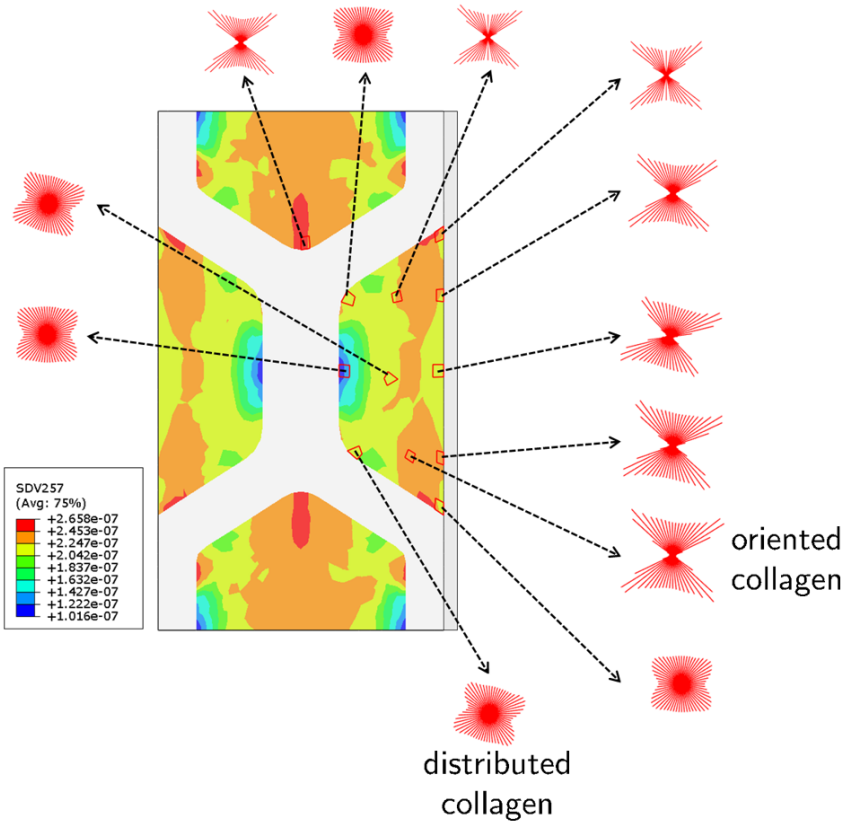

Figure 5.2: Predicted collagen fibre orientations close to and away from the textile structure.

This study was conducted as a proof of concept of the ability of the presented modelling approach in predicting collagen remodelling, and requires a comprehensive statistical evaluation for different loading conditions, cultivation cycles, reinforcing structures, etc. before being used in the development of textile reinforced tissue engineered heart valves.

List of Figures

List of Tables

Bibliography

Adanur, S., Liao, T.. 3D modeling of textile composite preforms. Compos Part B Eng 1998;29:787–793. doi:10.1016/S1359-8368(98)00036-5.

Aksenov, A., Dyadkin, A., Gudzovsky, A.. Numerical simulation of car tire aquaplaning. In: ECCOMAS Conference Computational Fluid Dynamics. 1996. p. 815–820.

Aksenov, A., Dyadkin, A., Pokhilko, V.. Overcoming of barrier between cad and cfd by modified finite volume method. ASME-Publications-PVP 1998;377:79–83.

Annerel, S., Degroote, J., Claessens, T., Dahl, S.K., Skallerud, B., Hellevik, L.R., Van Ransbeeck, P., Segers, P., Verdonck, P., Vierendeels, J.. A fast strong coupling algorithm for the partitioned fluid–structure interaction simulation of BMHVs. Computer Methods in Biomechanics and Biomedical Engineering 2012;15(12):1281–1312.

Antonietti, P.F., Biscari, P., Tavakoli, A., Verani, M., Vianello, M.. Theoretical study and numerical simulation of textiles. Appl Math Model 2011;35(6):2669–2681. doi:10.1016/j.apm.2010.11.062.

Argento, G., Simonet, M., Oomens, C., Baaijens, F.. Multi-scale mechanical characterization of scaffolds for heart valve tissue engineering. Journal of Biomechanics 2012;45(16):2893–2898.

Arruda, E.M., Boyce, M.C.. A three-dimensional constitutive model for the large stretch behavior of rubber elastic materials. Journal of the Mechanics and Physics of Solids 1993;41(2):389–412. doi:10.1016/0022-5096(93)90013-6.

Assidi, M., Ben Boubaker, B., Ganghoffer, J.F.. Equivalent properties of monolayer fabric from mesoscopic modelling strategies. International Journal of Solids and Structures 2011;48(20):2920–2930. doi:10.1016/j.ijsolstr.2011.06.010.

Auricchio, F., Conti, M., Ferrara, A., Morganti, S., Reali, A.. Patient-specific simulation of a stentless aortic valve implant: the impact of fibres on leaflet performance. Computer methods in biomechanics and biomedical engineering 2014;17(3):277–285.

Bavo, A.M., Rocatello, G., Iannaccone, F., Degroote, J., Vierendeels, J., Segers, P.. Fluid-Structure Interaction Simulation of Prosthetic Aortic Valves: Comparison between Immersed Boundary and Arbitrary Lagrangian-Eulerian Techniques for the Mesh Representation. PLOS ONE 2016;11(4).

Bednarcyk, B.A., Stier, B., Simon, J.W., Reese, S., Pineda, E.J.. Meso- and micro-scale modeling of damage in plain weave composites. Composite Structures 2015;121:258–270. doi:10.1016/j.compstruct.2014.11.013.

Ben Boubaker, B., Haussy, B., Ganghoffer, J.F.. Discrete woven structure model: yarn-on-yarn friction. Comptes Rendus - Mec 2007;335(3):150–158. doi:10.1016/j.crme.2007.02.006.

Bertagna, L., Veneziani, A.. A model reduction approach for the variational

estimation of vascular compliance by solving an inverse fluid–structure interaction problem. Inverse Problems 2014;30(5):055006.

Bianchi, D., Monaldo, E., Gizzi, A., Marino, M., Filippi, S., Vairo, G.. A fsi computational framework for vascular physiopathology: A novel flow-tissue multiscale strategy. Medical Engineering & Physics 2017;47:25–37.

Böl, M., Reese, S.. Finite element modelling of rubber-like polymers based on chain statistics. International journal of solids and structures 2006;43(1):2–26.

Böl, M., Reese, S., Parker, K.K., Kuhl, E.. Computational modeling of muscular thin films for cardiac repair. Computational Mechanics 2009;43(4):535–544. doi:10.1007/s00466-008-0328-5.

Borazjani, I.. Fluid-structure interaction, immersed boundary-finite element method simulations of bio-prosthetic heart valves. Computer Methods in Applied Mechanics and Engineering 2013;257:103–116.

Borazjani, I., Sotiropoulos, F.. Curvilinear immersed boundary method for simulating fluid structure interaction with complex 3D rigid bodies. NIH Public Access 2010;227(16):7587–7620.

Caballero, A., Mao, W., Liang, L., Oshinski, J., Primiano, C., McKay, R., Kodali, S., Sun, W.. Modeling left ventricular blood flow using smoothed particle hydrodynamics. Cardiovascular Engineering and Technology 2017;8(4):465–479.

Cacciola, G., Peters, G., Schreurs, P.. A three-dimensional mechanical analysis of a stentless fibre-reinforced aortic valve prosthesis. Journal of Biomechanics 2000a;33(5):521–530.

Cacciola, G., Peters, G.W.M., Baaijens, F.P.T.. A synthetic fiber-reinforced stentless heart valve. J Biomech 2000b;33(6):653–658. doi:10.1016/S0021-9290(00)00003-8.

Chagnon, G., Rebouah, M., Favier, D.. Hyperelastic Energy Densities for Soft Biological Tissues: A Review. Journal of Elasticity 2015;120(2):129–160. doi:10.1007/s10659-014-9508-z.

Chandra, S., Rajamannan, N.M., Sucosky, P.. Computational assessment of bicuspid aortic valve wall-shear stress: Implications for calcific aortic valve disease. Biomechanics and Modeling in Mechanobiology 2012;11(7):1085–1096.

Cheung, D.Y., Duan, B., Butcher, J.T.. Current progress in tissue engineering of heart valves: multiscale problems, multiscale solutions. Expert Opinion on Biological Therapy 2015;15(8):1155–1172.

D'Amore, A., Amoroso, N., Gottardi, R., Hobson, C., Carruthers, C., Watkins, S., Wagner, W.R., Sacks, M.S.. From single fiber to macro-level mechanics: A structural finite-element model for elastomeric fibrous biomaterials. Journal of the Mechanical Behavior of Biomedical Materials 2014;39:146–161. doi:10.1016/j.jmbbm.2014.07.016.

De Hart, J., Cacciola, G., Schreurs, P., Peters, G.. A three-dimensional analysis of a fibre-reinforced aortic valve prosthesis. Journal of biomechanics 1998;31(7):629–638.

De Hart, J., Peters, G.W.M., Schreurs, P.J.G., Baaijens, F.P.T.. Collagen fibers reduce stresses and stabilize motion of aortic valve leaflets during systole. J Biomech 2004;37(3):303–311. doi:10.1016/S0021-9290(03)00293-8.

De Jong, S., Postle, R.. A General Energy Analysis of Fabric Mechanics Using Optimal Control Theory. Textile Research Journal 1978;48(3):127–135. doi:10.1177/004051757804800302.

De Tullio, M., Afferrante, L., Demelio, G., Pascazio, G., Verzicco, R.. Fluid-structure interaction of deformable aortic prostheses with a bileaflet mechanical valve. Journal of Biomechanics 2011;44(9):1684–1690.

Döbrich, O., Gereke, T., Cherif, C.. Modeling the mechanical properties of textile-reinforced composites with a near micro-scale approach. Composite Structures 2016;135:1–7.

Duhovic, M., Bhattacharyya, D.. Simulating the deformation mechanisms of knitted fabric composites. Compos Part A Appl Sci Manuf 2006;37(11):1897–1915. doi:10.1016/j.compositesa.2005.12.029.

Duong, M.T., Nguyen, N.H., Staat, M.. Physical response of hyperelastic models for composite materials and soft tissues. Asia Pacific J Comput Eng 2015;2(3):1–18. doi:10.1186/s40540-015-0015-x.

Ehret, A.E., Itskov, M.. A polyconvex hyperelastic model for fiber-reinforced materials in application to soft tissues. Journal of Materials Science 2007;42(21):8853–8863. doi:10.1007/s10853-007-1812-6.

Flamini, V., DeAnda, A., Griffith, B.E.. Immersed boundary-finite element model of fluid–structure interaction in the aortic root. Theoretical and Computational Fluid Dynamics 2016;30(1-2):139–164.

Fung, Y.C., Fronek, K., Patitucci, P.. Pseudoelasticity of arteries and the choice of its mathematical expression. American Journal of Physiology 1979;237(5):H620–H631.

Gasser, T.C., Ogden, R.W., Holzapfel, G.A.. Modelling non-symmetric collagen fibre dispersion in arterial walls. Journal of the Royal Society, Interface 2006;3(6):15–35. doi:10.1098/rsif.2005.0073.

Gizzi, A., Bernaschi, M., Bini, D., Cherubini, C., Filippi, S., Melchionna, S., Succi, S.. Three-band decomposition analysis of wall shear stress in pulsatile flows. Physical Review E 2011;83(3):031902.

Glaessgen, E., Pastore, C., Griffin, O., Birger, A.. Geometrical and finite element modelling of textile composites. Compos Part B Eng 1996;27(1):43–50. doi:10.1016/1359-8368(95)00005-4.

Goetz, W., Lim, H., Lansac, E., Weber, P., Duran, C.. A temporarily stented, autologous pericardial aortic valve prosthesis. Journal of Heart Valve Disease 2002;11(5):696–702.

Goktepe, O., Harlock, S.C.. A 3D Loop Model for Visual Simulation of Warp-knitted Structures. Journal of the Textile Institute 2002;93(March 2015):11–28. doi:10.1080/00405000208630549.

Griffith, B.E.. Immersed boundary model of aortic heart valve dynamics with physiological driving and loading conditions. International Journal for Numerical Methods in Biomedical Engineering 2012;28:317–345.

Grujicic, M., Bell, W.C., Arakere, G., He, T., Cheeseman, B.A.. A meso-scale unit-cell based material model for the single-ply flexible-fabric armor. Materials and Design 2009;30(9):3690–3704. doi:10.1016/j.matdes.2009.02.008.

Gunning, P.S., Vaughan, T.J., McNamara, L.M.. Simulation of self expanding transcatheter aortic valve in a realistic aortic root: Implications of deployment geometry on leaflet deformation. Annals of Biomedical Engineering 2014;42(9):1989–2001.

Hallal, A., Younes, R., Fardoun, F.. Review and comparative study of analytical modeling for the elastic properties of textile composites. Compos Part B Eng 2013;50(July):22–31. doi:10.1016/j.compositesb.2013.01.024.

Hart, K., De Jong, S., Postle, R.. Analysis of the single bar warp knitted structure using an energy minimization technique: part i: theoretical development. Textile Research Journal 1985;55(8):489–498.

Hasani, H., Hassanzadeh, S., Abghary, M.J., Omrani, E.. Biaxial weft-knitted fabrics as composite reinforcements: A review. Journal of Industrial Textiles 2017;46(7):1439–1473. doi:10.1177/1528083715624256.

Hassani, B., Hinton, E.. A review of homogenization and topology optimization I—homogenization theory for media with periodic structure. Computers and Structures 1998;69(6):707–717. doi:10.1016/S0045-7949(98)00131-X.

Haug, E.J.. Intermediate dynamics, 1992.

Hernández-Gascón, B., Peña, E., Melero, H., Pascual, G., Doblaré, M., Ginebra, M.P., Bellón, J.M., Calvo, B.. Mechanical behaviour of synthetic surgical meshes: Finite element simulation of the herniated abdominal wall. Acta Biomaterialia 2011;7(11):3905–3913. doi:10.1016/j.actbio.2011.06.033.

Hibbitt, , Karlsson, , Sorensen, . ABAQUS/standard user's Manual. volume 1. Hibbitt, Karlsson & Sorensen, 2001.

Himburg, H.A., Grzybowski, D.M., Hazel, A.L., LaMack, J.A., Li, X.M., Friedman, M.H.. Spatial comparison between wall shear stress measures and porcine arterial endothelial permeability. American Journal of Physiology-Heart and Circulatory Physiology 2004;286(5):H1916–H1922.

Holzapfel, G.A.. Computational biomechanics of soft biological tissue. Encyclopedia of computational mechanics 2004;.

Holzapfel, G.A., Gasser, T.C.. A viscoelastic model for fiber-reinforced composites at finite stains: Continuum basis, computational aspects and applications. Computer Methods in Applied Mechanics and Engineering 2001;190(34):4379–4403. doi:10.1016/S0045-7825(00)00323-6.

Honglian, C., Mingqiao, G., Gaoming, J.. Three-Dimensional Simulation of Warp-knitted Fabric. Fibres & Textiles in Eastern Europe 2009;17(3):66–69.

Hou, G., Wang, J., Layton, A.. Numerical methods for fluid-structure interaction - A review. Communications in Computational Physics 2012;12(2):337–377.

Hsu, M.C., Kamensky, D., Bazilevs, Y., Sacks, M.S., Hughes, T.J.R.. Fluid–structure interaction analysis of bioprosthetic heart valves: significance of arterial wall deformation. Computational Mechanics 2014;54(4):1055–1071.

Hsu, M.C., Kamensky, D., Xu, F., Kiendl, J., Wang, C., Wu, M.C., Mineroff, J., Reali, A., Bazilevs, Y., Sacks, M.S.. Dynamic and fluid–structure interaction simulations of bioprosthetic heart valves using parametric design with T-splines and Fung-type material models. Computational Mechanics 2015;55(6):1211–1225.

Huang, Z.M., Ramakrishna, S.. Micromechanical modeling approaches for the stiffness and strength of knitted fabric composites: a review and comparative study. Compos Part A Appl Sci Manuf 2000;31(5):479–501. doi:10.1016/S1359-835X(99)00083-4.

Humphrey, J.D.. Mechanics of the arterial wall: review and directions. Critical Reviews in Biomedical Engineering 1994;23(1-2):1–162.

Iung, B., Vahanian, A.. Epidemiology of valvular heart disease in the adult. Nature Reviews Cardiology 2011;8(3):162–172.

Jana, S., Tefft, B.J., Spoon, D.B., Simari, R.D.. Scaffolds for tissue engineering of cardiac valves. Acta Biomater 2014;10(7):2877–2893. doi:10.1016/j.actbio.2014.03.014.

Joda, A., Jin, Z., Haverich, A., Summers, J., Korossis, S.. Multiphysics simulation of the effect of leaflet thickness inhomogeneity and material anisotropy on the stress–strain distribution on the aortic valve. Journal of Biomechanics 2016;49(12):2502–2512.

Kamensky, D.. An immersogeometric variational framework for fluid – structure interaction : application to bioprosthetic heart valves. Computer Methods in Applied Mechanics and Engineering 2015;284:1005–1053.

Katayama, S., Umetani, N., Sugiura, S., Hisada, T.. The sinus of Valsalva relieves abnormal stress on aortic valve leaflets by facilitating smooth closure. Journal of Thoracic and Cardiovascular Surgery 2008;136(6):1528–1535.e1.

Kim, H., Lu, J., Sacks, M.S., Chandran, K.B.. Dynamic simulation of bioprosthetic heart valves using a stress resultant shell model. Annals of Biomedical Engineering 2008;36(2):262–275.

King, M.J., Jearanaisilawong, P., Socrate, S.. A continuum constitutive model for the mechanical behavior of woven fabrics. International Journal of Solids and Structures 2005;42(13):3867–3896. doi:10.1016/j.ijsolstr.2004.10.030.

Koch, T., Reddy, B., Zilla, P., Franz, T.. Aortic valve leaflet mechanical properties facilitate diastolic valve function. Computer Methods in Biomechanics and Biomedical Engineering 2010;13(2):225–234.

Kyosev, Y., Angelova, Y., Kovar, R.. 3D Modelling of plain weft knitted structures from compressible yarn. Res J Text Appar 2005;9(1):88–97.

Lechat, C., Bunsell, A.R., Davies, P.. Tensile and creep behaviour of polyethylene terephthalate and polyethylene naphthalate fibres. Journal of Materials Science 2011;46(2):528–533. doi:10.1007/s10853-010-4999-x.

Li, K., Sun, W.. Simulated thin pericardial bioprosthetic valve leaflet deformation under static pressure-only loading conditions: Implications for percutaneous valves. Annals of Biomedical Engineering 2010;38(8):2690–2701.

Li, Y., Stier, B., Bednarcyk, B., Simon, J.W., Reese, S.. The effect of fiber misalignment on the homogenized properties of unidirectional fiber reinforced composites. Mech Mater 2016;92:261–274. doi:10.1016/j.mechmat.2015.10.002.

Li, Y., Yang, L., Chen, S., Xu, L.. Three Dimensional Simulation of Weft Knitted Fabric Based on Surface Model. Comput Model New Technol 2014;18(3):52–57.

Lin, H., Brown, L.P., Long, A.C.. Modelling and simulating textile structures using texgen. In: Advanced Materials Research. Trans Tech Publ; volume 331; 2011. p. 44–47.

Lin, H., Zeng, X., Sherburn, M., Long, a.C., Clifford, M.J.. Automated geometric modelling of textile structures. Textile Research Journal 2012;82(16):1689–1702. doi:10.1177/0040517511418562.

Llames, S., García, E., Hernández, J.O., Meana, Á.. Tissue bioengineering and artificial organs. In: Stem Cell Transplantation. Springer; 2012. p. 314–336.

Loerakker, S., Argento, G., Oomens, C.W.J., Baaijens, F.P.T.. Effects of valve geometry and tissue anisotropy on the radial stretch and coaptation area of tissue-engineered heart valves. Journal of Biomechanics 2013;46(11):1792–1800.

Loerakker, S., Ristori, T., Baaijens, F.P.. A computational analysis of cell-mediated compaction and collagen remodeling in tissue-engineered heart valves. Journal of the Mechanical Behavior of Biomedical Materials 2016;58:173–187.

Luraghi, G., Wu, W., De Gaetano, F., Rodriguez Matas, J.F., Moggridge, G.D., Serrani, M., Stasiak, J., Costantino, M.L., Migliavacca, F.. Evaluation of an aortic valve prosthesis: Fluid-structure interaction or structural simulation? Journal of Biomechanics 2017;58:45–51.

Mao, W., Caballero, A., McKay, R., Primiano, C., Sun, W.. Fully-coupled fluid-structure interaction simulation of the aortic and mitral valves in a realistic 3d left ventricle model. PLOS ONE 2017;12(9):e0184729.

Mao, W., Li, K., Sun, W.. Fluid-Structure Interaction Study of Transcatheter Aortic Valve Dynamics Using Smoothed Particle Hydrodynamics. Cardiovascular Engineering and Technology 2016;7(4):374–388.

Marom, G., Haj-Ali, R., Raanani, E., Schäfers, H.J., Rosenfeld, M.. A fluid-structure interaction model of the aortic valve with coaptation and compliant aortic root. Medical & Biological Engineering & Computing 2012;50(2):173–182.

Martins, P., Natal Jorge, R., Ferreira, A.. A comparative study of several material models for prediction of hyperelastic properties: Application to silicone-rubber and soft tissues. Strain 2006;42(3):135–147.

Maurer, M.M., Röhrnbauer, B., Feola, A., Deprest, J., Mazza, E.. Mechanical biocompatibility of prosthetic meshes: A comprehensive protocol for mechanical characterization. Journal of the Mechanical Behavior of Biomedical Materials 2014;40:42–58. doi:10.1016/j.jmbbm.2014.08.005.

Mazza, E., Ehret, A.E.. Mechanical biocompatibility of highly deformable biomedical materials. Journal of the Mechanical Behavior of Biomedical Materials 2015;48:100–124. doi:10.1016/j.jmbbm.2015.03.023.

Mingxing Xiao, , Zhaofeng Geng, , Kaijun Liao, . An improved model of rigid bodies for plain-weave fabrics based on the dynamics of multibody systems. Textile Research Journal 2011;81(13):1381–1394. doi:10.1177/0040517511402128.

Mohammadi, H., Cartier, R., Mongrain, R.. 3D physiological model of the aortic valve incorporating small coronary arteries. International Journal for Numerical Methods in Biomedical Engineering 2017;33(5):1–13.

Moreira, R., Neusser, C., Kruse, M., Mulderrig, S., Wolf, F., Spillner, J., Schmitz-Rode, T., Jockenhoevel, S., Mela, P.. Tissue-engineered fibrin-based heart valve with bio-inspired textile reinforcement. Advanced Healthcare Materials 2016;5(16):2113–2121.

Moreira, R., Velz, T., Alves, N., Gesche, V.N., Malischewski, A., Schmitz-Rode, T., Frese, J., Jockenhoevel, S., Mela, P.. Tissue-Engineered Heart Valve with a Tubular Leaflet Design for Minimally Invasive Transcatheter Implantation. Tissue Eng Part C Methods 2014a;00(00):150127064141009.

Moreira, R., Velz, T., Alves, N., Gesche, V.N., Malischewski, A., Schmitz-Rode, T., Frese, J., Jockenhoevel, S., Mela, P.. Tissue-engineered heart valve with a tubular leaflet design for minimally invasive transcatheter implantation. Tissue Engineering Part C: Methods 2014b;21(6):530–540.

Morganti, S., Auricchio, F., Benson, D.J., Gambarin, F.I., Hartmann, S., Hughes, T.J.R., Reali, A.. Patient-specific isogeometric structural analysis of aortic valve closure. Computer Methods in Applied Mechanics and Engineering 2015;284:508–520.

Morganti, S., Conti, M., Aiello, M., Valentini, A., Mazzola, A., Reali, A., Auricchio, F.. Simulation of transcatheter aortic valve implantation through patient-specific finite element analysis: Two clinical cases. Journal of Biomechanics 2014;47(11):2547–2555.

Nadler, B., Papadopoulos, P., Steigmann, D.J.. Multiscale constitutive modeling and numerical simulation of fabric material. International Journal of Solids and Structures 2006;43(2):206–221. doi:10.1016/j.ijsolstr.2005.05.020.

Namiri, M., Ashtiani, M.K., Mashinchian, O., Hasani-Sadrabadi, M.M., Mahmoudi, M., Aghdami, N., Baharvand, H.. Engineering natural heart valves: possibilities and challenges. Journal of Tissue Engineering and Regenerative Medicine 2017;11(5):1675–1683.

Nayfeh, A.H., Kress, G.R.. Non-linear constitutive model for plain-weave composites. Compos Part B 1997;8368:627–634.

Nestola, M., Gizzi, A., Cherubini, C., Filippi, S., Succi, S.. Novel risk predictor for thrombus deposition in abdominal aortic aneurysms. EPL (Europhysics Letters) 2015;112(2):28001.

Nguyen, V.P., Stroeven, M., Sluys, L.J.. Multiscale Continuous and Discontinuous Modeling of Heterogeneous Materials: a Review on Recent Developments. Journal of Multiscale Modeling 2011;03(04):229–270. doi:10.1142/S1756973711000509.

Novaro, G.M.. Aortic valve disease. 2014.

Padala, M., Keeling, W.B., Guyton, R.A., Thourani, V.H.. Innovations in therapies for heart valve disease. Circulation Journal 2011;75(5):1028–1041.

Peskin, C.S.. Flow patterns around heart valves: A numerical method. Journal of Computational Physics 1972;10(2):252–271.

Pibarot, P., Dumesnil, J.G.. Prosthetic heart valves selection of the optimal prosthesis and long-term management. Circulation 2009;119(7):1034–1048.

Qi, Y., Li, J., Liu, L.. Stiffness prediction of multilayer-connected biaxial weft-knitted fabric-reinforced composites. Journal of Reinforced Plastics and Composites 2015;34(14):1113–1125.

Radermacher, A., Reese, S.. Pod-based model reduction with empirical interpolation applied to nonlinear elasticity. International Journal for Numerical Methods in Engineering 2016;107(6):477–495.

Reese, S.. Meso-macro modelling of fibre-reinforced rubber-like composites exhibiting large elastoplastic deformation. International Journal of Solids and Structures 2003;40(4):951–980. doi:10.1016/S0020-7683(02)00602-9.

Röhrnbauer, B., Kress, G., Mazza, E.. A physically based structural model for a textile prosthetic mesh. International Journal of Solids and Structures 2014;51(3-4):633–646. doi:10.1016/j.ijsolstr.2013.10.030.

Röhrnbauer, B., Mazza, E.. A non-biological model system to simulate the in vivo mechanical behavior of prosthetic meshes. Journal of the Mechanical Behavior of Biomedical Materials 2013;20:305–315. doi:10.1016/j.jmbbm.2013.01.029.

Saeb, S., Steinmann, P., Javili, A.. Aspects of Computational Homogenization at Finite Deformations: A Unifying Review From Reuss' to Voigt's

Bound. Applied Mechanics Reviews 2016;68(5):050801. doi:10.1115/1.4034024.

Saleeb, A.F., Kumar, A., Thomas, V.S.. The important roles of tissue anisotropy and tissue-to-tissue contact on the dynamical behavior of a symmetric tri-leaflet valve during multiple cardiac pressure cycles. Medical Engineering & Physics 2013;35(1):23–35.

Schmoller, K.M., Bausch, A.R.. Similar nonlinear mechanical responses in hard and soft materials. Nature Materials 2013;12(4):278.

Shahriari, S., Kadem, L., Rogers, B., Hassan, I.. Smoothed particle hydrodynamics method applied to pulsatile flow inside a rigid two-dimensional model of left heart cavity. International Journal for Numerical Methods in Biomedical Engineering 2012;28(11):1121–1143.

Sherburn, M.. Geometric and mechanical modelling of textiles. Ph.D. thesis; University of Nottingham; 2007.

Singh, C., Wong, C., Wang, X.. Medical Textiles as Vascular Implants and Their Success to Mimic Natural Arteries. J Funct Biomater 2015;6(3):500–525. doi:10.3390/jfb6030500.

Sodhani, D., Raj, R.V., Simon, J., Reese, S., Moreira, R., Gesché, V., Jockenhövel, S., Mela, P., Stier, B., Stapleton, S.E.. Artificial Textile Reinforced Tubular Aortic Heart Valves - Multi-scale Modelling and Experimental Validation, 2018a. doi:10.1007/978-3-319-59548-1_11.

Sodhani, D., Reese, S., Jockenhövel, S., Mela, P., Stapleton, S.E.. Multi-scale modelling and simulation of a highly deformable embedded biomedical textile mesh composite. Composites Part B: Engineering 2018b;143:113–131.

Sodhani, D., Reese, S., Moreira, R., Jockenhövel, S., Mela, P., Stapleton, S.E.. Multi-scale modelling of textile reinforced artificial tubular aortic heart valves. Meccanica 2016;52(3):677–693. doi:10.1007/s11012-016-0479-y.

Sodhani, D., Stier, B., Reese, S.. Evaluating the simulation of ideal filler reinforced elastomers using a full field modelling approach. Constitutive Models for Rubber IX 2015;:317.

Stapleton, S.E., Moreira, R., Jockenhoevel, S., Mela, P., Reese, S.. Effect of reinforcement volume fraction and orientation on a hybrid tissue engineered aortic heart valve with a tubular leaflet design. Advanced Modeling and Simulation in Engineering Sciences 2015;2(1):1–17.

Stier, B., Simon, J., Reese, S.. Meso-mechanical investigation of woven carbon fiber reinforced plastics. In: THE 19TH INTERNATIONAL CONFERENCE ON COMPOSITE MATERIALS. 2013. .

Stier, B., Simon, J.W., Reese, S.. Finite Element Analysis of Layered Fiber Composite Structures Accounting for the Materials Microstructure and Delamination. Appl Compos Mater 2015a;22(2):171–187. doi:10.1007/s10443-013-9378-8.

Stier, B., Simon, J.W., Reese, S.. Numerical and experimental investigation of the structural behavior of a carbon fiber reinforced ankle-foot orthosis. Med Eng Phys 2015b;37(5):505–511. doi:http://dx.doi.org/10.1016/j.medengphy.2015.02.002.

Sturla, F., Votta, E., Stevanella, M., Conti, C.A., Redaelli, A.. Impact of modeling fluid-structure interaction in the computational analysis of aortic root biomechanics. Medical Engineering & Physics 2013;35(12):1721–1730.

Sun, W., Li, K., Sirois, E.. Simulated elliptical bioprosthetic valve deformation: Implications for asymmetric transcatheter valve deployment. Journal of Biomechanics 2010;43(16):3085–3090.

Tan, P., Tong, L., Steven, G.P.. Modelling for predicting the mechanical properties of textile composites—A review. Compos Part A Appl Sci Manuf 1997;28(11):903–922. doi:10.1016/S1359-835X(97)00069-9.

Toma, M., Bloodworth, C.H., Pierce, E.L., Einstein, D.R., Cochran, R.P., Yoganathan, A.P., Kunzelman, K.S.. Fluid-structure interaction analysis of ruptured mitral chordae tendineae. Annals of Biomedical Engineering 2017;45(3):619–631.

Ugbolue, S.C.. Geometrical Analysis of Warp Knit Auxetic Fabrics. J Text Sci Eng 2015;05(03):1000201. doi:10.4172/2165-8064.1000201.

Van Lieshout, M., Peters, G., Rutten, M., Baaijens, F.. A knitted, fibrin-covered polycaprolactone scaffold for tissue engineering of the aortic valve. Tissue Engineering 2006a;12(3):481–7. doi:10.1089/ten.2006.12.481.

Van Lieshout, M.I., Vaz, C.M., Rutten, M.C.M., Peters, G.W.M., Baaijens, F.P.T.. Electrospinning versus knitting: two scaffolds for tissue engineering of the aortic valve. Journal of Biomaterials Science, Polymer Edition 2006b;17(1-2):77–89. doi:10.1163/156856206774879153.

Van Loon, R., Anderson, P.D., Baaijens, F.P.T., Van De Vosse, F.N.. A three-dimensional fluid-structure interaction method for heart valve modelling. Comptes Rendus Mécanique 2005;333(12):856–866.

Vassiliadis, S., Kallivretaki, A., Provatidis, C., Domvoglou, D.. Mechanical analysis of woven fabrics: The state of the art. INTECH Open Access Publisher, 2011.

Verpoest, I., Lomov, S.V.. Virtual textile composites software WiseTex: Integration with micro-mechanical, permeability and structural analysis. Composites Science and Technology 2005;65(15-16 SPEC. ISS.):2563–2574. doi:10.1016/j.compscitech.2005.05.031.

Votta, E., Le, T.B., Stevanella, M., Fusini, L., Caiani, E.G., Redaelli, A., Sotiropoulos, F.. Toward patient-specific simulations of cardiac valves: State-of-the-art and future directions. Journal of Biomechanics 2013;46(2):217–228.

Wan, Y., Sun, B., Gu, B.. Multi-scale structure modeling of damage behaviors of 3D orthogonal woven composite materials subject to quasi-static and high strain rate compressions. Mechanics of Materials 2016;94:1–25. doi:10.1016/j.mechmat.2015.11.012.

Wang, Q., Kodali, S., Primiano, C., Sun, W.. Simulations of transcatheter aortic valve implantation: implications for aortic root rupture. Biomechanics and Modeling in Mechanobiology 2015;14(1):29–38.

Weber, M., Heta, E., Moreira, R., Gesche, V.N., Schermer, T., Frese, J., Jockenhoevel, S., Mela, P.. Tissue-engineered fibrin-based heart valve with a tubular leaflet design. Tissue Eng Part C Methods 2013;20(4):265–275. doi:10.1089/ten.TEC.2013.0258.

Weinberg, E.J., Mofrad, K., R., M.. A multiscale computational comparison of the bicuspid and tricuspid aortic valves in relation to calcific aortic stenosis. Journal of Biomechanics 2008;41(16):3482–3487.

Weinberg, E.J., Mofrad, M.R.K.. Transient, three-dimensional, multiscale simulations of the human aortic valve. Cardiovascular Engineering 2007;7(4):140–155.

Weinberg, E.J., Shahmirzadi, D., Mofrad, M.R.K.. On the multiscale modeling of heart valve biomechanics in health and disease. Biomechanics and Modeling in Mechanobiology 2010;9(4):373–387.

Wu, W., Pott, D., Mazza, B., Sironi, T., Dordoni, E., Chiastra, C., Petrini, L., Pennati, G., Dubini, G., Steinseifer, U., Sonntag, S., Kuetting, M., Migliavacca, F.. Fluid–Structure Interaction Model of a Percutaneous Aortic Valve: Comparison with an In Vitro Test and Feasibility Study in a Patient-Specific Case. Annals of Biomedical Engineering 2016;44(2):590–603.

Yang, H., Veneziani, A.. Efficient estimation of cardiac conductivities via pod-deim model order reduction. Applied Numerical Mathematics 2017;115:180–199.

Yeoman, M.S., Reddy, D., Bowles, H.C., Bezuidenhout, D., Zilla, P., Franz, T.. A constitutive model for the warp-weft coupled non-linear behavior of knitted biomedical textiles. Biomaterials 2010;31(32):8484–8493. doi:10.1016/j.biomaterials.2010.07.033.

Zhang, L., Jiang, G., Miao, X., Cong, H.. Three-dimensional computer simulation of warp knitted spacer fabric. Fibres & Textiles in Eastern Europe 2012;3(92):56–60.

Publications

2018

- Sodhani D, Reese S, Aksenov A, Soğanci S, Jockenhövel S, Mela P, Stapleton SE. **Fluid-structure interaction simulation of artificial textile reinforced aortic heart valve: Validation with an in-vitro test.** Journal of Biomechanics. 2018 Jul 20.

- Sodhani D, Reese S, Jockenhövel S, Mela P, Stapleton SE. **Multi-scale modelling and simulation of a highly deformable embedded biomedical textile mesh composite** Composites Part B: Engineering. 2018 Jun 15;143:113-31.

- Sodhani D, Raj RV, Simon J, Reese S, Moreira R, Gesché V, Jockenhövel S, Mela P, Stier B, Stapleton SE. **Artificial Textile Reinforced Tubular Aortic Heart Valves—Multi-scale Modelling and Experimental Validation.** In Biomedical Technology 2018 (pp. 185-215). Springer, Cham.

2017

- Sodhani D, Reese S, Moreira R, Jockenhövel S, Mela P, Stapleton SE. **Multi-scale modelling of textile reinforced artificial tubular aortic heart valves.** Meccanica. 2017 Feb 1;52(3):677-93.

2015

- D. Sodhani, B. Stier, S. Reese; Eds.: Bohdana Marvalova and Iva Petrikova; **Evaluating the simulation of ideal filler reinforced elastomers using a full field modelling approach**; Constitutive Models for Rubbers IX; Taylor & Francis Group; 2015; ISBN: 978-1-138-02873-9; 317-323

2014

- Sodhani D, Reese S. **Finite element based micro-mechanical modelling of interphase in filler reinforced elastomers.** Soft Materials. 2014 Nov 24;12(sup1):S152-61.
- Sodhani D, Reese S. **Finite element-based micromechanical modelling of microstructure morphology in filler-reinforced elastomer.** Macromolecules. 2014 Apr 29;47(9):3161-9.

2013

- Sodhani D, Reese S. **Finite element based micro-mechanical modelling of micro-structure morphology in filler reinforced elastomer.** Constitutive Models for Rubber VIII. 2013 Jun 3:273.

2012

- Sodhani D, Reese S. **3d finite element modelling of filler reinforced elastomers**. InProceedings of 15th EUROPEAN CONFERENCE ON COMPOSITE MATERIALS, Venice, Italy; 2012 Jun.
- Sodhani D, Reese S. **Plane stress finite element analysis of filler reinforced polymers**. PAMM. 2012 Dec;12(1):441-2.